COMPUTATIONAL STUDY OF IONIC POLYMERS: MULTISCALE STIFFNESS PREDICTIONS AND MODELING OF THE ELECTROMECHANICAL TRANSDUCTION

by

Fei Gao

BE, University of Science and Technology of China, P.R. China, 2002

MS, University of Science and Technology of China, P.R. China, 2005

Submitted to the Graduate Faculty of

the Swanson School of Engineering in partial fulfillment

of the requirements for the degree of

Doctor of Philosophy

University of Pittsburgh

2010

UNIVERSITY OF PITTSBURGH

SWANSON SCHOOL OF ENGINEERING

This dissertation was presented

by

Fei Gao

It was defended on

April 6, 2010

and approved by

Dr. William W. Clark, Professor, Mechanical Engineering and Materials Science

Dr. Qing-Ming Wang, Associate Professor, Mechanical Engineering and Materials Science

Dr. Jung-Kun Lee, Assistant Professor, Mechanical Engineering and Materials Science

Dr. Barbar J. Akle, Assistant Professor, Mechanical Engineering, Lebanese American University

Dissertation Director: Dr. Lisa M. Weiland, Assistant Professor, Mechanical Engineering and Materials Science

COMPUTATIONAL STUDY OF IONIC POLYMERS:

MULTISCALE STIFFNESS PREDICTIONS AND MODELING OF THE

ELECTROMECHANICAL TRANSDUCTION

Fei Gao, PhD

University of Pittsburgh, 2010

Ionic polymer transducers (IPTs) represent a relatively new class of active ('smart') materials, which can function as highly sensitive mechanical sensors as well as actuators. An IPT is made of an ionic polymer membrane sandwiched between two conductive electrodes. They generate controllable strain when applying a low voltage (<5 V) across their thickness and generate measurable currents due to extremely small mechanical strain. IPTs are cost effective and often have superior sensing capabilities compared to other active materials such as piezoelectrics. However, this novel class of transducers has not been widely employed mainly because the mechanism of IPT sensing is not clearly understood.

In this dissertation, the mechanical properties of ionic polymers (Nafion and Selemion), the ionomer morphology, and the fundamental mechanism responsible for the electromechanical sensing responses of IPTs are studied. A multiscale model for the prediction of material stiffness is presented. The results give access to a fundamental material parameters currently inaccessible via experimentation, namely local stiffness. Subsequently the sensing mechanism of stream potential is hypothesized. It is argued that the mechanism of streaming potential, unlike prior hypotheses, is able to systematically explain generalized experimentally observed sensing phenomena, such as the observation of an optimum conductive particulate volume fraction in the

interpenetrating electrode region of the transducer. Moreover, it is argued that coupling the exploration of local stiffness and streaming potential is prerequisite to gaining insight into subtler experimental sensing phenomena such as experimentally observed variations in sensing due to variations in IPT architecture.

TABLE OF CONTENTS

LIST OF TABLES

LIST OF FIGURES

NOMENCLATURE

Chapter 2

d	Electromechanical coupling coefficient
$\langle h^2 \rangle$	Mean square polymer chain length
k	Boltzmann's constant
M_e	Ionomer equivalent weight
N_A	Avogadro's number
r_c	Cluster radius
T	Temperature
V_i	Volume of ion exchange site
γ_c	Surface energy density of cluster
ΔV	Polymer volume change with water uptake
$\Delta V'$	Volume fraction of ion exchange sites
ρ_d	Density of dry polymer
ρ_w	Density of water
ρ^*	Effective density of hydrated polymer

Chapter 3

c	Constant of integration
E	Young's modulus
E_{ave}	Young's modulus of bulk material
E_{bb}	Young's modulus of polymer backbone
E_{cl}	Young's modulus of cluster
E_{sc}	Young's modulus of semicrystalline region of material
f	Function of Johnson distribution
f'	First derivative of f
f''	Second derivative of f
f_{bb}	Backbone volume fraction
f_{cl}	Cluster volume fraction
f_{sc}	Semicrystalline region volume fraction
f^*	Nominal stress
$\langle h^2 \rangle$	Mean square polymer chain length
k	Boltzmann's constant
l_{c-c}	Carbon-carbon bond length
m	Number of repeating monomer units in a polymer molecule
M_e	Ionomer equivalent weight
MW_{c-c}	Molecular weight of the portion of the chain between two cluster communication points
n	Number of repeating groups in a monomer unit
N_A	Avogadro's number

Chapter 3 (continued)

P	Probability density function
Q	Normalized statistical weight matrix
r	End-to-end chain length
r_o	Root mean square of *r*-values
S	Entropy
T	Temperature
U	Statistical weight matrix
V_i	Volume of ion exchange site
α	Relative length of material
γ	Shape parameter of the PDF for Johnson family distributions
γ_c	Surface energy density of cluster
ΔV	Polymer volume change with water uptake
$\Delta V'$	Volume fraction of ion exchange sites
δ	Shape parameter of the PDF for Johnson family distributions
θ	In-plane bond angle
λ	Scale parameter of the PDF for Johnson family distributions
υ	Number density of network chains
ξ	Location parameter of the PDF for Johnson family distributions
ρ	Material density
ρ_d	Density of dry polymer
ρ^*	Effective density of hydrated polymer
φ	Out-of-plane rotation angle

Chapter 4

a	Channel radius
A_e	Effective area of metal-polymer interfacial area
a_{ch}	Radius of conduction channel
a_{cl}	Radius of cluster
a_{IL}	Channel radius in ionic liquid swollen IPT
a_{Li}	Channel radius in lithium form IPT
a_{Na}	Channel radius in sodium form IPT
a_w	Channel radius in water swollen IPT
B	Dimensionless constant
C	Dimensionless constant
d	Cluster center-to-center distance
E	Young's modulus of bulk material
E_f	Young's modulus at frequency f
e	Electro charge
h	Half of the channel height
I_{IL}	Current in ionic liquid swollen IPT
I_{Li}	Current in lithium form IPT
I_{Na}	Current in sodium form IPT
I_s	Streaming current in a channel

Chapter 4 (continued)

I_t	Total current in an IPT
I_w	Current in water swollen IPT
I_y	Moment of inertia
$[i]$	Free ion concentration
k	Boltzmann's constant
l	Channel length
l_{ch}	Legnth of conduction channel
L_f	Cantilever free length
N	Number of channels
n	Number density of monovalent ions
N_A	Avogadro's number
n_{an}	Number of anions in a cluster
N_e	Effective number of channels
n_f	Number of free ions in a cluster
n_p	Number of ion pairs in a cluster
P	Force on cantilever end
q	Flux
T	Temperature
v	Flow velocity
$v_{\kappa^{-1}}$	Flow velocity within one Debye length

Chapter 4 (continued)

V_{anion}	Anion volume
V_{cation}	Cation volume
$V_{channel}$	Volume of a channel
V_{cl}	Volume of a cluster
V_{fl}	Volume of fluid in a cluster
$V_{electrode}$	Volume of metal electrode
$V_{Au}\%$	Au volume fraction in metal electrode
$V_{RuO_2}\%$	RuO_2 volume fraction in metal electrode
V_{Nafion}	Volume of Nafion
V_{total}	Total volume of porours medium
V_{void}	Volume of void in porous medium
W	Cantilever width
w	Channel width
β	Cluster radius ratio
Δp	Pressure difference
δ	Cantilever tip deflection
ε	Dielectric constant of water
ε_o	Permittivity of vacuum
η	Viscosity
η_{IL}	Viscosity of ionic liquid

Chapter 4 (continued)

η_{Li}	Viscosity of water with lithium cations
η_{Na}	Viscosity of water with sodium cations
η_w	Viscosity of water
κ	Permeability of medium
κ^{-1}	Debye length of the diluent
$v_{f,Li}$	Water volume fraction in lithium form IPT
$v_{f,w}$	Water volume fraction
$v_{f,IL}$	Ionic liquid volume fraction
$v_{f,l}$	Diluent volume fraction
$v_{f,Na}$	Water volume fraction in sodium form IPT
$v_{f,p}$	Particulates volume fraction
ρ	Charge density
ρ_e	Charge density of the solution
ρ_s	Charge density at shear surface
ϕ	Porosity

ACKNOWLEDGEMENTS

During my study at the University of Pittsburgh, many people have supported and helped me. I would like to take this opportunity to thank them.

First and foremost, I would like to thank my academic advisor, Dr. Lisa Weiland, for her guidance and advice throughout my Ph.D. studies, for being supportive and patient, and for giving me the opportunity to explore the possibilities of my potential. She always supports and helps me in every possible way that a professor can help her/his students. Thank you very much! I would like to thank my thesis committee members, for being on my committee and providing valuable discussions.

I would like to thank all of my friends, teachers, professors, and colleagues throughout my career at the University of Science and Technology of China, the University of Pittsburgh, and ANSYS, Inc. for always supporting me and seeing my potential. Special thanks to Dr. Guoyu Lin for always believing in me, being supportive and patient, and helping me with my job search.

Last but not the least, I would like to express my deep gratitude to my parents, Youchao Gao and Xiaoling He, and my best friends, Yan Yang, Jie Wu Pan, Chao Chen, and Wei An, for their love, support, and always being there to turn to. Without you, I could have accomplished nothing.

1.0 INTRODUCTION

Ionic polymer transducers (IPTs) represent a relatively new class of active ('smart') materials, which can function as highly sensitive mechanical sensors as well as actuators. The electromechanical sensing properties of ionic polymers were first reported by Sadeghipour et al. in 1992 [1]. But to date the physical mechanism responsible for this sensing response is not yet understood, limiting exploitation of these sensors.

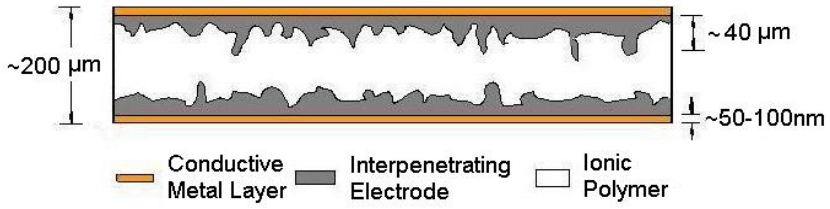

Figure 1.1: Structure of a typical IPT (schematic view)

To access the electromechanical coupling the ionic polymer (often Nafion by DuPont) must be sandwiched between two conductive electrodes. The structure of a typical IPT is shown in Figure 1.1. The exact state of the ionic polymer can be manipulated, but is typically ion exchanged from its virgin acid (H^+) form to sodium (Na^+) or lithium (Li^+) forms, and saturated with water. IPTs are sometimes referred to as Ionic Polymer-Metal Composites (IPMCs), which places emphasis on the constituents frequently utilized in the creation of these transducers. This

work adopts the moniker IPT as favoring a description of the functionality while leaving open the possibility of developing IPTs with alternate-to-metal electrically conductive media.

IPTs generate controllable strain when applying a low voltage (<5 V) across their thickness and generate measurable currents due to extremely small mechanical strain. The voltage produced across the thickness of the IPT strip by bending it can be calibrated and correlated to the applied loads or stresses. Sadeghipour et al. have demonstrated the potential of IPTs as accelerometers for vibration sensing with linear characteristics and high sensitivity [1]. Shahinpoor et al. also reported the application of IPT sensors to quasi-static or dynamic displacement sensing [2]. While there has been considerable discussion of their response in bending mode, IPTs are also effective shear, compression, and tension sensors. For example, for 10 mm x 30 mm IPT samples, a relationship between electric charge and strain was found under shear loading. The average sensitivity was reported to be 0.0242 μC/ε at frequencies of 30 to 120 Hz [3].

In this dissertation, the mechanical properties of ionic polymers, the ionomer morphology, and the fundamental mechanism responsible for the electromechanical sensing responses of IPTs are studied. This will promote the development and optimization of sensing systems that are highly sensitive, miniature, compliant and potentially autonomous.

1.1 MOTIVATION

In mechanical and civil engineering, mechanical deformation/strain sensing is of great importance. Sensor systems are capable of improving the precision of mechanical systems, performing nondestructive damage evaluation, and expanding device reliability, lifetime, and

application environments. The extent to which these goals may be realized is frequently a function of the sensor's sensitivity. IPTs are cost effective and often have superior sensing capabilities compared to other active materials such as piezoelectrics. However, this novel class of transducers has not been widely employed because the mechanism of IPT sensing is not clearly understood. Further, it is widely accepted that strong correlations exists among the ionic polymer morphology and stiffness, electrode architecture, and active response. Perhaps not surprisingly, ionomer morphology and stiffness evolution are also poorly understood. This work is intended to investigate the fundamental mechanism of IPT sensing through simultaneous consideration of morphology and stiffness.

1.2 OBJECTIVE

The immediate goal of this work is to investigate the fundamental sensing mechanism in IPTs. Specifically the hypothesis of a streaming potential mechanism in the electrode region is explored. In order to do this a number of contributing factors must be considered, such as the roles of ionomer stiffness, ionomer morphology, and electrode architecture. Physics-based models are developed and compared to reported experimental studies. The ultimate goals of this dissertation are to provide meaningful insight into the interrelation among these parameters, and subsequently to test the hypothesis of streaming potential as the mechanism responsible for IPT sensing. Achieving these goals will enable the optimization and widespread use of IPT sensor arrays.

1.3 CONTRIBUTIONS

The contributions of this dissertation include (i) creation of models which enable assessment of multiscale stiffness parameters that are experimentally inaccessible, (ii) creation of methods which will enable critical review of the streaming potential hypothesis for varied electrode architectures, and (iii) exploration of the interface among these parameters for varied IPT preparations. Included in the studies are demonstrations of method effectiveness through comparison to experiment. Predictions are found to be consistent with experiment. More importantly though are the subsequent insights gained that may be employed to optimize IPT sensitivity and reliability. Moreover, the presented methods are consistently computationally *un*intensive, thereby increasing the likelihood of their broader usage.

1.4 DOCUMENT ORGANIZATION

This dissertation explores the hypothesis that streaming potential is the dominant mechanism of IPT sensing. This first requires review of IPTs per the current state of the art (Chapter 2). However, full appreciation of IPTs can be achieved only after establishing an equally in-depth appreciation of the active ionic polymer layer; to this end Chapter 3 explores ionic polymer morphology. Chapter 4 then offers development of the streaming potential modeling approach, including consideration of the impact of ionomer morphology. Predictions are compared to reported experiments for a number of IPT cases, including for varied ionomer properties and varied electrode architectures. Finally, Chapter 5 offers concluding remarks. Because a number

of modeling constructs are explored and developed in this dissertation, appropriate nomenclature tables are offered for Chapters 2-4 as part of the preface of this dissertation.

2.0 BACKGROUND AND LITERATURE REVIEW

Ionic polymers first received widespread attention in the 1970's for their application of chemoelectric properties in Polymer Electrolyte Membrane Fuel Cells (PEM FCs), and more recently for use in Fuel Cell Vehicles [4-6]. Recent enthusiasm aside, PEM FCs have been in existence for some time; they were first deployed in the Gemini space program in 1962 [7]. There has also been significant research activity on application of ionic polymers as transducers, or 'smart materials' since their electromechanical sensing properties were first reported later by Sadeghipour et al. in 1992 [1]. Their biocompatibility coupled with high gravimetric energy density and cryogenic functionality, has led to considerable conjecture over potential applications ranging from biosensors to outer-space actuators [1-3,8,9]. From the electromechanical transduction perspective ionic polymer transducers (IPTs) are a relatively new class of active materials. Like their PEM FC predecessors, it is generally accepted that electromechanical transduction in IPTs arises from selective ionic conduction. However, the exact mechanism of IPT electromechanical coupling is not understood.

This chapter provides a review of the current state of the art in understanding of the active ionic polymer layer as well as the IPT as a whole. The chapter begins with a review of ionic polymers and of the potential applications of IPTs. Because the following dissertation explicitly explores the significance of ionomer morphology in IPT response, Section 2.2 presents the current state of understanding of ionomer morphology. Section 2.3 then reviews

experimentally observed IPT response including studies of the impact of electrode architecture. The closing section of this chapter reviews ionic polymer and IPT transduction models. The following chapters, which present the modeling studies of this dissertation, subsequently expand on the current state of the art in IPT modeling, especially as it relates to testing the hypothesis of streaming potential dominating IPT sensing response.

2.1 IONIC POLYMER TRANSDUCER APPLICATIONS

An ionic polymer, i.e., an ionomer, is a polymer that comprises both electrically neutral repeating units and ionized units. To access the electromechanical coupling response the ionomer must be sandwiched between two conductive electrodes in the creation of an IPT. IPTs generate controllable strain when applying a low voltage (<5 V) across their thickness and generate measurable currents when subjected to mechanical stimulation.

Identification of (and ultimately, optimization of) the fundamental mechanisms responsible for IPT sensing is motivated by their current (not-optimized) ability to satisfy a range of basic application criteria – when properly fabricated and utilized they are reliable, conformal, multifunctional, and highly sensitive.

The mechanical sensing properties of ionic polymers have been quantified and compared to that of piezoelectric materials by Newbury and Leo [10], and Farinholt and Leo [11]. It has been demonstrated that, in charge sensing mode, an IPT sensor is one order of magnitude more sensitive than traditional piezoelectric transducers. When saturated with ionic-liquids, IPTs have been demonstrated to be reliable and environmentally stable [12]; in this form they can operate over a million cycles in open air [13]. Moreover, IPTs are soft elastic sensors which are

compatible with conformal structures. They can be made as thin as 10 μm and can be cut into any area or shape, which makes them good candidates for miniaturization. In addition, although an IPT in actuation generates bending deformation only, electric signals are observed in IPT sensors under bending, shear, compression, and tension.

As sensors, IPTs have a broad range of potential applications. By bending the IPT strip, a voltage is produced across the thickness of the strip. The output voltage can be calibrated and correlated to the applied loads or stresses. Based on this general observation it has previously been established that the IPT sensors have a number of viable applications. Based on their vibrational damping property, Sadeghipour et al. [1] have demonstrated their potential as accelerometers for vibration sensing with linear characteristics and high sensitivity. Shahinpoor et al. [2] reported the application of IPT sensors to quasi-static or dynamic displacement sensing. While there has been considerable discussion of their sensing responses in bending mode, IPTs are also effective shear, compression, and tension sensors. For example, for IPT samples with dimensions of 10 mm x 30 mm, a relationship between electric charge and strain was found under shear loading. The average sensitivity was reported to be 0.0242 μC/ε at frequencies of 30 to 120 Hz [3].

Due to the electromechanical coupling properties of IPTs, they can function as mechanical actuators as well as sensors. As actuators, IPTs have large activation displacement, high gravimetric energy density, while requiring low stimulation electric field. There has been considerable conjecture over the potential applications of these soft transducers including artificial robotic muscles and cryogenic wiper blades [8,9,14-16]. To date a large volume of reports have emerged on IPT actuators, while comparatively few have been presented for sensing.

While not a focus of this dissertation, it should be noted that the potential for utilizing IPTs as energy scavengers exists. Energy scavenging is the process by which energy from the surrounding environment is converted into stored electrical energy. Ionic polymers are a unique class of material that exhibit both electromechanical and chemoelectric coupling. Besides their sensing and actuation functionalities when dynamic excitation is applied on ionic polymer membranes, they also can produce DC electricity due to the reaction of hydrogen and oxygen at the membrane surface, which is the basis for power generation in PEM FCs. These properties of ionic polymers enable their applications as mechanical and chemical energy scavengers. IPTs therefore have the long term potential for utilization in sensing/scavenging arrays in remote locations, and whose lifetime is not limited by a finite energy storage source such as a battery.

2.2 IONOMER MORHOLOGY

Ionomers are fabricated by the addition of an ionized (hydrophilic) pendant chain (usually no more than 15%) to electrically neutral (hydrophobic) polymeric chains. The addition of pendant ionic groups produces phase separation: nanoscale hydrophilic regions of pendant ionic groups, counterions, and diluents reside within a hydrophobic polymer matrix. While the counterions are attracted to the covalently attached pendant ionic groups, they are otherwise free to move through the hydrophilic regions. The capacity of counterions can be described by the equivalent weight (EW) of the ionic polymer, which is defined as dry mass in grams of ionic polymer in proton form per mole of acid groups in the polymer divided by the valence of the acid group. The mobility of counterions is known as selective ionic conduction and is the basis of ionic polymer use in fuel cell applications. The morphology developed due to hydrophobic/hydrophilic

phase separation has a strong influence on the tortuosity of selective ionic conduction and is therefore of considerable interest in PEM FC applications [17].

Despite the fact that there is no agreement on the exact mechanism responsible for IPT sensing, it is generally accepted that, like the chemoelectric applications, it arises from selective ionic conduction, which in turn is sensitive to ionomer morphology. This section is therefore dedicated to reviewing the current state of understanding of ionomer morphology.

2.2.1 **Cluster Morphology**

A significant number of ionomer morphologies have been proposed including, for instance, lamellar and planar postulates [18-20]. It has also been suggested that the morphology is not at all fixed, rather that it may vary significantly with hydration state [21]. But the actual morphology remains an open topic; in fact it has even been suggested that, based on the experimental procedures employed to date, the actual ionomer morphology is unlikely to be predicted, but should be sought nonetheless [22].

Early models of common ionomers, such as Nafion, were based on the concept of spherical ‘ion clusters’ connected by ‘ion channels’ such as that proposed by Hsu and Gierke [23]. These models were used to predict the ordering of the clusters as a rationale for (as opposed to prediction of) selective ionic conduction in PEM FC applications [24,25]. Hsu and Gierke proposed that the hydrophilic ionic side groups and the water that has been taken up by the material cluster together. The model further suggests an idealized structuring whereby the embedded clusters are of essentially constant radius, uniformly distributed throughout the material, and interconnected by channels (Figure 2.1). Despite the idealized nature of the model and general acceptance that it is incorrect, the Hsu and Gierke model has been widely used

because of its simplicity, relative predictive effectiveness, and the absence of consensus for an alternate postulate.

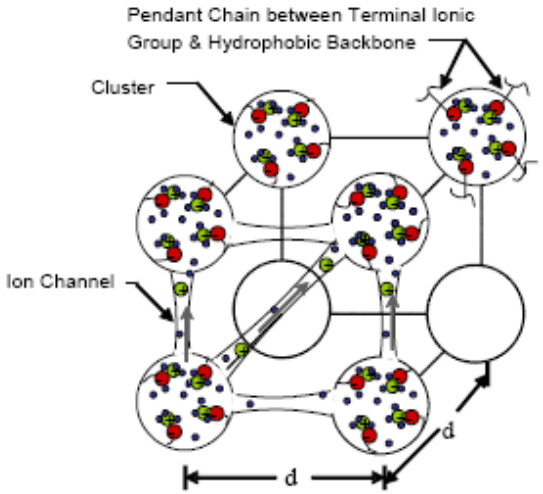

Figure 2.1: Spherical cluster morphology with intercluster channels proposed by Hsu and Gierke [23] and the selective ionic conduction.

Consider for instance a recent micromechanical prediction of cluster size and distribution based on minimization of elastic, electrostatic, and cluster surface energies [26]. The approach draws from the Hsu and Gierke model while enabling a continuum strategy to estimate the morphological impact of varying the counterion, diluent, or even the base ionomer. Despite the fact that the predicted morphology is likely incorrect (in part because of its acceptance of the Hsu and Gierke model), the approach is relatively straight forward and enables prediction of the reality that morphology will change with ionomer state. Moreover, the magnitude of these predicted morphological variations, despite lacking absolute correctness, correlates appropriately with experimental observations.

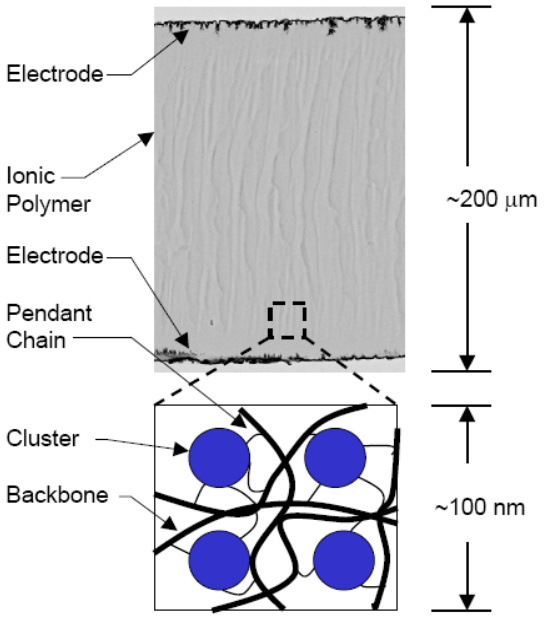

Figure 2.2: Cross-sectional view of a typical IPT relative to the assumed ionic polymer clustering morphology by Hsu and Gierke [23].

Consider further that it has been experimentally established that active response is a strong function of hydration [12,27]; per the micromechanical prediction approach cluster radius is significantly diminished with decreasing hydration. Decreased cluster radius per the Hsu and Gierke model corresponds to increased tortuosity for selective ionic conduction, and subsequently corresponds to experimental observations of decreased electromechanical coupling [27,28]. Further, morphological variation is observed for varied counterions and/or diluents; again active response is also observed to vary [27,28]. While the spherical cluster model is generally accepted to be incorrect, the foregoing examples demonstrate the coupling between the morphological and active response domains, and thus the need to attempt morphological characterization. Figure 2.2 provides an illustration of scaling for the spherical cluster morphology model for a typical IPT case.

2.2.2 **Parallel Water Channel Morphology**

Schmidt-Rohr and Chen [29] have recently offered arguments that for the specific case of Nafion the hydrophilic regions are akin to long parallel water channels (Figure 2.3). The proposed channels are surrounded by partially hydrophilic pendant chains, forming inverted-micelle cylinders. The dimensions of these channels (1.8~3.5 nm diameter) are large compared to earlier postulates. For comparison, while Hsu and Gierke do not offer dimensions for the proposed intercluster channels qualitatively illustrated in Figure 2.1, it is understood that these dimensions are substantially smaller than those of the clusters (*i.e.*, ~4.5 nm diameter clusters might have ~0.4 nm channels). Schmidt-Rohr and Chen go on to argue that this parallel channel morphology successfully explains the transport properties of hydrated Nafion as well as the results of a range of SAXS studies, which had been difficult to explain for the more tortuous morphological propositions.

It is intuitive that parallel water channel morphology has significantly reduced tortuosity in the selective ionic conduction pathway as compared to the clustering postulate of Hsu and Gierke. For the purposes of this dissertation, these two cases are treated as bounding cases, and thus both will be considered in the assessment of the streaming potential hypothesis.

While morphology models and models of active response are typically performed in separate studies, the notion that selective ionic conduction serves as the basis of active response is universal among the proposed morphological models. Similarly, the fact that morphology has an important role to play in the ultimate active response is generally acknowledged in transduction models. That both morphology and transduction remain open topics is perhaps not surprising.

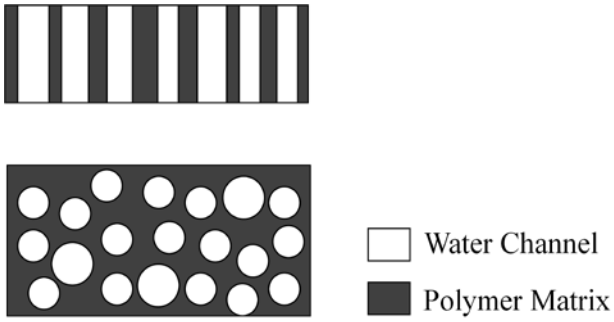

Figure 2.3: Parallel water channel morphology proposed by Schmidt-Rohr and Chen where channels vary between 1.8 and 3.5 nm in diameter [29]

2.2.3 **Role of Ionomer Stiffness**

As just noted, there is a lack of consensus on both ionomer morphology and underlying electromechanical mechanisms responsible for IPT sensing. Despite this lack of consensus, it is understood that both are functions of ionomer stiffness. In the case of IPT transduction models this stiffness dependence is displayed at two length scales. At the device length scale, classic characterization parameters such as free displacement and blocked force are a function of the active material's stiffness [30]. At the nanoscopic length scale, the local backbone elastic energy is an important parameter in morphology evolution [26]. In addition, Weiland and Leo [31,32] suggest that pendant chain stiffness of ionic polymers plays a role in ion distribution as it relates to the availability of free ions for selective ionic conduction. However, at both length scales ionomer stiffness values are experimentally difficult or, in some cases, impossible to measure.

In the case of the millimeter-to-centimeter, device length scale, reported stiffness values can range by as much as 300%. For instance, Nafion 117 (1100 EW, 7 mils (178 μm) thick) membrane in Li^+ form is reported to have stiffness from 70 MPa to 300 MPa for fully hydrated

to dry cases [14,33-35]. Experimental challenges associated with these variations include hydration control, sample preparation variations (such as ion exchange method), and even variations from one batch to the next of the ionomer itself. These difficulties are exacerbated at lower length scales, experimental reports at these length scales therefore tend to instead focus on AFM, SAXS, etc. (which are not appropriate for quantifiably reliable stiffness assessments).

Despite the challenges associated with obtaining exacting stiffness properties, the multi-length scale dependence of morphology and ultimately active response on stiffness warrants its investigation. Multiscale modeling represents one viable approach to exploring this multi-length scale dependence.

2.2.4 **Rotational Isomeric State (RIS) Multiscale Stiffness Assessment**

Rotational Isomeric State (RIS) theory as proposed by Flory [36] is based on the recognition that the conformation of a single polymer chain arises from individual bonds assuming low energy orientations. The premise is straight forward: it is assumed that there are a discrete number of low energy orientations for any given bond within a larger polymer chain. Moreover, the probability of each is dictated by both the magnitude of the energy barriers between orientations and by the orientation of the adjacent bonds. By assessing the probability of specific bond placements over the length of entire chains, projection of the conformation of the entire chain is possible. Part of this prediction necessarily includes assessing the location of crosslinks. The distance between crosslinks may therefore be predicted. Higher crosslink density corresponds with higher bulk material stiffness.

The original strategy proposed by Flory employed Gaussian statistical approaches to the assessment of the distribution of crosslink lengths. In turn, probability density functions (PDFs)

of the crosslink lengths were employed in Boltzmann statistical mechanics to assess relative bulk stiffness. This decades old strategy continues to be among the most robust multiscale approaches, but is subject to decreasing reliability in short chain systems (a ramification of the Gaussian statistical approach).

Mark and Curro [37] subsequently demonstrated that a Monte Carlo approach for generating crosslink distributions is effective for systems with short crosslink lengths. Sharaf and co-workers [38,39] next extended the short chain approach by considering the presence of rigid inclusions (akin to common composite materials). It is well established in composite materials research that a given constituent will shift the global stiffness as a direct function of that constituent's stiffness and volume fraction [40]. However the composites approach assumes that the stiffness of each constituent is fixed. Conversely, the works of Sharaf and co-workers displays that the stiffness of the polymer varies as the inclusion dimensions and volume fraction are varied; this is the result of the inclusions displacing and thus altering the low energy conformation of the polymer network.

In all of the approaches, the network data (a list of chain lengths between crosslinks) had to be converted into a PDF, which was then employed in a Boltzmann statistical mechanics approach to the assessment of the mechanical properties of the material system. Each of the short chain approaches noted, however, employed a cubic spline statistical approach that included subjective binning of the crosslink data. This insertion of human error into the process ultimately necessitated the normalization of stress strain predictions to minimize this error. In other words, the approach could not be used to predict stiffness, only relative stiffness among similar cases.

A multiscale RIS Monte Carlo (RIS-MC) modeling approach applied to stiffness prediction of ionomers with high crosslink density has subsequently been developed by Weiland

and co-workers [32,41,42]. The approach employs the Mark-Curro Monte Carlo approach, in accordance with the high crosslink density present in ionic polymers. In addition, it expands on the observation that the cubic spline statistical approach is inappropriate for the generation of repeatable stiffness predictions. These works instead employ a Johnson family statistical assessment in the generation of PDFs. This enabled, for the first time, stable quantitative stiffness predictions from this multiscale method, and thus normalization of the predictions was not needed. For the specific case of ionic polymers, it further adopts the composite material methods of Sharaf and coworders by exploring the exclusion of hydrophobic backbones from hydrophilic morphological regions. Because minimization of elastic energy is an important parameter in morphology evolution, developing an understanding of this stiffness variation may become significant in understanding ionomer morphology evolution.

The approach embodies flexibility that enables prediction of ionomer stiffness as a function of its specific composition (ionomer type, counterion type, diluent type and uptake, etc.). This approach has been refined as part of this dissertation. Additional discussion and literature review are presented in Chapter 3 along with model development, results, and demonstration.

2.3 IPT EXPERIMENTAL BACKGROUND

The majority of IPT experimental studies to date have focused on actuation as opposed to sensing. However, experiments show that for an IPT the voltage required to induce a given deformation is typically one to two orders of magnitude larger than the voltage displayed when that same deformation is imposed, which indicates that, unlike piezoelectric transducers, the coupling in IPT sensing is fundamentally different from that in actuation. Thus study of sensing

and actuation necessarily requires consideration of different mechanisms. While it is understood that actuation and sensing necessarily occur via fundamentally different mechanisms, some correlations may be found in studies of the electrode-ionomer interface. Thus the following section offers review of experimental observations of IPT sensing and actuation, including consideration of the electrode architecture.

2.3.1 **Actuation and Sensing**

The majority of IPT research to date has focused on actuation properties. The IPT actuation mode of interest occurs in bending; when a step voltage (< 5V) is imposed the tip of the IPT cantilever bends toward the anode as illustrated in Figure 2.4. The initial displacement occurs over 0.1 seconds, followed by a slow relaxation spanning over 30 seconds [43]. The relaxation is sometimes described as ‘back relaxation’ because it often occurs in the direction opposite the initial displacement as in Nafion-based IPTs. However, relaxation that continues along the original trajectory has also been observed as in Flemion-based IPTs [28]. The magnitude of these responses has been shown to be a function of ionomer type, diluent type and uptake (‘hydration’ in the case of water as diluent), counterion, and electrode architecture. When characterized under dynamic excitation, the magnitude of electromechanical coupling is further found to initially display decreased coupling followed by stable coupling out to the limits of most tests in the low 100s of Hz with increasing frequency; studies in the frequency domain are generally limited to 200 Hz [3,12].

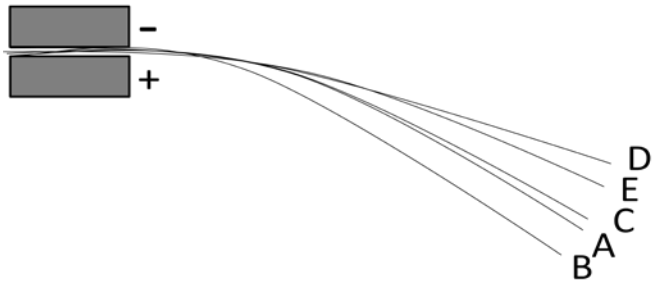

Figure 2.4: Displacement of Nafion-based IPT under step voltage: from A to B fast initial motion, from B to C slow back relaxation, from C to D fast motion upon shorting, and from D to E slow final relaxation [43].

For a typical IPT ones of volts are required for actuation to a given tip displacement (static or dynamic), while imposed deformation to this same displacement generates tens of millivolts in response [2]. This stands in stark contrast to many other electroactive materials such as piezoelectrics where dipole distortion is responsible for both sensing and actuation, and thus the magnitude of coupling is consistent in both modes. While some have artificially imposed an analogous piezoelectric coefficient on IPTs, because the coupling in actuation is substantially larger, in fact no comparable thermodynamic Maxwell relation of electromechanical coupling (*i.e.*, coefficient ***d***) can be identified for IPTs.

It is further observed, in contrast to piezoelectric materials, that the IPT electromechanical response is inherently dynamic. For instance, within the quasistatic realm of excitation (for instance, at or below hundreds of hertz excitation) there is negligible variation in electromechanical coupling in piezoelectric materials. Moreover, a DC stimulation (*i.e.*, step application of an electrical field) will result in a DC response in piezoelectric materials (*i.e.*, step response in deformation) which is held so long as the DC stimulus is sustained. Further, sustained response in piezoelectric sensors is similarly observed. The departure of IPT *actuation* from this benchmark has been addressed above (i.e., Figure 2.4). While it is maintained that the

dominant mechanisms responsible for IPT sensing and actuation differ, they have in common a dynamic basis. Namely, the magnitude of electromechanical coupling in IPT sensors varies with the rate of stimulus. For instance Farinholt and Leo [11] report a linear relationship between the short circuit current and the imposed transducer tip velocity in bending. In addition, in the presence of a DC deformation stimulus the corresponding IPT sensing response is observed to decay over the span of seconds or less [12] (While a decay is also observed in actuation as described by 'relaxation' above, the time scales are fundamentally different).

It is also observed that a fully hydrated (preferably by boiling) IPT displays stronger electromechanical coupling in actuation than one that has 'dried' with exposure to open air [12]. To address this dehydration effect application of ionic liquids instead of water has been proposed [12]. Conversely, Bonomo et al. [44] argues that a water saturated IPT displays *improved* sensitivity when it is in equilibrium with the environment and the excess water has evaporated. Their experimental data show that IPT sensors saturated with water produce an extremely noisy sensing signal while, after reaching equilibrium with the environment, the same IPT produces a comparatively noiseless signal with notably higher sensitivity. Chen et al. [45] have made similar observations, but observe that as a hydrated sample approaches equilibrium with the environment, sensitivity initially improves but is then followed by decay as the water continues to evaporate from the transducer. Because neither of these reports fully define the IPT initialized or final states it is difficult to draw conclusions, but observation of a fundamentally different tendency for sensing as compared to actuation is clear.

Any proposed sensing mechanism must accommodate other significant observations. For instance, besides diluent uptake, diluent type has been demonstrated to have a significant effect on the magnitude of sensing response; while use of an ionic liquid diluent results in stable

operation (ionic liquids do not evaporate), as compared to water the magnitude of sensing response is diminished [11,12]. Similarly, manipulation of the counterion is known to affect the magnitude of sensing response; a lithium exchanged IPT displays a sensing current that is 5 to 10 times larger than a sodium exchanged IPT [11]. A number of potential explanations are possible, including the effect of diluent viscosity and the tortuosity of selective ionic conduction for counterions of varied sizes. But it is pertinent to recall that manipulation of diluent, counterion, and even base ionomer are also known to affect morphology.

The interdependence between the ionomer material state and the IPT active response are clearly complex. Thus the actual sensing mechanism remains an open topic; this knowledge gap has hampered widespread adoption of these otherwise competitive and potentially superior sensors. Before presenting the mechanisms proposed to date (Section 2.4), it is pertinent to next consider some details in the role of the electrode-ionomer interface.

2.3.2 **IPT Electrodes**

Shahinpoor et al. [16,46] studied the effect of surface-electrode resistance on IPT actuation and argued that the actuator performance is improved when the surface-electrode resistance is lowered by depositing highly conducting metal on top of the platinum electrode. In fact, a recent modeling study has gone so far as to study the effectiveness of the electrode in IPT response, in the absence of ionomer interaction [47]. While that study offers valuable insights into the implications of ‘perfect electrode communication’ assumptions, its failure to consider the active layer offers little insight into the underlying mechanism responsible for IPT sensing.

Returning to electrode architecture experimental studies, recent progress is indicating that the electrode in IPTs plays an important role in IPT electromechanical transduction mechanism.

The relationship between the electrode-ionomer interface and the actuation performance in IPTs has been studied by Akle et al. [13,48,49]. A linear correlation between capacitance and actuation performance in IPTs has been proposed by Akle [48]. This work also presents an IPT fabrication process named the Direct Assembly Process (DAP), which improves IPT *actuation* performance by 50 times. By blending varied volume fractions and types of ionomer, diluent, and conducting powder (for instance, RuO_2), the DAP allows the controllable creation of a wide array of electrode architectures. Most of the studies in Chapter 4 are based on IPTs fabricated by the DAP.

For actuation, a correlation between the generated peak strain and the interfacial surface area between the conductor phase and the ionomer is reported [48]. The actuation strain rate is a function of the content and conductivity of the conductor particle in the electrode [50-52]. While most of the published work on the DAP focuses on IPT actuation, this process can improve IPT sensitivity as well (Figure 2.5). As the thickness and concentration of the electrode increase, the sensitivity increases. However, the experiments also demonstrate that there is an upper bound on this effect. It is hypothesized that a tradeoff exists between the availability of free ions for selective ionic conduction through the transport media, the effective surface area of the electrode, and the interaction of ions with the electrode surfaces [50]. Thus, in addition to accommodating experimentally observed dynamic effects and compositional variation effects, the mechanism responsible for IPT sensing must also accommodate varied electrode architecture effects.

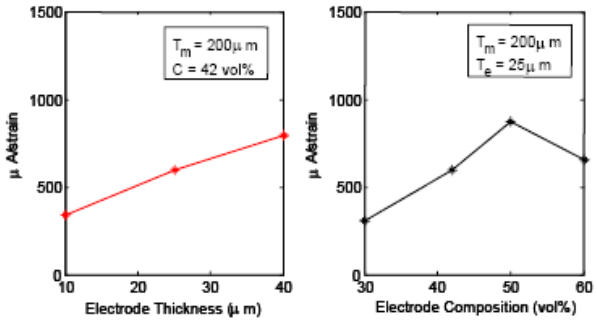

Figure 2.5: The normalized sensing response per unit strain of a RuO_2 based IPT as a function of (a) electrode thickness, and (b) electrode metal composition (volume percent) [50].

2.3.3 **IPT Diulents**

Of all the limitations of IPT applications the one that attracts the most attention is that a diluent is required for IPTs to function. Typically, water is used as the diluent. Using water as the diluent enables IPTs as efficient transducers in aqueous environments. However, it limits the performance of IPTs due to the chemical breakdown of the water molecules at low operating voltages and the water evaporation when operated in open air. Therefore, diluents with good thermal and electrochemical stability are favored to improve the operation stability of IPTs in open air.

An ionic liquid is a salt in the liquid state at relatively low temperature. While ordinary liquids such as water and gasoline are predominantly made of electrically neutral molecules, ionic liquids are largely made of ions, which are typically organic cations and organic or inorganic anions. Recently ionic liquids have been used in Nafion based IPTs for their excellent thermal and electrochemical stability and low vapor pressure [12,49]. Bennett et al. [12] have compared water to ionic liquids as the diluents by applying a 1.5 V (peak) sine wave on a

platinum- and gold-plated Nafion 117 swollen with water and 1-ethyl-3-methylimidazolium trofluoromethanesulfonate (EMI-Tf) ionic liquid. The strain generated by the water swollen IPT sample decreased nearly to zero after about 2000 cycles due to the dehydration of the material when operated in open air. By contrast, the same actuator swollen with EMI-Tf operated for over 250,000 cycles with only 25% decrease of generated strain. In addition, ionic liquid swollen IPTs are demonstrated to operate in air for up to 1 million cyles with a performance loss of less than 43% [53]. Although there are some drawbacks for ionic liquids being used as IPT diluents, such as the decrease of the magnitude of the actuation response and the reduction in the speed of the response, the improvement of the stability of IPTs in open air could potentially increase the applications of IPTs dramatically.

2.4 IPT TRANSDUCTION MODELS

Previous modeling investigations of IPT transduction can be categorized in three classes: (1) empirical models, including black box models and grey box models [10,34,44,45,54], which are useful for narrow ranges of IPT synthesis, (2)‘hydraulic models’ of ion transport-induced deformation [55-57], and (3) electrostatic models [28,30,58].

General ‘hydraulic models’ of ion transport-induced deformation have been proposed by deGennes, et al. [55], Asaka, et al. [56], and Tadokoro, et al. [57]. These models place emphasis on pressure induced fluid motion through an IPT, where ions are presumed to be carried with the fluid motion. These models accurately accommodate the experimental phenomena explored within each of the noted efforts. However, none of the hydraulic models of electromechanical

transduction have been able to represent all types of experimentally-observed phenomena. For instance, in order to successfully identify the physical mechanism responsible for IPT sensing it must first be recognized that a sensing signal may be generated in bending, tension, compression, or shear (not limited to bending).

Of the models intended to address the physics of *sensing*, only the micromechanics approach by Nemat-Nasser and Li has met with some success [28,30]. Consider first the micromechanics aspect of these studies in isolation from sensing. Beginning with an assumption that the Hsu and Gierke cluster morphology applies, their micromechanics approach has been used to study clustering in Nafion [26]. The cluster size r_c is predicted from the minimization of the free energy as a function of the equivalent weight of the ionomer, volume fraction of water, temperature, electrostatic energy, elastic energy due to polymer chain reorganization, and cluster surface energy per

$$r_c^{\,3} = \frac{\gamma_c \left\langle h^2 \right\rangle M_e}{2N_A kT} \frac{\left(\Delta V + \Delta V'\right)}{\rho_d} \left[1 - \sqrt[3]{\frac{4\pi\rho_d}{3\rho^*(\Delta V + \Delta V')}} \right]^{-2} \qquad (2.4.1)$$

where γ_c is the surface energy density of the cluster, $\left\langle h^2 \right\rangle$ is the mean square polymer chain length, M_e is the ionomer equivalent weight, ΔV is volume change with water uptake, $\Delta V' = \frac{N_A V_i}{M_e / \rho_d}$ is the volume fraction of ion exchange sites, V_i is the volume of the ion exchange site, ρ_d is density of the dry polymer, and $\rho^* = \frac{\rho_d + \Delta V \rho_w}{1 + \Delta V}$ is the effective density of the hydrated polymer.

The strength of this micromechanics study is that introduces a tool for assessing morphological evolution as a function of fundamental IPT parameters. This could in turn be

used to assess active response. However a number of significant simplifying assumptions are introduced in its development to enable tractable analytical assessment. Not least among these assumptions is the application of the Hsu and Gierke spherical cluster morphology (as noted above, the morphology is generally accepted as incorrect). Thus this seminal micromechanics study does offer an important tool in assessing the interrelation between ionomer morphology and active response, however it must be imposed with due caution.

The micromechanics study by Li and Nemat-Nasser was subsequently employed as a basis from which active response could be explored, similar to the goals of this thesis. Their work focused on the use of an electrostatics model of electromechanical deformation, which argues that IPT transduction is the result of the electrostatic pressure exerted on polymer clusters due to local charge imbalance (actuation) and is due to the formation of electric dipoles in the polymer clusters under mechanical deformation (sensing). They have also experimentally demonstrated that the response of an IPT depends on the chemical composition and structure of the backbone ionic polymer, the architecture of the metal electrodes, the nature of the counter-ions, and the level of hydration, and that the model is able to accommodate their experimental observations. This approach has subsequently been adopted and somewhat expanded by Porfiri [58] to a plate-like model, which describes the contributions from a variety of IPT constituents and phenomena, including counterion, diluent, and polymer motions, electric dipole generation, osmotic effects, boundary layer formation, polymer swelling, and local charge imbalances. It accounts for charge redistribution inside the IPT and dipole creation induced by mechanical deformations. The constitutive parameters of this plate-like model are expressed in terms of fundamental IPT physical quantities, such as polymer hydration level, IPT dielectric constant, polymer and electrode dimensions and elastic properties, and diluent concentration, which are

consistent with experimental findings. In addition, the work shows that the electromechanical coupling of IPTs is strongly correlated to the capacitance, which is largely independent of the IPT thickness and highly correlated to the thickness of the boundary layers formed by the counter-ions in the vicinity of the electrodes.

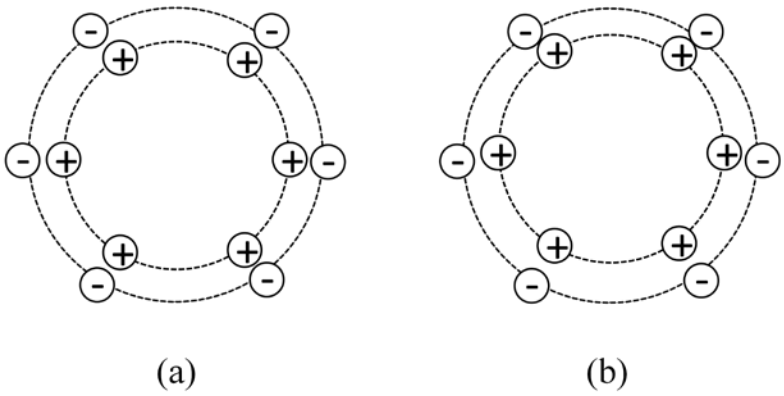

Figure 2.6: Schematic illustration of ionic polymer clusters: (a) ion pairs within a cluster and (b) dipole induced by imposed bending curvature [14].

The strength of these models is their consideration of the breadth of active phenomena present in IPTs, including consideration of morphology. However, the component of these models intended to justify the observation of IPT sensing is the formation of intra-cluster dipoles during deformation. As illustrated in Figure 2.6 the dipole hypothesis assumes the existence of *perfectly paired*, radially oriented pendant ionic groups with electro-neutralizing counterions, residing within *spherical clusters* (the Hsu and Gierke model of Figure 2.2). Under these ideal conditions it is then argued that in bending deformation, per a Poisson effect, the ion pairs will be distorted above and below the IPT neutral axis, resulting in the creation of an effective dipole within each cluster, which in turn gives rise to accumulation of IPT surface charge (sensing response). However, even under these ideal conditions, the described dipole effect cannot exist

under pure shear loading; but as noted above, sensing response under shear loading has been experimentally observed. In addition, the notion of perfect ion pairing stands in contrast to generally accepted mechanisms for actuation response, in which *free* counterions form boundary layers at the transducer's surfaces (see for instance He 2008 [59]); moreover, the models themselves include the assessment of boundary layer formation, and therefore embody contradictory assumptions. Weiland and Leo [31,32] subsequently investigated the equilibrium state of single clusters and concluded that the perfect-pairing assumption is unlikely to be reasonable. Rather, it is suggested that *non-ideal ion pairing enables sensing*. Finally, while the assumption of spherical clusters is often imposed for its simplicity, the preceding morphology discussion draws attention to its optimistic nature; it is unlikely that the dipole theory can be retained for an alternate morphology. Combined these reports call the hypothesis of a polarization mechanism into question.

Recently the mechanism of streaming potential as unpaired ions move relative to covalently affixed pendant ionic groups has been proposed [50,51]. Unlike its predecessors which focus on bending, it has been suggested that the mechanism of streaming potential should be able to predict that a sensing response will be generated for all modes of deformation.

2.5 STREAMING POTENTIAL HYPOTHESIS

To explore the streaming potential hypothesis, consider that it has previously been argued that capacitance in IPTs is mainly due to an electric double layer [48], which forms at the interface between the electrode and the electrolyte [60-65]. It has also been previously established that the existence of a double layer is prerequisite to the observation of streaming potential [66]. Thus, to

begin discussion of the preliminary models of the mechanism of streaming potential in IPT sensing, it is prudent to first review the generalized view of streaming potential.

Figure 2.7 illustrates the fundamental streaming potential concept. When an electrode is submerged in an electrolyte an electric double layer is formed when the ions pass from the high chemical energy metal phase to the lower chemical energy electrolyte phase. If a pressure gradient is applied along the electrode surface and the electrolyte is sheared against the electrode, it will result in a disruption of the electric double layer and generate a potential and a current in the electrode, which are known as streaming potential and streaming current.

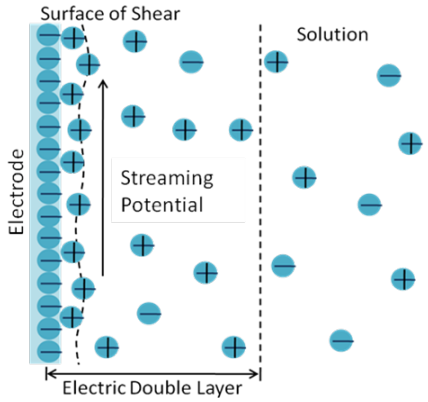

Figure 2.7: Electric double layer and streaming potential

Streaming current and streaming potential are two interrelated concepts in the areas of surface chemistry and electrochemistry. They are part of electrokinetic phenomena. When an electrolyte is driven by a pressure gradient through a channel or porous plug with charged walls, the transport of free ions along with the pressure-driven fluid flow gives rise to a net charge transport, i.e., the streaming current.

For ionic polymers, consider that it has been argued that *imperfect* ion pairing results in the availability of free counterions within the hydrophilic regions [31,32], thereby resulting in

the presence of an electrolyte within these regions. Similarly, the unpaired but covalently attached anions line the walls of these regions. Provided the electrolyte is set into motion with respect to the bound anions, a streaming potential should result. Now considering that there is a net relative motion of this electrolyte with respect to the electrode for all modes of deformation, an impetus exists for the mechanism of streaming potential.

A significant goal of this dissertation is testing the streaming potential hypothesis for IPT sensing. Expanded literature review of streaming potential phenomena at the length scale of typical ionomer morphological features is offered in Chapter 4 to facilitate presentation of the rationale for certain aspects of model development.

3.0 MULTISCALE STIFFNESS PREDICTIONS

This chapter presents a multiscale model for material stiffness and morphology that is prerequisite to exploring streaming current. In parallel with rapid advances in computing power, multiscale material modeling has been receiving increasing attention. The vision is that multiscale modeling might ultimately serve as an alternate laboratory method or as a material design tool [67,68]. In general, multiscale modeling is not yet mature enough for these purposes; the biggest challenges are (1) identifying appropriate methods of modeling at the atomic scale, and (2) identifying appropriate methods to span length and time scales up to the traditional engineering scale [69-71]. However, the basic tenets of multiscale modeling are not new, rather the averaging of lower-length scale effects to anticipate larger-length scale properties has historically been the basis of materials research [72]. This effort adapts strategies from the earlier multiscale approaches (viz., comparatively computationally *un*intensive) to the goal of developing an alternate laboratory tool capable of ~1^{st} order accuracy. The predictions from such a model could guide more intensive studies in ionomeric materials. The work adapts rotational isomeric state (RIS) theory in combination with Monte Carlo (MC) methodology to the creation of a multiscale stiffness prediction model appropriate to ionic polymers. The first two sections provide background and define the method established as part of this dissertation. The third section establishes that the approach is robust for a known case - Nafion. Section 3.4 illustrates

how the method can be adapted to the exploration of lesser known cases - Selemion, appropriate to the optimization of IPT sensing response.

3.1 INTRODUCTION TO ROTATIONAL ISOMERIC STATE THEORY

RIS theory as described by Flory [36] has long been used to build atomic scale models to study deformation trends and material properties in polymeric materials. Many advancements and studies have been conducted regarding RIS including the accurate molecular representations of many polymers including Poly(dimethylsiloxane), Poly(oxyethylene), and Vinyl Polymer Glass [73-75]. The fundamental idea of this approach is that any given bond within a single polymer chain is restricted to a discrete number of possible low energy bond angles (φ as indicated in Figure 3.1), dictated largely by the interaction with the nearest-neighbor bond.

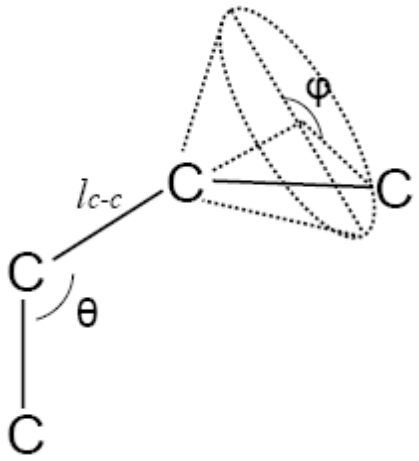

Figure 3.1: Schematic of the spacial geometry of a Nafion molecule [42]

From the RIS theory, a Gaussian analysis is typically imposed to anticipate final chain conformation and corresponding mechanical response. However, application of the Gaussian approach to RIS theory does not represent a reasonable approximation for short chain polymers displaying rubber elasticity. A non-Gaussian theory of rubberlike elasticity, as discussed by Curro and Mark [37], has been developed to simulate the spatial configuration of short chain molecules in a more realistic way by applying RIS theory in combination with a MC methodology. This RIS-MC approach is used to computationally generate a large number of end-to-end distances *r* between crosslinks of the polymer chain (Figure 3.2). The *r*-values are then used to estimate an appropriate probability density function (PDF), and subsequently any number of statistical methodologies may be imposed to predict material response trends.

The Mark-Curro approach has been used to study the effect of particle reinforcement in polymer composites [38,39]. A similar modeling approach to stiffness predictions of hydrated ionic polymers is then proposed by Weiland et al. [41] and Matthews et al. [42], by applying RIS theory in a manner analogous to the particle inclusion works, where inclusion volumes are now taken to be clusters. In addition, it is assumed that these clusters, under specified conditions, may act as backbone cross-linking junctions, such that the ionomer stiffness is based on polymer short chain response (Figure 3.2). Weiland et al. [41] seek to find a relationship between statistical parameters and material stiffness by applying the Johnson family distributions for PDF estimations. Establishing a consistent relationship between these parameters and the corresponding stiffness predictions may ultimately serve as a first step toward the custom design of material stiffness at the synthesis stage. This work demonstrates that using the Johnson family of distributions as the density estimation method introduces stable predictions. However, there

are still sources of error in the approach such as simulation of polymer chain with total lengths that are unrealistically short.

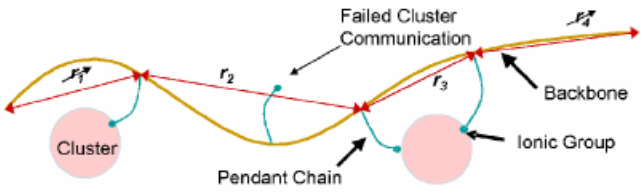

Figure 3.2: End-to-end distance *r* between cross-links for a single Nafion polymer chain [78]

Computational generation of physically realistic total chain lengths is a long standing challenge often requiring significant computational burden [38]. As a result, many studies are forced to assume that the error associated with using artificially repeatable and/or short backbone lengths is within acceptable bounds; see, for example [41,42,76]. The current effort employs the method of Weiland et al. [41] but seeks to computationally attain backbone chain lengths of sufficient length to (1) assess the extent of error associated with artificially short backbone lengths, and (2) identify the simulated chain length requisite for stable stiffness predictions, as detailed in Gao and Weiland [77-79].

3.2 MODELS AND COMPUTATIONAL METHODS FOR NAFION

In this work the mechanical responses of the ionic polymer Nafion in specific forms are considered: 1200 Equivalent Weight (EW), hydrated and containing Li^+ or Na^+ counterions. The model assumes a rectangular cluster orientation analogous to the cubic crystalline structure and

consistent with the idealized morphology proposed by Hsu and Gierke [23] indicating identical spherical clusters uniformly distributed within the polymer matrix and interconnected by channels. It is assumed that the ion exchange is complete and that the sample has been annealed (thereby eliminating semi-crystallinity). The Mark-Curro approach to RIS-MC theory is applied in a manner analogous to that used in particle reinforcement investigations [38,39], such that the chain conformation is excluded from occupying any volume dedicated to a hydrophilic cluster. Further, the polymer backbone may have discrete points of communication with the hydrophilic clusters via the pendant chain attachment points. These attachment points are assumed to approximate cross-linking points, and thus mark an end-point for the given chain length *r* (Figure 3.2).

3.2.1 **Simulation of Polymer Chain Conformation**

To implement this model, geometry of the polymer backbone chain must be identified, through appropriate statistical weight matrices for backbone chain conformation, bond lengths, and distances between pendant chain attachment points. Bulk Nafion material is a complicated network of molecules. An individual Nafion molecule is composed of the repeating monomer unit shown in Figure 3.3, which is repeated by *m* times. The calculations in this dissertation are performed for fully developed Nafion chains having m = [50, 120]. The -$(CF_2CF)(CF_2CF_2)_n$- portion constitutes the hydrophobic backbone of the polymer and SO_3^- is the pendant chain terminal ionic group which is hydrophilic and generally interacts with the nearest cluster. The typical composition of Nafion backbone is 87/13, meaning that there are 13 (CF_2CF) groups for every 87 (CF_2CF_2) groups in the total length of the polymer backbone; thus the value of *n* is most often approximately 7. In the simulation, the actual values of *n* are sampled from a discrete

probability distribution in the range of [5, 11] as summarized in Table 1, with a mean of approximately 7 [42].

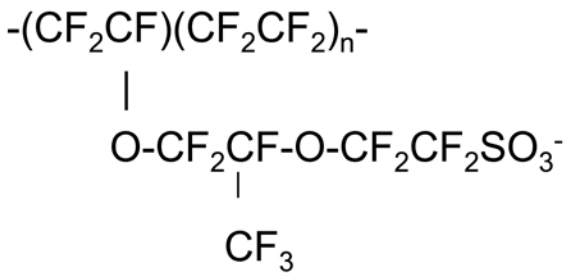

Figure 3.3: Chemical structure of Nafion monomer

Table 1. Discrete probability distribution of *n* values [42]

n	Probability
5	0.1
6	0.2
7	0.3
8	0.2
9	0.1
10	0.05
11	0.05

In the simulation, the polymer chains are placed within a $(5000\ \text{Å})^3$ 3-dimensional grid of spherical clusters. The grid size is selected to accommodate the longest anticipated, fully extended backbone chain in a fully hydrated material sample based on an estimation of Nafion polymer chain length [42]. The cluster distribution scheme is akin to a cubic lattice shown in

Figure 3.4. The center-to-center distance between clusters is determined by the cluster radius and volume fraction.

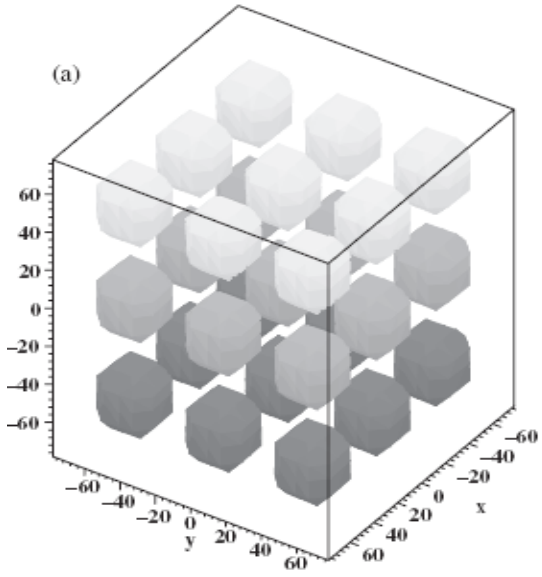

Figure 3.4: Cluster distribution akin to a cubic lattice [42]

Once the cluster distribution is assigned, a starting point of each polymer chain is randomly specified and the backbone is dynamically constructed according to the polymer spacial geometry within the 3-dimensional grid, where cluster locations are excluded. The Nafion backbone takes the form of (CF_2CF_2), or polytetrafluoroethylene (PTFE), based on the simplifying assumption that the presence of the diluent has only a small effect on backbone potentials [80]. For PTFE, as shown in Figure 3.1, the carbon-carbon bond length and in-plane bond angle are fixed at $l_{c-c} = 1.53\,\text{Å}$, and $\theta = 116°$, respectively, while the out-of-plane rotation angle φ corresponding to energy minima must be identified by applying a statistical weight

matrix. Thus PTFE statistical weight matrices are applied to predict Nafion backbone bond angles. Each subsequent bond must be similarly placed.

For PTFE, both 3- and 4-state statistical weight matrices have previously been studied, where 3- and 4- dictate the number of low energy out-of-plane bond angles φ (Figure 3.1). The more physically realistic helical chain coiling in both PTFE and Nafion may be captured only by the 4-state matrices [81,82]. Therefore, the simulation adopts the 4-state model with rotation angles of two *trans* (φ = ±15°) and two *gauche* (φ = ±120°) conformations. The 4-state statistical weight matrices used in this model, as discussed in details in Matthews et al. [42] and Weiland et al [41], are:

$$U_2 = \begin{bmatrix} 1 & 0 & 0 & 0 \\ 0 & \sigma' & 0 & 0 \\ 0 & 0 & \sigma' & 0 \\ 0 & 0 & 0 & 1 \end{bmatrix} \qquad U_3 = \begin{bmatrix} 1 & \sigma & 0 & \omega \\ 1 & \sigma & \sigma\beta & 1 \\ 1 & \sigma\beta & \sigma & 1 \\ \omega & 0 & \sigma & 1 \end{bmatrix}$$

$$U_k = \begin{bmatrix} 1 & \sigma & 0 & \omega \\ 1 & \sigma & 0 & 0 \\ 0 & 0 & \sigma & 1 \\ \omega & 0 & \sigma & 1 \end{bmatrix} \qquad U_n = \begin{bmatrix} 1 & \sigma' & \sigma' & \omega \\ 1 & \sigma' & \sigma'\beta & 0 \\ 0 & \sigma'\beta & \sigma & 1 \\ \omega & \sigma & \sigma' & 1 \end{bmatrix} \qquad (3.2.1)$$

where σ = 0.2, σ' = 2.0, ω = 0.2, β = 0.5 at 25 °C, and the rows and columns are indexed in the order t^+ (+15 °), g^+ (+120°), g^- (-120°), and t^- (-15°). The orientation of the second bond is dictated by U_2, the third by U_3, the last by U_n, and all others by U_k, except when a bond placement coincides with a cluster or when the bond corresponding to a pendant chain attachment point is being placed. These matrices have then been normalized to obtain the conditional probability matrices [36] as,

$$Q_2 = \begin{bmatrix} 1 & 0 & 0 & 0 \\ 0 & 1 & 0 & 0 \\ 0 & 0 & 1 & 0 \\ 0 & 0 & 0 & 1 \end{bmatrix},$$

$$Q_3 = \begin{bmatrix} 0.6552 & 0.2137 & 0 & 0.1310 \\ 0.4017 & 0.1310 & 0.0655 & 0.4017 \\ 0.4017 & 0.0655 & 0.1310 & 0.4017 \\ 0.1310 & 0 & 0.2137 & 0.6552 \end{bmatrix},$$

$$Q_k = \begin{bmatrix} 0.7295 & 0.1246 & 0 & 0.1459 \\ 0.8541 & 0.1459 & 0 & 0 \\ 0 & 0 & 0.1459 & 0.8541 \\ 0.1459 & 0 & 0.1246 & 0.7295 \end{bmatrix},$$

$$Q_n = \begin{bmatrix} 0.2781 & 0.4829 & 0.2144 & 0.0245 \\ 0.3203 & 0.5562 & 0.1235 & 0 \\ 0 & 0.6263 & 0.0556 & 0.3138 \\ 0.1261 & 0.1095 & 0.4863 & 0.2781 \end{bmatrix}. \qquad (3.2.2)$$

These matrices are employed with a random number between 0 and 1 to choose the angle of rotation φ for all bonds in the simulation based on the rotational state of the preceding bond. For example, suppose placement is being attempted of the last bond of a backbone chain where the preceding bond is in the t^+ state. This indicates that the first row of Q_n contains the appropriate conditional probabilities to select the particular φ value for the current bond. A random number generator is invoked to select a random number between 0 and 1. Assume a value of 0.5 is returned. Since $0.278 < 0.5 < (0.278 + 0.482)$, the value $\varphi_n = 120^o$ has been selected.

In Matthews et al. [42] and Weiland et al. [41] when all out-of-plane rotation angles result in cluster coincidence, the chain is terminated. This resulted in the prediction of total chain lengths that were unrealistically short - as compared to the expected number of repeat units *m* being in the range of 135 to 225. In the Matthews et al. and Weiland et al. studies *m* never exceeded 45 but was typically much lower. To avoid early chain termination in the present

effort, when the current bond fails for all out-of-plane rotation angles, the preceding bond is replaced by choosing another low energy conformation (Figure 3.5).

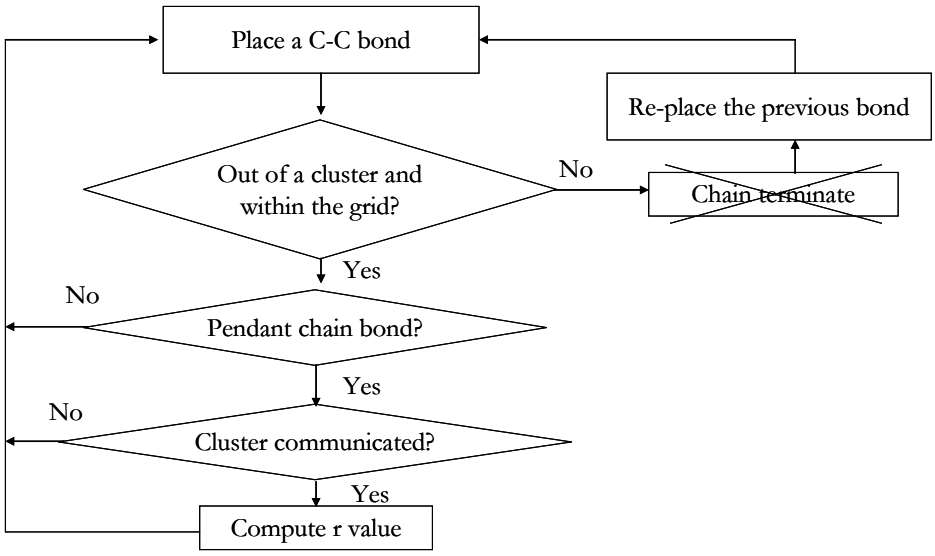

Figure 3.5 Flow chart for the improved RIS model

By this means early chain termination is greatly eliminated, and more realistic *r*-values are generated from polymer chains with *m* up to 120. This approach is also physically consistent with chain reorientation upon hydration.

It is assumed that the pendant chain terminal ionic group successfully communicates with the nearest cluster if the distance between the backbone connection point and the cluster is within 8 Å. This value is an estimate of the fully extended length of the Nafion pendant chain length which has been reported to be in the range of about 5 to 10 Å [83]. Each simulated Nafion backbone chain can have multiple *r*-values as illustrated in Figure 3.2. The free-end effects are eliminated by discarding the first and last *r*-values for each chain because the free ends do not contribute to material stiffness. To assure statistical validity, a large number of *r*-values

(~10,000) are generated for each data set. From this, an appropriate PDF $P(r)$ for the chain length may be estimated.

3.2.2 **Macroscopic Model for Stiffness Prediction**

To compute Young's modulus of the material, Boltzmann's approach to statistical thermodynamics is used in a macroscopic-level model to relate the entropy of the chain $S(r)$ to the estimated PDF $P(r)$ for the simulated polymer chain end-to-end lengths through the expression

$$S(r) = c + k \ln P(r) \qquad (3.2.3)$$

where k is Boltzmann's constant and c is a constant of integration that drops out when the difference in entropy for the unperturbed configuration is taken with respect to the distorted configuration. Under the assumption of rubberlike elasticity, the "three chain" model, as described by Treloar [83], yields the relation

$$\Delta S = \frac{\nu}{3}\left[S(r_o\alpha) + 2S(r_o\alpha^{-1/2}) - 3S(r_o)\right] \qquad (3.2.4)$$

where υ is the number density of network chains, r_o is the root mean square of the simulation-generated r-values and α is the relative length of the sample. The three chain model, in essence, assumes that the simulated polymer chains will tend to align with Cartesian axes.

RIS theory assumes that under load, the rotation about a given bond is unrestricted and thus the Helmholtz free energy is strictly a function of entropy, allowing the nominal stress f^* to be then given by

$$f^* = -T\left(\frac{\partial \Delta S}{\partial \alpha}\right)_T = -\frac{\nu k T r_o}{3}\left[G'(r_o\alpha) - \alpha^{-3/2} G'(r_o \alpha^{-1/2})\right] \quad (3.2.5)$$

where T is the absolute temperature, $G(r) = \ln P(r)$ and $G'(r) = \frac{dG(r)}{dr}$. The corresponding modulus [f^*] is computed from the relation

$$\left[f^*\right] = -\frac{f^*}{\alpha - \alpha^{-2}} \quad (3.2.6)$$

For small strains ($\alpha \to 1$), the modulus [f^*] approaches Young's modulus. The resulting stiffness is subsequently given by

$$E = \frac{-\nu k T r_o}{6}\left\{\frac{r_o P(r_o) P''(r_o) - r_o\left[P'(r_o)\right]^2 + P(r_o) P'(r_o)}{\left[P(r_o)\right]^2}\right\} \quad (3.2.7)$$

and υ is estimated per the method of Weiland et al. [41] by

$$\nu = \frac{\rho N_A}{MW_{c-c}} \quad (3.2.8)$$

where ρ is the material density, N_A is Avogadro's number, and MW_{c-c} is the molecular weight of the portion of the chain between two cluster communication points. The material density is a readily available, experimentally determined value, whereas Avogadro's number is a constant. MW_{c-c} is estimated based on the percentage of successful pendant chain-to-cluster communications. Based on the assumption of n = 7 (Figure 3.3), it corresponds to a molecular weight of the repeat unit of 781 g/mol, where only the backbone is considered to be load bearing. A single failure corresponds to a local MW_{c-c} of $781 \times 2 = 1562$ g/mol. Therefore, if the failure rate is 15%, then $MW_{c-c} = 0.85 \times 781 + 0.15 \times 781 \times 2 = 898$ g/mol [41].

3.2.3 **Statistical Analysis Methods**

In order to apply Boltzmann statistical mechanics (Section 3.2.2), a probability density function $P(r)$ must be created from the collected *r*-values (Section 3.2.1). Application of the traditional cubic spline approach can lead to prediction instability and further suffers from a lack of standardized application strategies [42]. Conversely application of the Johnson family of distributions in the estimation of $P(r)$ is well defined and results in stable predictions. Of the four Johnson family distributions (Unbounded, Bounded, Lognormal, Normal), only the Unbounded and Bounded families are sufficiently flexible for the data generated from the simulation model [41] and are used in this work.

In general, the probability density function $P(r)$ based on the Johnson distributions has the form

$$P(r) = \frac{\delta}{\lambda\sqrt{2\pi}} f'\left(\frac{r-\xi}{\lambda}\right) \exp\left\{-\frac{1}{2}\left[\gamma + \delta \cdot f\left(\frac{r-\xi}{\lambda}\right)\right]\right\} \qquad (3.2.9)$$

where δ and γ are shape parameters, λ is a scale parameter, ξ is a location parameter, for all $r \in H$ the function f is defined according to the applied distribution family, f' is the first derivative of f with respect to r, and f'' is the second derivative of f with respect to r. The Unbounded and Bounded distributions defining f, f' and f'' are

$$f(y) = \begin{cases} \ln(y + \sqrt{y^2+1}), & \text{for the } S_U \text{ (Unbounded) family,} \\ \ln(\frac{y}{1-y}), & \text{for the } S_B \text{ (Bounded) family,} \end{cases} \qquad (3.2.10)$$

$$f'(y) = \frac{df(y)}{dy} = \begin{cases} 1/\sqrt{y^2+1} & \text{for the } S_U \text{ family and all real y,} \\ 1/(1-y) & \text{for the } S_B \text{ family and } y \in (0,1), \end{cases} \qquad (3.2.11)$$

$$f''(y)=\frac{d^2 f(y)}{dy^2}=\begin{cases} -y/(y^2+1)^{3/2}, & \text{for the } S_U \text{ family and all real y,} \\ -(1-2y)/[y(1-y)]^2, & \text{for the } S_B \text{ family and } y\in(0,1). \end{cases} \quad (3.2.12)$$

The bounds on these distributions are

$$H=\begin{cases} (-\infty,+\infty), & \text{for the } S_U \text{ family,} \\ [\xi,\xi+\lambda], & \text{for the } S_B \text{ family.} \end{cases} \quad (3.2.13)$$

Using (3.2.9)-(3.2.13), the function $G(r)$ can be written as

$$G'(r)=\frac{f''\left(\frac{r-\xi}{\lambda}\right)-\delta\cdot\left[f'\left(\frac{r-\xi}{\lambda}\right)\right]^2\cdot\left[\gamma+\delta\cdot f\left(\frac{r-\xi}{\lambda}\right)\right]}{\lambda\cdot f'\left(\frac{r-\xi}{\lambda}\right)} \quad (3.2.14)$$

When this expression is substituted into (3.2.6), the resulting stiffness expression as a function of distortion is given by

$$\left[f^*\right]=\frac{-r_o\nu kT}{3\left[\alpha-\alpha^{-2}\right]}\cdot\left\{\begin{array}{l} \dfrac{f''\left(\frac{r_o\alpha-\xi}{\lambda}\right)-\delta\cdot\left[f'\left(\frac{r_o\alpha-\xi}{\lambda}\right)\right]^2\cdot\left[\gamma+\delta\cdot f\left(\frac{r_o\alpha-\xi}{\lambda}\right)\right]}{\lambda f'\left(\frac{r_o\alpha-\xi}{\lambda}\right)} \\ -\alpha^{-3/2}\cdot\dfrac{f''\left(\frac{r_o\alpha^{1/2}-\xi}{\lambda}\right)-\delta\cdot\left[f'\left(\frac{r_o\alpha^{1/2}-\xi}{\lambda}\right)\right]^2\cdot\left[\gamma+\delta\cdot f\left(\frac{r_o\alpha^{1/2}-\xi}{\lambda}\right)\right]}{\lambda\cdot f'\left(\frac{r_o\alpha^{1/2}-\xi}{\lambda}\right)} \end{array}\right\} \quad (3.2.15).$$

3.3 MULTISCALE STIFFNESS PREDICITONS OF NAFION

RIS-MC simulation of long backbone chains in the presence of inclusions is known to be a substantial computational challenge [38,41,42]. For the material cases of Nafion considered here it is proposed that physically realistic chain lengths have between 135 and 225 repeat units (*m*-values). However, in previous studies of this material system the simulated chain length never

exceeds m = 45, while typical values are much lower [42]. This is due to the early termination while building the backbone chain.

In the current effort the RIS-MC approach is improved so that chain lengths corresponding to m-values in the range of [50, 120] are achieved. Because modest increases in simulated chain length can significantly increase computational burden, identification of the total chain length required for stable predictions is desirable (where it is assumed that total physical chain length may not be necessary because it is the end-to-end chain lengths that dictate the elastic properties of the material.).

In this work, Nafion 1200 EW in Lithium form with 10 vol% water is first studied to identify the chain length that is sufficient to gain stable predictions. Based on the chain length that is identified, Nafion 1200 EW in Sodium form with 10 and 30 vol% of water are then studied to validate the modeling trends for ionomers with different counterions and hydration levels. The cluster size and volume fraction for Nafion in Lithium and Sodium forms are provided in Table 2.

Table 2. Cluster morphology values based on [14]

Counterion	Li^+	Na+	Na^+
Cluster volume fraction	10%	10%	30%
Cluster radius (Å)	13	11	21
Cluster center-to-center distance (Å)	43.8	39.6	50.4

It is significant that the cluster size and distribution differ for the two 10 vol% cases. These values derive from the micromechanics model discussed previously [26]. The electrostatic

energy term in the energy minimization differs between the cases, which causes a shift in the equilibrium cluster size. In turn, the electrostatic energy term differs because the two ions achieve different proximities to the electroneutralizing pendant group based on their physical sizes.

3.3.1 **Nafion 1200 EW in Lithium form**

For the Lithium cases, *m*-values are sampled from several smaller ranges, which are [50, 80], [80, 100], and [100, 120]. A set of *r*-values (about 10,000) is generated for each simulation. Ten sets of data are obtained and analyzed for each of these chain length ranges.

The data sets of r-values are then imported into the software package FITTR1 [84] for statistical analysis. The package incorporates several fitting methods for each of the four Johnson families in the generation of a *P(r)* expression. In this dissertation, estimates of $P(r)$ are generated using combinations of Johnson Bounded and Unbounded distributions. The FITTR1 software also generates the Kolmogorov-Smirnov (K-S) statistic to assess the maximum discrepancy between the empirical (refers to the simulated distribution here) and fitted distributions as a percentage value. Based on the K-S statistic, the diagonally weighted least squares (DWLS) fitting method is selected as the best fit for the Nafion case considered in this study. Brief summaries of the predicted polymer stiffness per the DWLS fitting method for both the Johnson Bounded and Unbounded distributions are provided in Table 3 and Table 4, respectively. Full details of the multiple simulations and corresponding predictions are provided in appendix A.

Table 3. Stiffness predictions [MPa] of Nafion 1200 EW in Li^+ for different *m*-values, Johnson Bounded distribution.

m	50-80	80-100	100-120
Median [MPa]	12.8	13.1	13.0
Standard Deviation [MPa]	0.4	0.5	0.6

Table 4. Stiffness predictions [MPa] of Nafion 1200 EW in Li^+ for different *m*-values, Johnson Unbounded distribution.

m	50-80	80-100	100-120
Median [MPa]	13.8	13.0	13.4
Standard Deviation [MPa]	0.6	0.7	0.8

Attaining longer chain lengths establishes that simulated chain length is an important parameter in this method. In the previous works exploring this method (*m* typically much less than 45), a standard deviation of 3.6 MPa from the predicted median stiffness of 10.0 MPa is sufficient to argue that the method is stable [41]. In the current effort the standard deviation is within a few percent of the mean stiffness of about 13 MPa for all cases; **thus increasing the chain length improves prediction stability by almost an order of magnitude**. In addition, the mean value predicted has modestly increased. However, chain lengths containing more repeat units than [50, 80], while significantly increasing the computational burden, do not offer any further improvements in prediction stability. It is worthy of note that it would be incorrect to perceive a trend of increased stability in the range of [50, 80] as compared to the range of [100,120]; for all ranges considered in this work the K-S statistic is virtually unchanged as chain length increases. The variations in the standard deviation from the median are subsequently also small. Similarly it does not suggest that the predictions employing the Johnson Bounded

distribution are significantly better than those employing the Johnson Unbounded distribution for the case considered in this study.

While the current results yield no significant distinction between the predictions resulting from the Johnson Bounded or Johnson Unbounded distributions, early studies suggest that the Johnson Bounded distribution is preferred [41]. The significant difference between this study and earlier studies is that the root mean square value r_o for the estimated PDFs are nearly identical for Johnson Bounded and Unbounded distributions as illustrated in Figure 3.6. In general, however, r_o for the Johnson Unbounded distribution tends to be larger than that of the Johnson Bounded distribution. In instances where r_o for the Unbounded distribution is in the vicinity of the inflection point of the PDF, application of the Bounded distribution will likely be preferred. The rationale in these cases derives from inspection of equation (3.2.15), where it is observed that the predicted modulus is a function of the PDF, and of its first and second derivatives; these values can oscillate in the vicinity of the inflection point. Further, application of the cubic spline approach is discouraged in this method, as the localized, user-dependent binning of the data can similarly yield local expressions with inflection points or other unstable qualities as compared to the PDF as a whole [41,42].

Moreover, a significant number of computational runs are completed to confirm that 10,000 *r*-values are sufficient to yield a repeatable result; this is substantially fewer than the 30,000 to 80,000 *r*-values previously employed in the RIS-MC approach [37-39]. Thus, a single computational simulation of chains with lengths in the reduced range of [50, 80], and requiring only ~10,000 *r*-values could be employed to repeatably predict bulk material stiffness of Nafion within a range of few percent.

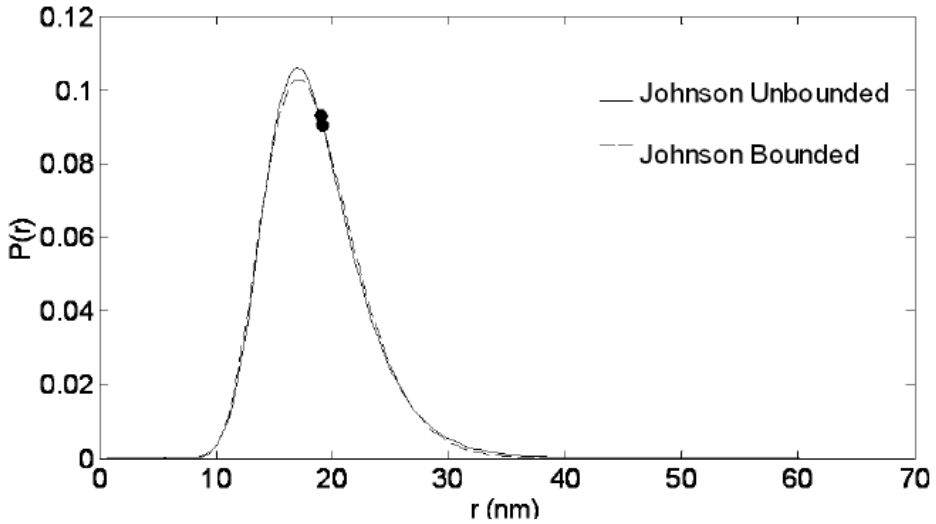

Figure 3.6: Typical Johnson Unbounded and Bounded estimated PDFs and r_o -values of 19.3 and 19.0 Å, respectively, for a simulation including [50, 80] *m*-values.

One of the primary goals of this effort is to establish a repeatable and reliable first order multiscale material property prediction method. The foregoing establishes that the method is repeatable; the reliability of the method must next be considered. Experimental measurement of the bulk stiffness of fully hydrated Nafion 1200 EW in Lithium form suggests a stiffness in the range of ~75 to ~150 MPa [14,23,85] (Difficulties with hydration control are typically reported as the source of error in this experimental measurement.) This experimental value is a measure of the volume averaged bulk material stiffness including semicrystalline regions, hydrophilic clusters, and the net backbone contributions to stiffness. Conversely, the simulation predicts only the net backbone contribution to stiffness, for which there is no reliable experimental measure. Thus a means to compare what is reasonably known from experiment to the prediction must be imposed: a simple rule of mixtures strategy is employed for this purpose.

The rule of mixtures assumes that the stiffness of each constituent contributes to the bulk stiffness in proportion with its volume fraction,

$$E_{ave} = f_{cl}E_{cl} + f_{sc}E_{sc} + f_{bb}E_{bb} \quad (3.3.1)$$

where E_{ave} is the experimentally determined bulk stiffness, E is Young's modulus, f is volume fraction, and the subscripts *cl*, *sc*, and *bb* represent the hydrophilic cluster, semicrystalline, and backbone regions, respectively. For the case when the cluster volume fraction is 10%, f_{cl} would be set to 0.1. But noting that this portion of the bulk material is not expected to support the tensile load imposed experimentally, the stiffness of this region E_{cl} is set to zero. The weight fraction of the semicrystalline regions present in ionic polymers has been reported to be in the range of 3~12% [80]; converting this to volume fraction yields a range of 1.8~7.4%. Experimental studies of the semicrystalline regions of a material that is similarly dominated by a PTFE backbone reports directional stiffness matrix values for the PTFE semicrystalline regions [87]; based on this report, 5000 MPa is a reasonable assumed value for the Young's modulus of a semicrystalline region. If the semicrystalline volume fraction is assumed to be 2%, then the remaining polymer matrix must make up 88% of the volume. Imposing the simulation predicted stiffness of 13 MPa for this remaining volume in Equation (3.3.1) results in the prediction of a bulk material stiffness of 110 MPa, which is well within the range of experimentally reported stiffness for bulk Nafion in Li^+ form [14].

In the foregoing rule of mixtures analysis it is convenient to select a 2% semicrystalline volume fraction because, (1) using round numbers avoids the implication of artificially high levels of prediction precision, while (2) simultaneously illustrating that a reasonable prediction is within the bounds of the analysis. However, it must be recognized that the high stiffness of the

semicrystalline region dominates the prediction. Thus the most significant observation that is drawn from this analysis is that the predicted 13 MPa contribution to stiffness from the polymer backbones is within an appropriate range.

Alternatively, consider that hydrated Nafion in acid form (*viz*., H^+ rather than Li^+ cations) has similar bulk stiffness to that in Lithium form, with an experimentally reported range of ~100 to ~130 MPa. Acid form Nafion hydrogel (no significant semicrystallinity) has been reported to have a stiffness of ~15 MPa [87]. Again, the presence of water in the samples obscures the polymer backbone contribution to the measurement. Because the details of the Nafion morphology in H^+ form differ from that of Li^+ form, detailed comparison of the two cases should be viewed with caution. However, these measurements provide a reasonable frame of reference that supports the perspective that the predicted backbone stiffness of ~13 MPa is within reason (and more specifically, is *not* artificially low).

3.3.2 **Nafion 1200 EW in Sodium form**

The stiffness predictions of the Nafion 1200 EW in Lithium form have been demonstrated to be stable and reliable. The RIS-MC approach is then used for Nafion 1200 EW in Sodium form in order to further check the validity of the approach for Nafion with different counterions and hydration levels. The cluster morphology used in the Sodium case is shown previously in Table 2. The foregoing effort has demonstrated that *m* in the range of [50-80] is sufficient to get repeatable and reliable stiffness predictions for Nafion 1200 EW in Lithium form. Therefore, for the Sodium cases, *m* is randomly distributed in the range of [50-80]. Since the prediction results of Lithium case show good stability with a standard deviation of only a few percent, only three data sets are generated for each of the Sodium cases. The statistical analysis of Lithium cases

does not suggest any superiority between Johnson Bounded and Unbounded distributions, which means that either of the two distributions could be used. In this work, only Johnson Bounded distribution is employed for the Sodium cases.

The stiffness predictions of Nafion 1200 EW in Sodium with 10 and 30 vol% of water by Johnson Bounded distribution are summarized in Table 5 and Table 6, respectively. The resulting stiffness for the two cases are about 26.2 MPa and 15.6 MPa, respectively. The prediction results retain the stability with a standard deviation of a few percent.

Table 5. Stiffness predictions [MPa] of Nafion 1200 EW in Na^+ with 10 vol% water

r_o	Stiffness
18.55	26.2
18.59	24.3
18.57	27.3
Median	26.2
Standard Deviation	1.6

Table 6. Stiffness predictions [MPa] of Nafion 1200 EW in Na^+ with 30 vol% water

r_o	Stiffness
19.76	15.5
19.57	16.0
19.55	15.6
Median	15.6
Standard Deviation	0.2

For consistency, the rule of mixtures is applied to the sodium predictions akin to that for the lithium prediction to assess their reliability. As the volume fraction of cluster f_{cl} changes, the volume fraction of backbone regions f_{bb} changes accordingly. For the cases when the cluster volume fraction is 10% and 30%, f_{cl} would be set to 0.1 and 0.3. If the semicrystalline volume fraction f_{sc} is assumed to be 2% for Nafion with 10 vol% water, then the remaining polymer matrix must make up 88%. Based on this assumption, the semicrystalline volume fraction for Nafion with 30 vol% water would be 1.6%, and the remaining polymer matrix would make up 68.4% of the total volume. Imposing the predicted stiffness values in Table 5 and Table 6, the predictions of bulk stiffness of Nafion in Sodium form with 10 and 30 vol% hydration are 123 MPa and 90 MPa, respectively. The prediction trends are consistent with the experimental observation that Nafion with higher hydration level is softer than the polymer with lower hydration level.

Table 7. Stiffness predictions of Nafion 1200 EW in Li^+ and in Na^+.

Counterion	Hydration level [vol%]	Backbone Stiffness [MPa]	Bulk Stiffness [MPa]
Li^+	10	13.8	110
Na^+	10	26.2	123
Na^+	30	15.6	90

3.3.3 **Discussion**

The stiffness predictions for all the three cases presented previously are summarized in Table 7. For the same hydration level (*viz*., 10 vol%), the predicted backbone stiffness of the Sodium case is significantly larger than that of the Lithium case. Thus the prediction suggests that for different counterions, even for the same hydration level, a different material stiffness should be expected. Further, this prediction was affected by the different clustering imposed for the two cases, where variations in electrostatic energy resulted in the imposition of smaller, more densely packed clustering for the sodium case. Whether or not the imposed spherical cluster morphology akin to that of Hsu and Gierke is strictly true, it is reasonable to expect that the nature of clustering would be similarly affected for other morphological postulates.

It is next noted that the prediction is consistent with the experimental observations that the stiffness of dry Nafion polymer correlates with the radius of the alkli metal counter-cation in the polymer [14]. It is argued that in general larger cations result in larger observed dry polymer stiffness. This is again consistent with the influence of the electrostatic term in the evolution of morphology, and subsequently on the energy state of the surrounding polymer. Therefore, the RIS-MC prediction that the backbone stiffness of Nafion in Sodium form is larger than that of Lithium form is argued as reasonable.

Consider next the predictions for the same counterion (Sodium), but for different hydration levels. For the sodium cases of 10 and 30 vol% water the predicted backbone stiffness is 26.2 and 15.6 MPa, respectively. Compared with the 10 vol% of water case, the mean root square of chain length r_o for 30 vol% of water case is larger, and hence the stiffness is smaller. But the relative magnitudes may be initially counterintuitive. Namely, how could the sample

ever achieve 30 vol% when the elastic energy barrier at 10 vol% would necessarily be significant, and therefore resist the additional uptake? But consider next that achieving optimum uptake requires boiling. Simply soaking the sample at room temperature will not suffice; these room temperature predictions are consistent with that observation. While the assessment presented here does not address the process of how the additional energy associated with boiling results in 30 vol%, it does predict that once the sample has achieved this maximum hydration, it will retain that hydration at room temperature so long as it is stored in water. In other words, the prediction is consistent with the reality that once this hydration level does exist, the elastic energy tending to expel that water is reduced. Only upon exposure to open air will the excess water be expelled. Thus the prediction of decreased local stiffness with increased hydration, while initially counterintuitive, is consistent with experimental observation.

The last point of discussion addresses the utility of a method that can reasonably predict a stiffness value that is experimentally difficult or impossible to measure. For instance, the preceding discussion of energy barriers to water uptake illustrates the role that local stiffness can play in morphology evolution; these parameters are also important in understanding active response. However access to this local stiffness parameter is experimentally impossible. Thus, in light of the fact that multiscale methods, in general, have not yet reached the requisite maturity to routinely and accurately achieve such predictions, the ~1^{st} order accuracy provided by the presented method becomes an important tool. Other significant parameters could similarly be assessed, such as the stiffness of the pendant chains. In the case of this alternate stiffness parameter, even indirect assessment of available experimental characterizations, such as the rule of mixtures analysis imposed here, is impossible. The importance of this parameter in the mechanism of ionic transport for fuel cell applications has been considered [24,25]. Similarly,

the importance of this parameter in actuation/sensing applications has been discussed [26,31]. However, in each of these efforts, because of the lack of viable experimental or modeling strategies to yield insight into the actual stiffness, an artificially imposed value is instead employed. The method presented in the current effort offers a viable strategy with only modest computational burden, for predicting this stiffness value, and subsequently enabling more informed assessment of the mechanisms responsible for ionic polymer active response.

The foregoing describes one potential application for the modeling methodology described in this effort. But the approach has considerable versatility. Because the magnitude of the predictions assessed in detail in this effort are both reasonable and stable, it is conceivable that the approach could be similarly useful in the prediction of other properties (for instance, polarization evolution in PVDF), as well as in guiding otherwise computationally intensive materials studies. The next section offers one illustration of the method's versatility through morphology prediction of a lesser known ionic polymer.

3.4 MULTISCALE STIFFNESS PREDICTIONS OF SELEMION®

The intent of the forgoing study was to establish, for a well known case, that the RIS-MC method is robust. In this case an often studied IPT sensor case was considered – namely an IPT employing a Li^+ exchanged, 10 vol% of water, Nafion 1200 EW ionic polymer layer. However, the ultimate intent of identifying underlying response mechanisms is to use this understanding to enhance response via, for instance, utilization of alternate constituents. Having established that the method is robust, it may next be employed to forecast properties of lesser known candidate systems, or of material properties that are experimentally inaccessible. For instance, in a

subsequent companion study the method was employed as part of an iterative strategy to predict morphology, as detailed in the next sections.

3.4.1 **Introduction to Selemion®**

While the acidic polymer electrolyte membrane (PEM) Nafion has garnered considerable attention, the active response of basic PEMs offers another realm of potential applications [14,30]. The basic PEM Selemion® has been considered for use in desalination processes as well as in the development of a CO_2 separation prototype device (Figure 3.7) [79]. Moreover, like the acidic counterpart, a basic ionomer relies on selective ionic conduction, and could therefore be considered in IPT development. However, Selemion® has not yet been studied as much as Nafion.

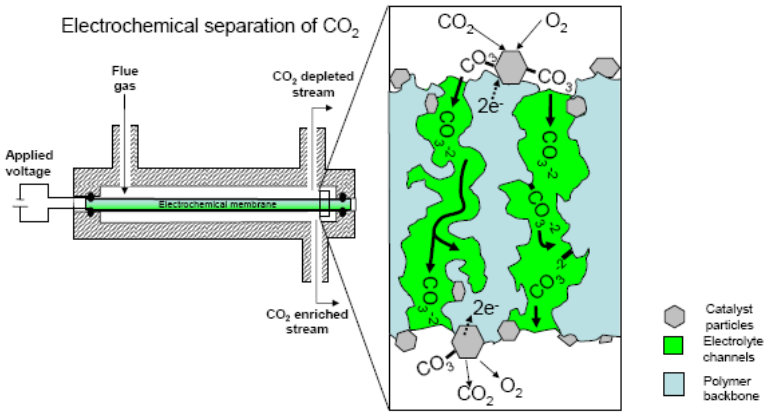

Figure 3.7: An elecetrochemical separation module for carbon dioxide [79]

The mechanical response of Selemion® AMV 500 EW with carbonate counterion is considered. A cluster distribution akin to a cubic lattice is imposed. It is assumed that the ion

exchange is complete. To implement the RIS-MC model the Selemion® backbone chain conformation must be identified through appropriate statistical weight matrices for bond angles and lengths, and distances between pendant chain attachment points.

Selemion® is a copolymer of styrene, chloromethylstyrene, and divinylbenzene, which is manufactured by copolymerizing these three components and introducing a trimethyl ammonium as the ion exchange group. Bulk Selemion® material is a complicated network of molecules, as shown in Figure 3.8. Styrene and divinylbenzene only contribute to building the network of the material and, consequently, stability; chloromethylstyrene is the component that is able to be attached by a pendent chain. There is little information available about the exact structure of individual Selemion® molecules, while the backbone of this kind of polymer is composed of styrene. Although the Selemion® backbone is a complicated network rather than a single backbone chain, the conformational characteristics of polystyrene (PS), which have been studied by using conformational energy calculations [88], may be used in our simplified model to perform a preliminary study of the properties of Selemion®.

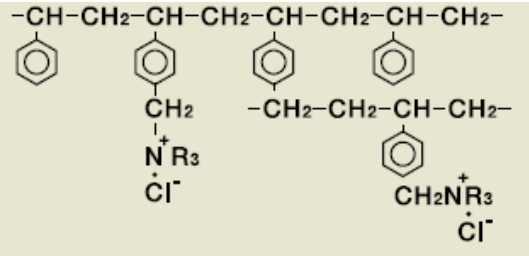

Figure 3.8: Structure of Selemion® network.

In this model, the Selemion® molecule is considered as composed of the repeating monomer unit -$(CH_2CHC_6H_4CH_2NR_3)(CH_2CHC_6H_5)_n$-, which is repeated by *m* times. The -$(CH_2CH)(CH_2CHC_6H_5)_n$- portion constitutes the backbone of the polymer and NR_3^+ (i.e., may be

$N(CH3)_3^+$) is the pendant chain terminal ionic group which is hydrophilic and generally interacts with the nearest cluster. Based on the assumption of a PS form for the backbone, the composition of this backbone can be calculated from the equivalent weight of Selemion®. Based on the equivalent weight of the specific case considered, the value of *n* is approximately 3.68. In this simulation, the actual values of *n* are sampled from a discrete probability distribution on the range [0, 7], with a mean of approximately 3. The discrete probability distribution for n values is shown in Table 8. Since the actual molecular weight of Selemion® is not readily available, the *m* value used in this simulation is chosen based on the preceding studies, which show that an *m* value of 50-80 is sufficient for non-terminated Nafion polymer chains to obtain stable stiffness predictions [78]. It is also found that in all the data sets of *r*-values for a certain chain length range, the *r*-values are mostly from polymer chains with m equals to 50. This is because a small increase in polymer chain length increases the computational burden significantly and longer the polymer chain is much more likely to encounter an early termination. Therefore, chain length of $m = 50$ is chosen for the case of Selemion® 500 EW in carbonate form.

Table 8. Discrete probability distribution for n values of Selemion®

n	Probability
0	0.05
1	0.1
2	0.25
3	0.25
4	0.15
5	0.1
6	0.05
7	0.05

3.4.2 **RIS-MC Model for Selemion®**

In the simulation model, the polymer chains of Selemion® are placed into a certain arrangement of spherical clusters within a 3-dimentional grid of (5000 Å)^3. A cluster distributions scheme analogous to cubic crystalline structure is imposed. The cluster size r_c for this case is calculated using the micromechanics approach presented by Li and Nemat-Nasser [26] as introduced in Chapter 2.

Once the cluster distribution is assigned, a carbon-carbon bond is randomly placed in the 3-dimentional grid, where cluster locations are excluded. For PS the carbon-carbon bond length and in-plane bond angle are fixed at l = 1.53 Å, and θ = 112°, respectively, while the out-of-plane rotation angle must be identified by applying a statistical weight matrix, where it is understood that various angular orientations between bonds correspond with local low energy conformations. Each subsequent bond must be similarly placed. The conformational characteristics of PS have been studied by using conformational energy calculations [88]. PS has three isomeric forms: isotactic PS (iPS), which has pure meso dyads, syndiotactic PS (sPS), which has pure racemic dyads, and atactic PS, which has a mix of meso dyads and racemic dyads. The simulation adopts the 2-state model with rotation angles of 10° and 110°. The 2-state statistical matrix applied for meso dyads is applied, which is

$$U_m'' = \begin{bmatrix} \omega'' & 1/\eta \\ 1/\eta & \omega/\eta^2 \end{bmatrix} \qquad (3.4.1)$$

where $\omega \approx \omega' \approx 0.046$, $\omega'' \approx 1.80$, and $\eta \approx 0.80$ were identified by the means provided in [88], and the rows and columns are indexed in the order 10° and 110°. The matrix has then been normalized to

$$Q = \begin{bmatrix} 0.7330416 & 0.2669584 \\ 0.9705067 & 0.02949325 \end{bmatrix} \qquad (3.4.2)$$

and the orientation of the second bond is dictated by it, except when a bond placement coincides with a cluster or when the bond corresponding to a pendant chain attachment point is being placed. It is assumed that the pendant chain terminal ionic group successfully communicates with the nearest cluster if the distance between the backbone connection point and the cluster is within 7 Å. This value is an estimate of the fully extended length of the Selemion® pendant chain.

To avoid early chain termination, the previous bond is replaced by choosing a minor low energy conformation similar to the work presented in previous section [77,78]. By this means the chain termination is postponed. Therefore, more realistic *r* values are generated. Each simulated Selemion® backbone chain can have up to 50 *r* values. The free-end effects are also eliminated by discarding the first and last *r* value for each chain as before. To assure statistical validity, a large number of *r* values (about 10,000) are generated. From this, the probability density function *P(r)* for the chain length may be estimated using Johnson family distributions per the computational methods presented in section 3.2.

3.4.3 **Results and Discussions**

Fully hydrated Selemion® 500 EW polymer with cubic cluster orientation is considered. It is assumed that the ion exchange is complete. In equation (2.4.1), repeated here for convenience

$$r_c^{\,3} = \frac{\gamma_c \left\langle h^2 \right\rangle M_e}{2 N_A k T} \frac{(\Delta V + \Delta V')}{\rho_d} \left[1 - \sqrt[3]{\frac{4\pi\rho_d}{3\rho^*(\Delta V + \Delta V')}} \right]^{-2} \qquad (3.4.3)$$

the initial guess of mean square polymer chain length $\langle h^2 \rangle$ for Selemion® is chosen as the mean square Nafion chain length from RIS-MC calculation. Imposing input values with ranges consistent with the current understanding of Selemion®, the cluster radius is predicted to be 24.2 Å. The parameters are provided in Table 9.

Table 9. Parameters and results of calculation for cluster size in Selemion®

Equivalent Weight (g/mol)	500	Temperature (K)	300
Dry density ρ_d (g/cm^3)	1.20	Wet density ρ_m (g/cm^3)	1.16
Water Content (weight percent)	21%	Water Content (volume percent)	25%
Effective density ρ^* (g/cm^3)	1.19	Surface Energy Density (N/m)	0.0036
Radius of Cluster r_c (Å)	24.2	Mean distance between cluster (Å)	59.8

With these parameters, the end-to-end chain lengths of Selemion® are generated by RIS-MC method, which are then used to predict the polymer stiffness. A brief summary of the predicted Selemion® polymer stiffness per the DWLS fitting method for the Johnson Bounded distribution are provided in Table 10. The cluster size is also recalculated by using the simulated Selemion® chain lengths. The resulting cluster radius is 2.42 nm. With this number, per the RIS-MC approach, the Selemion® stiffness is predicted to be 1.24 MPa, which is within the tolerance, which means the foregoing predictions are good and no iteration is required.

Table 10. Stiffness predictions for Selemion® [MPa], m=50, Johnson Bounded distribution.

r_o	Stiffness
15.05	1.18
15.55	1.11
14.42	1.50
15.16	1.17
15.41	1.16
Mean	1.22
Standard Deviation	0.16

The resulting stiffness predictions are too low. Volume averaged stiffness of hydrated Selemion® is on the order of 600 MPa; per the rationale of the Nafion discussions, it is not appropriate to directly compare the predicted local stiffness to this experimentally determined global stiffness, it is still reasonable to infer from this experimentally available parameter that the predictions are too low. Given the simplifying assumption employed in this preliminary study, this is to be anticipated. Namely, because the network structure of Selemion® molecule is simplified as a single backbone rather than a branched system (Figure 3.9), the predicted crosslink density is too low. The stiffness prediction of Selemion® could be improved to achieve more realistic results by expanding the simplified backbone of Selemion® to a more complex branched structure and applying more mature statistical matrices.

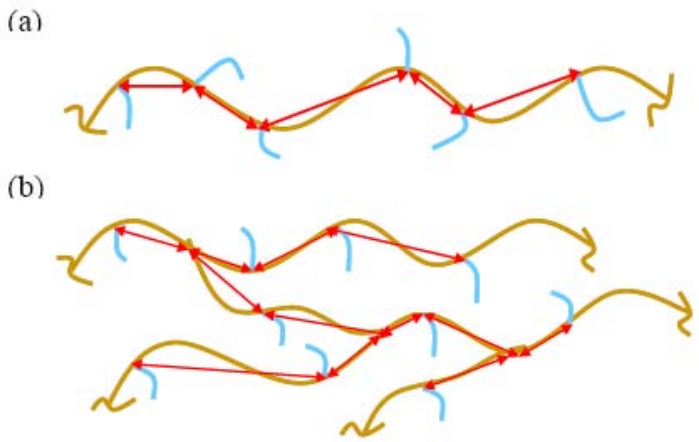

Figure 3.9: Backbone strucutre of Selemion® (a) our model – single backbone chain (b) the real branched backbone chain.

However, as shown in Table 10, the simulated stiffness values of this method continue to be stable for an alternate material system (as previously demonstrated for Nafion). As model complexity is increased, it may be reasonable to assume that this multiscale method will continue to demonstrate the ability to generate reasonable macroscopic property predictions.

The foregoing discussion of the prediction of Selemion® morphology demonstrates the utility of the RIS-MC method developed in this dissertation for predicting parameters that are currently unavailable. While other demonstrations become little more than an academic exercise, the method could be similarly employed for the prediction of material parameters that are experimentally inaccessible. Significant among these is the prediction of pendant chain stiffness in specific ionomer/diluent/cation cases.

It has previously been argued that pendant chain stiffness plays an important role in the concentration of inter-cluster free (unpaired) cations. In the next chapter this concentration is again estimated for a well studied IPT case. However, novel ionomer/diluent/cation cases will

require a method to estimate this value where the foregoing offers that functionality via a relatively straight forward, computationally *un*-intensive platform.

4.0 STREAMING POTENTIAL METHOD FOR MODELING THE ELECTROMECHANICAL RESPONSES OF IONIC POLYMER TRANSDUCERS

In this chapter, a modeling construct for exploring the hypothesis of streaming potential in ionic polymer transducer (IPT) sensors is presented. The streaming potential hypothesis arises from the argument that incomplete pairing of covalently attached pendant ionic groups with their electro-neutralizing counterions establishes the existence of a charged electrolyte within the ionic polymer [31,32]. This electrolyte exists in the hydrophilic phase of the otherwise hydrophobic material. Under mechanical stimulation the electrolyte flows past electroded regions interspersed within the hydrophobic phase, generating a streaming potential in the electrode. To well illustrate the streaming potential hypothesis, the parallel water channel morphology in Nafion membrane recently proposed by Schimdt-Rohr and Chen [29] is employed in the model. The first section (4.1) introduces the streaming current in a single channel. In the second section (4.2) the first generation model is developed for the parallel water channel morphology and successfully addresses the physics of sensing in IPT bending. The effect of electrode architecture is considered in Section 4.3, while variation of the ionomer state (diluent and counterion) are considered in Section 4.4. Section 4.5 explores the implications of varied ionomer morphology. Section 0 expands the model to address transient effects, such as signal decay under DC deformation. Section 4.7 explores the specific case of response for varied input stimulus rates. The chapter is then closed with concluding discussion in Section 4.8.

4.1 THE STREAMING POTENTIAL HYPOTHESIS

As a starting point, and for its ease of implementation, the parallel water channel morphology proposed by Schmidt-Rohr and Chen [29] has been employed *a priori* to explore the streaming potential hypothesis. Later sections of this chapter will explore the implications of alternate morphological propositions. Further, model development focuses on bending; arguments for the existence of a streaming current for other modes of deformation are offered in later sections.

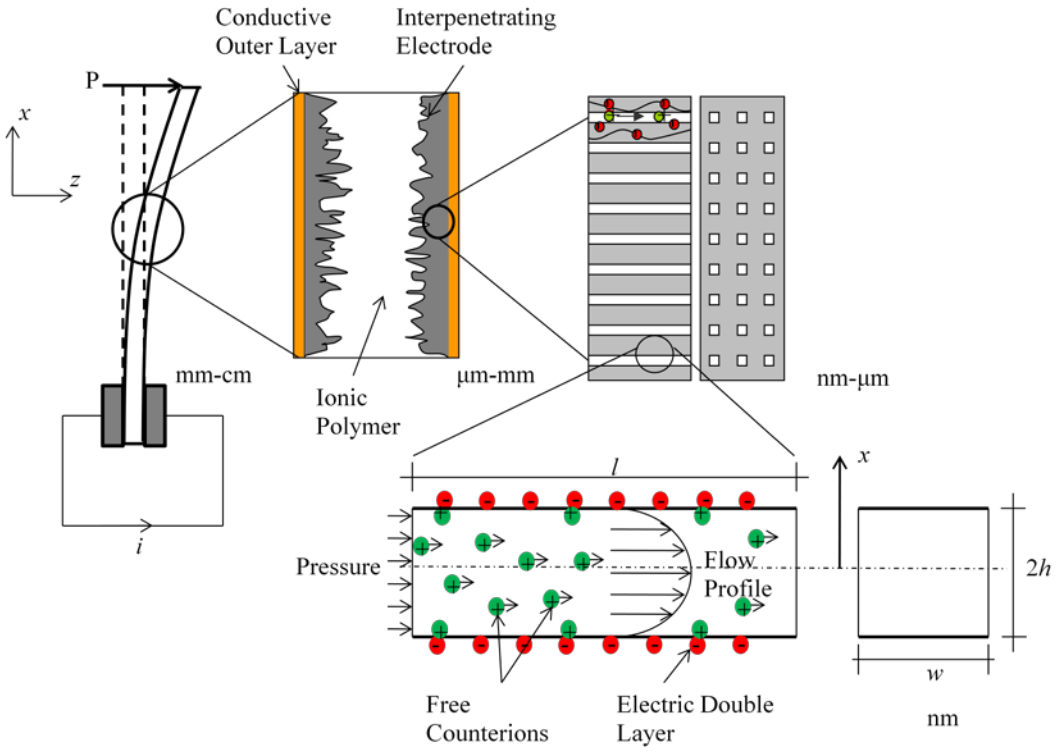

Figure 4.1: Schematic illustration of the multiscale structures of an IPT and the origin of the streaming current in a channel

The preliminary model begins by considering a pressure-driven flow (*i.e.*, via IPT bending) of electrolyte in a rectangular channel. The streaming current generated in a transducer

can be predicted as the sum of the streaming currents in all the channels. Figure 4.1 illustrates how the streaming potential phenomenon may manifest itself for flow through a channel displaying an electric double layer at the surfaces. When a pressure gradient is applied along the channel, some of the ions in the double layer shear against the channel wall and are carried by the flowing fluid, and a streaming current I_s is established.

The streaming current I_s generated in a single channel is equal to the product of the charge density of the flowing fluid, $\rho(x)$, and the local speed of the fluid, $v(x)$, integrated over the cross section of the channel [89]:

$$I_s = w\int_{-h}^{h} \rho(x)v(x)dx \qquad (4.1.1)$$

where x is the height from the channel midplane, w is the channel width, and h is half of the channel height (Figure 4.1). The flow velocity distribution can be described by a Poiseuille flow subject to the no-slip boundary conditions at the walls:

$$v(x) = \frac{1}{2\eta}\frac{\Delta p}{l}(h^2 - x^2) \qquad (4.1.2)$$

where Δp is the pressure drop between two points a distance l apart along the channel, and η is the viscosity of the flow. The local charge density in the electrolyte is zero beyond the electric double layer. Therefore, only the charges on the shear surface of the electric double layer contribute to the streaming current. In other words, of that flow, generally only the portion that is within one Debye length κ^{-1} (~ the distance over which the double layer extends) is of consequence. Thus, in the electrolyte that lies within one Debye length of the solution, where $x = h - \kappa^{-1}$ and κ^{-2} is negligible, the flow velocity is

$$v_{\kappa^{-1}} = \frac{h}{\kappa\eta}\frac{\Delta p}{l} \qquad (4.1.3)$$

If the charge density $\rho(x)$ at the surface of shear is taken as a constant ρ_s , when a pressure gradient is applied, a streaming current is established as,

$$I_s = 2wh\rho_s v_{\kappa^{-1}} = \frac{2wh^2\rho_s}{\kappa\eta}\frac{\Delta p}{l} \qquad (4.1.4)$$

.

Equation (4.1.4) holds in general when the channel size is relatively large. A recent work by Daiguji et al. [90] has demonstrated that when the channel size is on the order of or smaller than the Debye length, the electric double layers of two adjacent walls overlap. In this case the general relationship between streaming current and the flow velocity no longer applies. Instead, they argue that the channel becomes a unipolar solution of counterions at a concentration that neutralizes the surface charge of the channel. The coions are essentially repelled from the channel. If the pressure bias is applied between two ends of the nanochannels filled with a unipolar solution of counterions, only the solution of counterions can pass through the nanochannels so that the streaming potential and streaming current are generated. When this theory applies, *i.e.*, the Debye length is greater than the channel size, the charge density can been seen as constant throughout the solution. So, the streaming current in a single nanochannel is determined by integrating the product of the charge density and the flow velocity over the cross section of the channel

$$I_s = w\int_{-h}^{h}\rho(x)v(x)dx = w\int_{-h}^{h}\rho_e\frac{1}{2\eta}\frac{\Delta p}{l}(h^2 - x^2)dx = \frac{2wh^3\rho_e}{3\eta}\frac{\Delta p}{l} \qquad (4.1.5)$$

where ρ_e is the charge density of the unipolar solution.

Projection of the streaming current requires populating the right hand side of equations (4.1.4) and (4.1.5). In this work the dimensions *w* and *h* are selected such that they are consistent with that of the Schmidt-Rohr and Chen nanochannel model [29]. The macroscopically determined viscosity of the diluent may also be employed with the understanding that a more correct value would still be treated as a constant and therefore have no impact on the *trends* of interest. The remaining terms must be calculated or inferred by other means as follows in the next section. Whether equation (4.1.4) or equation (4.1.5) should be employed in the model, (*viz.* whether Daiguji's theory applies) depends on the relative dimensions of the channel and the Debye length of the electrolyte, which is determined by

$$\kappa^2 = \frac{2e^2 n}{\varepsilon \varepsilon_o kT} \tag{4.1.6}$$

where ε_o is the permittivity of vacuum, ε is the dielectric constant of water, k is Boltzmann constant, T is temperature, e is the electron charge, and n is the number density of the monovalent ions defined by

$$n = \frac{1}{2} N_A \cdot \sum [i] \tag{4.1.7}$$

where N_A is Avogadro's number, and $[i]$ is free ion concentration.

4.2 PRELIMINARY MODEL FOR IPT SENSING IN BENDING

In this section an IPT cantilever beam that is fabricated from Nafion membrane plated with conductive metal electrodes is considered. Based on the hypothesis of the parallel nanochannel ionomer morphology, it is assumed that the hydrophilic regions of the membrane are parallel

nanochannels perpendicular to the surfaces of the membrane and uniformly distributed (Figure 4.1 and Figure 4.2). This corresponds to an assumption of 100% alignment of channels with flow direction for bending. This is an optimistic assumption invoked for mathematical simplicity. The preliminary model assumes that the interpenetrating electrodes are sufficiently interspersed for the resulting current to be communicated to the IPT electrodes. The nanochannel in the model has a height and width of $2h = 2.4$ nm and $w = 2.4$ nm, which are from the average diameter of the cylindrical nanochannel proposed by Schmidt-Rohr and Chen [29]. The channel length is taken to be the depth of electrode. It is optimistically assumed that the electrodes communicate with all nanochannels in that depth completely.

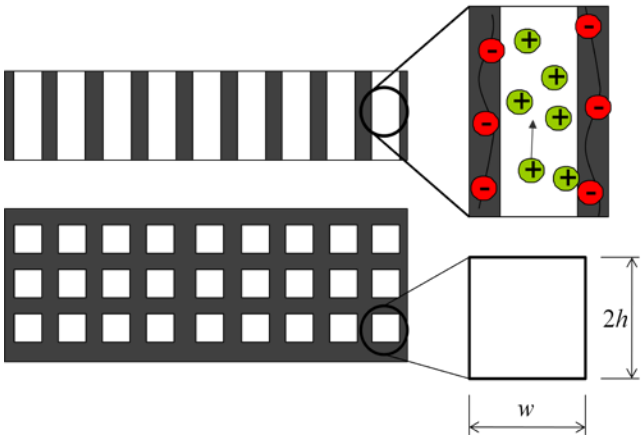

Figure 4.2: Selective ionic conduction in parallel nanochannel model

Due to the extreme small size of channels, it is necessary to compare the Debye length of the IPT diluent with the channel size to determine if Daiguji's theory applies [90]. The actual Debye length is not accessible. In order to establish a viable frame of reference, consider that for two widely different diluent concentrations of 1 M and 0.001 M KCl solutions, by equations

(4.1.6) and (4.1.7), the Debye lengths are 9.75 nm and 308 nm, respectively, both of which are greater than the 2.4 nm channel size proposed by Schmidt-Rohr and Chen [29] and are in turn greater than the channel size in previously proposed morphologies. It is therefore deemed probable that Daiguji's theory applies and equation (4.1.5) is employed. Moreover, as model evolution is presented in later sections of this chapter, the assumption is retained that Daiguji's theory applies.

4.2.1 **Charge Density in Small Channels**

The charge density can be calculated based on the Weiland and Leo prediction of unpaired counterions in equilibrium Nafion [31,32]. The concentration of unpaired ions per unit volume may be used directly to estimate charge density such that,

$$\rho_e = \frac{n_f e}{V_{fl}} \tag{4.2.1}$$

where n_f is the number of free ions, e is the elementary charge, and the volume of the fluid V_{fl} is

$$V_{fl} = V_{cl} - n_{an} V_{anion} - n_p V_{cation} \tag{4.2.2}$$

where the number n and volume V of the counterions and ionic groups are treated as non-negligible.

4.2.2 **Pressure Difference for Bending Mode**

The instantaneous pressure gradient in the nanochannel can be estimated from the stress difference between the two sides of the membrane. For a cantilever beam with an end load P (Figure 4.3),

$$\Delta p(x) = \frac{P(L_f - x)}{I_y} l \qquad (4.2.3)$$

where x is the distance from the fixed end of the beam, L_f is the free length of the cantilever, and I_y is the moment of inertia of the membrane cross section.

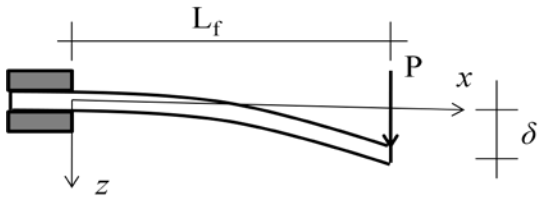

Figure 4.3: A cantilever beam with an end load

The tip deflection δ is:

$$\delta = \frac{PL_f^{\,3}}{3EI_y} \qquad (4.2.4)$$

where E is Young's modulus of the bulk material. Combining equations (4.2.3) and (4.2.4), the pressure drop Δp between the two ends of the channel has the relationship with the deflection as

$$\frac{\Delta p(x)}{l} = \frac{3E(L_f - x)}{L_f^{\,3}} \delta \qquad (4.2.5)$$

which indicates that in the model the channel length does not affect the prediction of the streaming current. It does however indicate that E, the Young's modulus of the material, has a linear relationship with the streaming current.

4.2.3 **Streaming Current in an IPT Bender**

Combining equations (4.1.5) and (4.2.5), the streaming current in a single channel is given as

$$I_s(x) = \frac{2wh^3\rho_e E(L_f - x)}{\eta {L_f}^3}\delta \qquad (4.2.6)$$

where x varies with channel position along the length of the IPT (Figure 4.3). Consider that the signal expected for the array of nanochannels existing in an IPT is additive. The total current in an IPT equals the sum of the current in every single channel in the IPT. The total current can be calculated by integrating equation (4.2.6) over the length of the IPT and then imposing the estimated linear density of channels. Mathematically this is equivalent to multiplying the maximum streaming current in a single channel by half of the total channel number *N*. Equation (4.2.6) reaches its maximum at the fixed end of the IPT cantilever beam where $x = 0$ as

$$I_{s\max} = \frac{2wh^3\rho_e E}{\eta {L_f}^2}\delta \qquad (4.2.7)$$

The number of nanochannels *N* can be calculated through the dimensions of the IPT and the channel, the thickness of the electrode, and the volume fraction of the diluent (Figure 4.2). For an IPT with electrolyte volume fraction of $v_{f,l}$, the total number of nanochannels is

$$N = \frac{V_{Nafion} v_{f,l}}{V_{channel}} = \frac{v_{f,l} W L_f l}{2hwl} = \frac{v_{f,l} W L_f}{2hw} \qquad (4.2.8)$$

where W is the width of the IPT cantilever, $v_{f,l}$ is the volume fraction of the diluent, and l is the thickness of the electrodes. Hence, the total streaming current in an IPT is

$$I_t = \frac{N}{2} I_{s\max} = \frac{v_{f.l} W h^2 \rho_e E}{2\eta L_f} \delta \qquad (4.2.9)$$

4.2.4 **Preliminary Predictions**

A 5 mm x 15 mm IPT with 38.2% volume fraction of water is considered to estimate the total number of channels within the volume. By equation (4.2.9), which indicates a linear relationship between the tip deflection and the current generated in the IPT, the projected sensing trend as a function of tip deflection is illustrated in Figure 4.4.

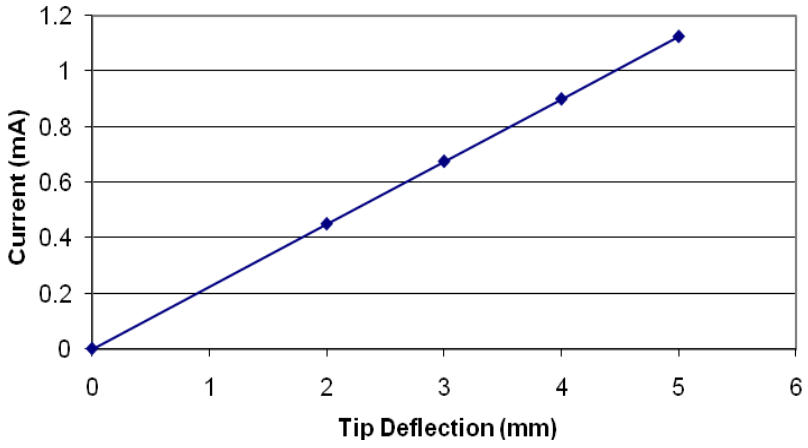

Figure 4.4: Preliminary predictions of IPT currents at various tip deflections

The purpose of the predictions of Equation (4.2.9) and subsequently Figure 4.4 is to establish that the generalized approach yields physically reasonable predictions. The predicted current is higher than the experimental results. For instance, for the 2.0 mm deflection case the

expected IPT current is ~0.01 mA for an 8.5 mm x 10 mm sample [11], while this prediction is ~0.50 mA. However, observation of appropriate trends is significant. The general prediction trend is correct, namely, as deflection is increased the predicted IPT sensor current also increases [91].

4.2.5 **Channel Geometry**

While the predictions of equation (4.2.9) and Figure 4.4 are helpful in establishing a preliminary proof-of-principle on the proposed method (namely, that the predicted order of magnitude is reasonable), for the current state of development, normalization will be more instructive and appropriate in the assessment of IPT predicted trends. Therefore, for IPT cantilevers with the same electrode characteristics (counterion, electrode thickness, diluent type and uptake), the streaming current of equation (4.2.9) can be normalized with respect to $\frac{\nu_{f,l} W h^2 \rho_e E}{2\eta}$. The normalized streaming current is expressed as

$$I_t \Big/ \frac{\nu_{f,l} W h^2 \rho_e E}{2\eta} = \frac{\delta}{L_f}, \qquad (4.2.10)$$

While the streaming potential hypothesis is not dependent on the exact geometry of a transport pathway, the parallel channel morphology is convenient for illustration. To illustreate this, it is prudent to adapt the streaming current predictions from the rectangular channel model (Figure 4.5b), to a round cross sectional channel model. Further this adaption will become important for model adaptation to the significantly different cluster morphology proposed by Hsu and Gierke (Section 4.5). Moreover, a round cross-section is more akin to the morphology model in Nafion proposed by Schmidt-Rohr and Chen [29], in which the dimensions of the channels are

distributed in a range (1.8~3.5 nm diameter; Figure 4.5a). For simplicity the nanochannels in this illustration are assumed to be identical parallel circular cylindrical channels with radius a uniformly distributed throughout the IPT (Figure 4.5c). Then the flow velocity in the channel becomes

$$v(r) = \frac{\Delta p}{4\eta l}(a^2 - r^2) \qquad (4.2.11)$$

where r is the distance from the center of the cylindrical channel.

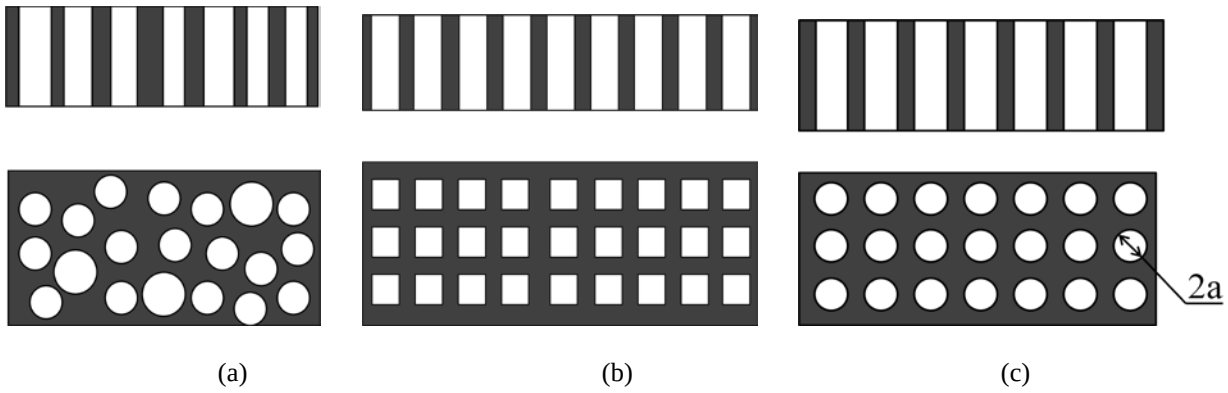

Figure 4.5: (a) Parallel circular cylindrical nanochannel morphology proposed by Schimdt-Rohr and Chen, (b) a model of identical and uniformly distributed parallel channels with rectangular cross-section, and (c) the adapted model of parallel channels with round cross-section

For cylindrical channels, the streaming current is defined by

$$I_s = 2\pi \int_0^a \rho(r) v(r) r dr \qquad (4.2.12)$$

Combining equations (4.2.5), (4.3.1), and (4.3.2), the streaming current in a single channel is given as

$$I_s(x) = \frac{3\pi\rho_e a^4 E(L_f - x)}{8\eta {L_f}^3}\delta \qquad (4.2.13)$$

With a maximum value of

$$I_{s\max} = \frac{3\pi\rho_e a^4 E}{8\eta {L_f}^2}\delta \qquad (4.2.14)$$

For an IPT with diluent volume fraction of $v_{f,l}$, the number of the cylindrical nanochannels is

$$N = \frac{V_{Nafion} v_{f,l}}{V_{channel}} = \frac{v_{f,l} W L_f l}{\pi \cdot a^2 l} = \frac{v_{f,l} W L_f}{\pi \cdot a^2} \qquad (4.2.15)$$

Thus, per the same arguments presented above in the integration over the transducer, the total streaming current of an IPT equals

$$I_t = \frac{N}{2} I_{s\max} = \frac{3}{16}\frac{v_{f,l} W a^2 \rho_e E}{\eta L_f}\delta \qquad (4.2.16)$$

Comparing equation (4.2.16) with equation (4.2.9) for rectangular channel model in preliminary studies, the streaming current is observed to be a function of a single characteristic cross-sectional dimension. Thus, while the predicted magnitude of streaming current may vary with assumed morphology, its existence is insensitive to the assumed morphology. Further, per the same method presented previously, for IPT cantilevers with the same electrode characteristics (counterion, electrode thickness, diluent type and uptake), the streaming current of equation (4.2.16) can be normalized with respect to $\frac{3}{16}\frac{v_{f,l} W a^2 \rho_e E}{\eta}$. The normalized streaming current is expressed as

$$I_t \Big/ \left(\frac{3}{16}\frac{v_{f,l} W a^2 \rho_e E}{\eta}\right) = \frac{\delta}{L_f}, \qquad (4.2.17)$$

The normalized equations (4.2.10) and (4.2.17) have exactly the same expression, which means the predictions will not vary between these two channel geometries. This is supportive of the conclusion that the streaming current is insensitive to the channel geometry for the parallel channel model. Figure 4.6 shows the relationship between the normalized streaming currents and the tip deflections for IPT cantilevers with free lengths of 15 mm and 20 mm. As expected the shorter IPT is predicted to display a higher streaming current when subject to the same tip displacement, as this will incur larger internal stresses/pressure, and therefore larger flow velocities in the shorter IPT. While for IPTs with same free length, the normalized streaming current for rectangular channel model and circular cylindrical channel model are identical. Thus in the presence of the proposed normalization appropriate predictions are retained.

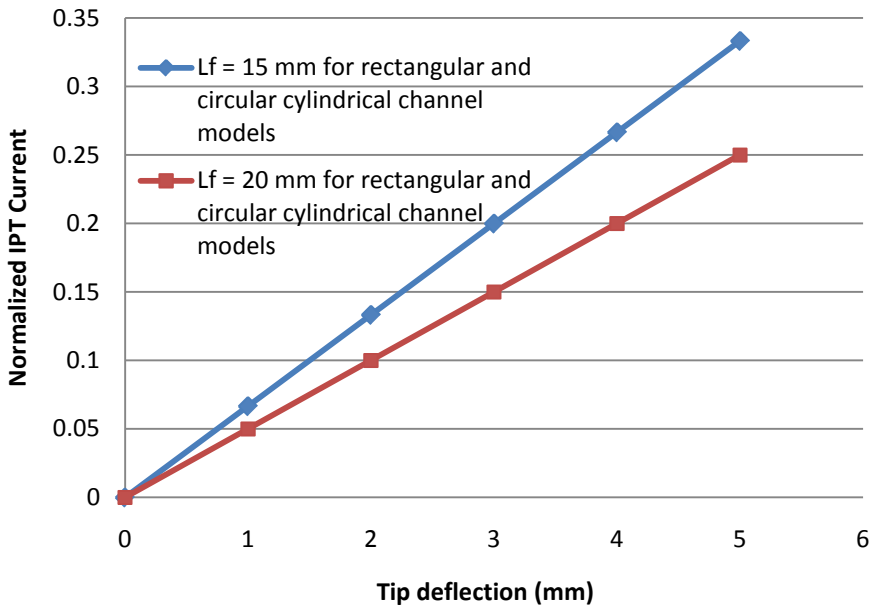

Figure 4.6: Normalized streaming current vs. tip deflection for IPT cantilevers with free lengths of 15 mm and 20 mm. for both rectangular and circular cylindrical channel models

4.3 EFFECT OF ELECTRODE ARCHITECTURE

As discussed in the literature review, the direct assembly process (DAP) for electrode application allows the controllable creation of a wide array of electrode architectures [48]. The approach enables blending of varied volume fractions and types of ionomer, diluent, and conducting powder. It has previously been demonstrated that the properties of IPTs vary with electrode architecture. In this section, the streaming potential method is employed to model IPT sensing responses with different electrode architectures. The resulting trends are compared with previous experimental data.

4.3.1 **Electrode Morphology**

Scanning electron microscopy (SEM) has been performed on select polymer samples by Akle to explore the electrode morphology effects of the DAP for varied electrode thickness and metal to polymer ratio in the electrode [48]. Shown in Figure 4.7 are two SEM images of DAP built transducers with different electrode thickness [48]. Figure 4.8 shows the SEM images of transducers with different metal to ionomer concentrations [48]. The transducers are saturated with 1-ethyl-3-methylimidazolium trofluoromethanesulfonate (EmI-Tf) ionic liquid.

The SEM images clearly show that the electrode morphology of metal particles dispersed within the ionomer is similar to a porous medium. A porous medium is a matrix permeated by an interconnected network of voids (pores). In the streaming current model presented here, it is assumed that the electrode is composed of the metal particles and the voids between the particles. A void is the space between the particles that are touching. For porous media, a void could be air, water, etc. In the cases for IPTs built by DAP, the void is a mixture of the ionomer and the

diluent. The void volume fraction of the electrode can be considered as the porosity of the electrode. The electrode particles contact each other and coagulate through DAP. The “porosity” and surface area of the electrode are related to the extent of this coagulation.

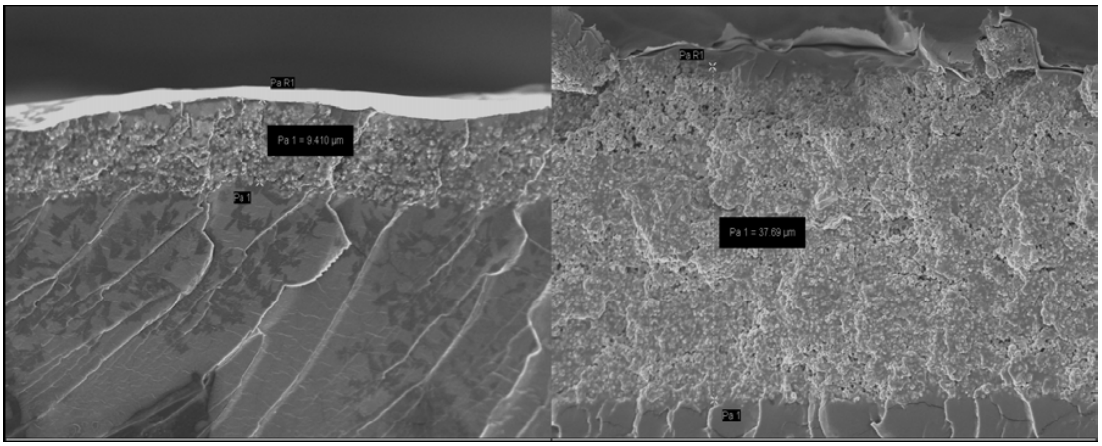

Figure 4.7： Scanning electron microscopy (SEM) showing (a) the top crosssection of a Nafion 117 ionomer painted with a 9.5 µm RuO_2 / Nafion electrode. (b) shows the top cross-section of a Nafion 117 ionomer painted with a 38 µm RuO_2 / Nafion electrode [48].

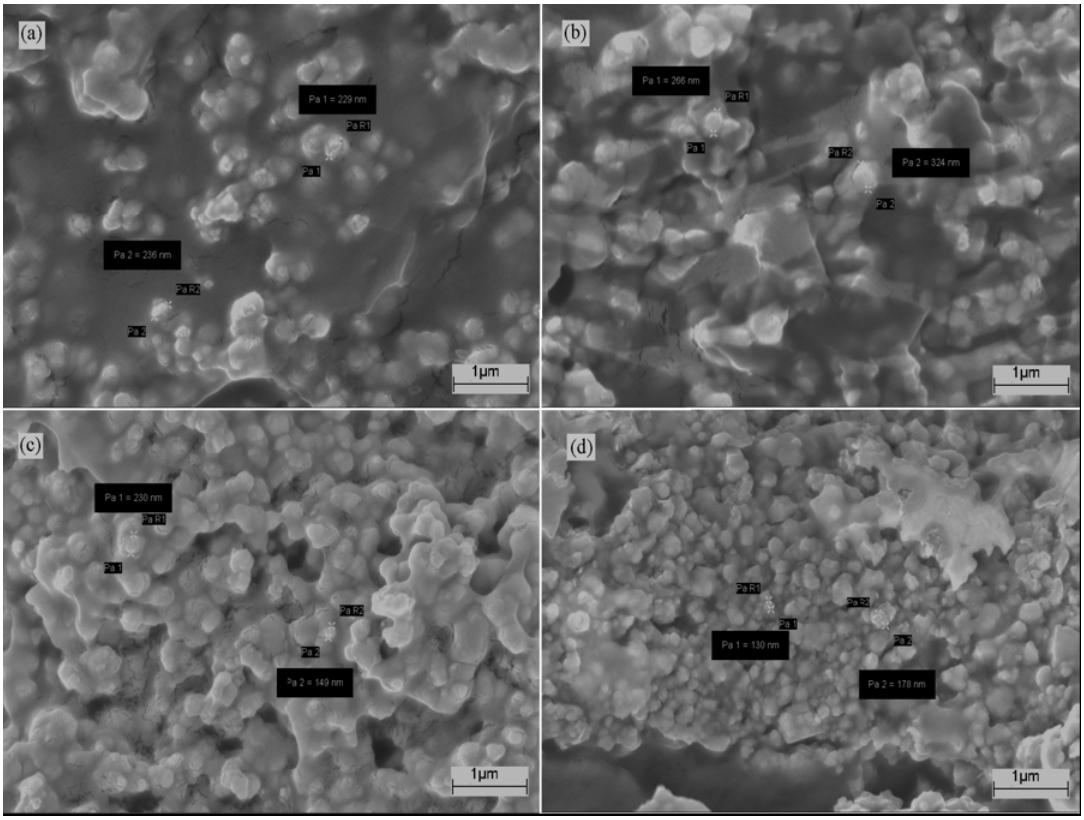

Figure 4.8: Scanning electron microscopy (SEM) SEM images of the high surface area RuO_2 electrode with (a) 22, (b) 30, (c) 36, and (d) 66 vol % metal [48].

4.3.2 **Darcy's Law**

Darcy's law is a phenomenologically derived constitutive equation that describes the flow of a fluid through a porous medium. Darcy's law is a simple proportional relationship between the instantaneous discharge rate through a porous medium, the viscosity of the fluid and the pressure drop over a given distance. By Darcy's law, the pore velocity v would be the velocity a conservative tracer would experience if carried by the fluid through the formation

$$v = \frac{q}{\phi} \qquad (4.3.1)$$

where ϕ is the porosity of the medium defined as a fraction of the volume of voids over the total volume

$$\phi = \frac{V_{void}}{V_{total}} \tag{4.3.2}$$

The flux q, discharge per unit area, with units of length per time, m/s, is

$$q = \frac{-\kappa}{\eta}\nabla p \tag{4.3.3}$$

where η is the viscosity of the fluid, ∇p is the pressure gradient vector, and κ is the permeability of the medium

$$\kappa = C \cdot a^2 \tag{4.3.4}$$

where C is a dimensionless constant that is related to the configuration of the flow-paths, and a is the pore radius. Combining equations (4.3.1)-(4.3.4), the pore velocity becomes

$$v = \frac{-C \cdot a^2}{\eta\phi}\nabla p \tag{4.3.5}$$

Assuming the electrode area of an IPT can be considered as a porous medium, Darcy's law can be used to describe the streaming potential phenomenon in the electrode. The porosity ϕ here is the volume of the polymer times the volume fraction of the diluent in the polymer. Combine equations (4.3.5), and (4.2.12), the streaming potential profile simplifies to

$$I_s = C\frac{\pi \cdot a^4 \rho_e}{\eta\phi}\frac{\Delta p}{l} \tag{4.3.6}$$

The cantilever beam analysis arguments in the elimination of $\frac{\Delta p}{l}$ and subsequent integration over the transducer as presented in Sections 4.2.2 and 4.2.3 are again employed. Introducing the

volume fraction of metal particulates in the electrode $v_{f,p}$ as a factor for electrode-electrolyte communication, by equations (4.2.5), (4.2.15), and (4.3.6) the total streaming current of an IPT in the porous interpenetrating electrode region becomes

$$I_t = \frac{Nv_{f,p}}{2} I_{s\max} = \frac{3C}{2} \frac{v_{f,l} v_{f,p} W a^2 \rho_e E}{\phi \eta L_f} \delta \qquad (4.3.7)$$

As illustrated in Figure 2.5 (copied below for convenience), varying electrode thickness and particulate volume fraction via the DAP has a significant effect on IPT sensing response. Inspection of equation (4.3.7) lends insight into the observation of increased sensitivity with thickness. The particulate is stiffer than the ionomer. As layers of particulate are added, the overall IPT stiffness E will increase, while all other parameters remain fixed. Moreover, it is intuitive that sensitivity should increase with increased electrode communication surface area. However, the existence of some optimum in the case of varied particulate volume fraction requires additional consideration.

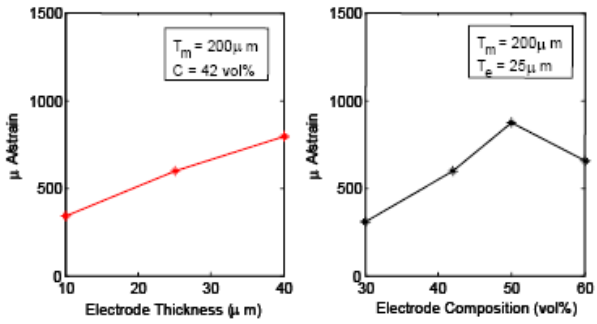

Figure 2.5: The normalized sensing response per unit strain of a RuO2 based IPT as a function of (a) electrode thickness, and (b) electrode metal composition (volume percent) [12].

4.3.3 **IPTs with Different Electrode Particulate Volume Fraction**

When the electrode particulate volume fraction varies the elastic energy of the material system also varies, and so the channel size varies accordingly; thus there exists some tradeoff between the availability of conductive particulate and availability of streaming electrolyte. One approach to address the changing channel size is via Eshelby micromechanics. In general it is expected that, for otherwise consistent properties, the channel size will decrease with increasing particulate volume fraction. A rigorous solution of the variation could adapt the detailed mircomechanics approach by Li and Nemat-Nasser [26] to the case of elongated ellipsoids. For the purpose of the current work the ability to demonstrate the trend is deemed sufficient. Predicted evolution of spherical inclusions with particulate volume fraction has previously been employed to estimate channel size evolution [50]. Here the ratio (β) of evolution of spherical cluster size per the expression developed by Li and Nemat-Nasser [26] is imposed on channel cross-sectional area evolution [50] from the baseline suggested by Schmidt-Rohr and Chen [29]. Thus, the radius a of equation (4.3.7) is replaced by βa,

$$I_t = \frac{3C}{2}\frac{v_{f,l}v_{f,p}W\beta^2 a^2 \rho_e E}{\phi\eta L_f}\delta = B\frac{v_{f,p}\beta^2}{\phi}, \qquad (4.3.8)$$

All the parameters in the expression expected to display comparatively small or no variation with the evolution of particulate volume fraction are lumped into a single constant *B*. For instance, each case considered will be subject to the same tip displacement δ. Dividing by the constant *B* enables inspection of the influence of the remaining terms, collectively described as the streaming current factor in Table 11 and plotted in Figure 4.9.

Table 11. Predicted variation in channel size with electrode particulate [50].

RuO_2 volume fraction ($v_{f,p}$)	0	0.3	0.4	0.5	0.6
Radius Ratio ($\beta = a_c / a_{c,0\%}$)	1	0.98	0.92	0.85	0.75
Porosity (ϕ)	1	0.7	0.6	0.5	0.4
Streaming current factor ($\frac{v_{f,p}\beta^2}{\phi}$)	0	0.41	0.56	0.72	0.68

IPTs with RuO_2 volume fraction from 0 to 60% are calculated. To appreciate the population of Table 11 consider the cases of zero and 30 vol% ruthenium dioxide. When there is no RuO_2 present, the channel size corresponds to that expected in pure, hydrated ionomer. Thus the radius of the channel is unaltered ($\beta = 1$) while porosity factor is 100% ($\phi = 1$). The net factor is therefore $\frac{0 \times 1^2}{1} = 0$; while flow is unrestricted there is no communication with the electrode. As RuO_2 volume fraction increases to 30 vol%, the changed cluster energy predicts a modest decrease in channel size ($\beta = 0.98$) and somewhat more restriction in flow due to porosity effects ($\phi = 0.7$), but this flow is now in communication with the electrode, and thus the net factor is non zero. As further RuO_2 is introduced, flow is further restricted while electrode surface area continues to increase. At some point (beyond 50 vol% RuO_2) flow becomes so restricted that diminishing returns are observed.

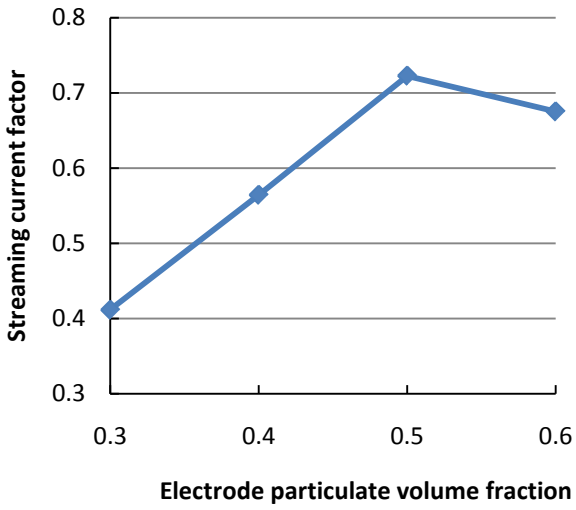

Figure 4.9: Normalized **s**treaming current as RuO_2 volume fraction varies.

Comparing with experiment (Figure 2.5) a sensitivity peak is correctly predicted at 50 vol%. Weiland and Akle [50] have predicted a similar peak, but failure to include porosity in their analysis resulted in a comparatively flat projection. The approach presented here including porosity more accurately predicts the relative magnitude of the experimentally observed peak. It is generally agreed that when the volume fraction of metal particles increases, the porosity ϕ initially decreases but will increase again when the concentration precipitates particle aggregation. In this study the electrode particulates are assumed to be identical spheres. Therefore, the evolution of porosity remains linear because the most packed arrangement of identical spheres has porosity of 0.26, while in this study that transitional value is never reached.

4.3.4 **Effective Surface Area of the Electrode Particulates**

The preceding section explored the effect of varying the volume fraction of a single type of electrode particulate. Next consider that it has also been experimentally observed that the type of

particulate introduced to the IPT electrode via the DAP can have significant effect. To explore this, consider first that among the channels in the ionic polymer only those that contact with the electrode particles are effective per the streaming potential model, *i.e.*, the streaming current is proportional to the metal-ionomer interfacial area. Thus the effective surface area of the electrode particulates is proportional to the number of effective channels that interact with the electrode particulates. The effective number of channels N_e can be estimated as:

$$N_e = \frac{A_e}{\pi \cdot a^2} \tag{4.3.9}$$

where A_e is the effective area of the metal-polymer interfacial area. Now consider the case of an electrode region composed of blends of ruthenium dioxide and gold, the volumetric surface area of RuO_2 and Au are 400 and 10 m, respectively. The effective metal-polymer interfacial area A_e can be estimated as,

$$A_e = V_{electrode}(400 \times V_{RuO_2}\% + 10 \times V_{Au}\%) \tag{4.3.10}$$

where the surface area of these constituents is proportionally addressed. Imposing this expression for the case where the total metal volume fraction is held constant at 40 vol%, illustrates the predicted linearly increasing trend with the content of RuO_2 for sensing observed. The relative number of effective channels for different content of metals is shown in Table 12. In the absence of experimental data for sensing with varied composition a comparison with actuation data is considered (Figure 4.11) [48]. The experimental data displays a plateau in the plot of strain output of IPTs at 50 vol% and 75 vol% RuO_2. As noted above, the porosity in this dissertation does not consider particle aggregation for the volume fractions of pure RuO_2. The experimental plateau could be because of the onset of particle aggregation at 50 vol% in the presence of a

RuO_2 and Au blend, which would limit the effective surface area of the electrode. Moreover, this assessment does not consider the different electrical conductivities, where the superior conductivity of gold as compared to its volume fraction may also contribute to the onset of dimimishing returns at some critical volume fraction. Further, the use of actuation data in this instance may also represent an important source of error. However, in general the IPT performance shows an increasing trend when the content of RuO_2 increases, which is consistent with the predicted increasing active response for increasing RuO_2 content.

Table 12. Percentage of effective channels.

RuO_2 volume fraction	1	0.75	0.5	0.25
Au volume fraction	0	0.25	0.5	0.75
Relative number of effective channels (n:n %)	1	0.76	0.51	0.27

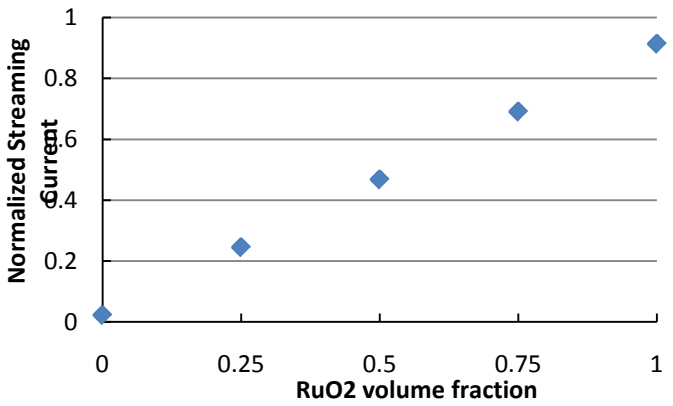

Figure 4.10: Normalized modeling sensing trends for IPTs with variation in the metal content of RuO_2 and Au for consistent total volume of metal

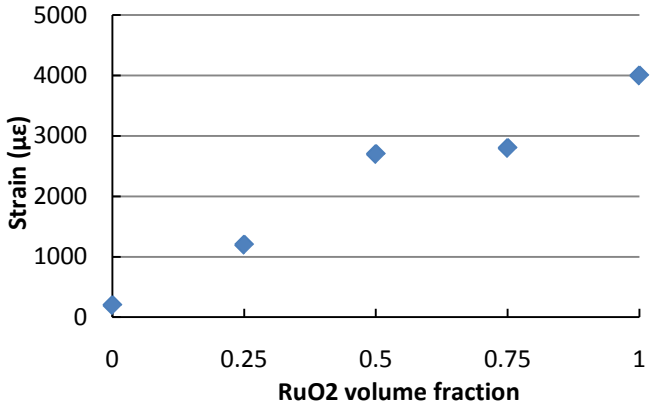

Figure 4.11: Strain output of IPTs for samples produced by variation in the metal content with consistent volume to the application of square wave potentials of ±2 V [48].

4.4 EFFECT OF DILUENT VARIATION

In addition to the IPT sensing response effects when the electrode architecture is varied, it has been experimentally observed that variations in the ionomer state also affect response. For instance, variation in diluent uptake and variation in diluent type have both been shown to affect response. This section as well as Section 4.5 will explore the ability of the streaming current model to predict experimentally observed variations in sensing response as the ionomer state and morphology assumptions are varied.

4.4.1 Ionic Liquid versus Water as IPT Diluent

Traditionally, water has been used as the diluent for IPTs. Water-swollen IPTs have to be operated in an aqueous environment to maintain their stability, which has limited their applications. While some reports suggest that dehydration may have favorable effects on

sensitivity, these reports have not yet reached concensus. Recently ionic liquids have been used as the diluents in Nafion based IPTs for their excellent thermal and electrochemical stability and very low vapor pressure. Bennett et al. [12] have compared water to ionic liquids as the diluents by applying a 1.5 V (peak) sine wave on a platinum- and gold-plated Nafion 117 swollen with water and 1-ethyl-3-methylimidazolium trofluoromethanesulfonate (EMI-Tf) ionic liquid, respectively. When operated in open air, the strain generated by the water swollen IPT sample decreased nearly to zero after about 2000 cycles due to the dehydration of the material. By contrast, the same actuator swollen with EMI-Tf operated for over 250,000 cycles with only 25% decrease of generated strain. Although there is a decrease of the magnitude of the actuation response and a reduction in the speed of the response in IPTs swollen with ionic liquids, the improvement of the operation stability in open air could potentially increase their applications dramatically.

In this section the effect of water vs. ionic liquid EMI-Tf is considered for a case with Lithium counter ion, 35% electrode volume fraction, and diluent volume fraction of 32.8% for water and 48.2% [27] for ionic liquid EMI-Tf. Fromequation (4.3.7), the streaming current can be predicted by

$$I_t = \frac{3C}{2}\frac{v_{f,l}v_{f,p}Wa^2\rho_e E}{\phi\eta L_f}\delta \qquad (4.4.1)$$

To assess the variation in predicted response it is noted that the diluent volume fraction $v_{f,l}$, the viscosity η, and the channel size a vary between the two cases. The volume fraction variation is assessed directly (38.2% and 48.2% for water and ionic liquid, respectively). Similarly, the effect of variation in viscosity may be varied directly by the assumption that macroscopically measured properties appropriately capture the trend. While the channel size in water and ionic liquid forms

are only slightly different, because the parameter is raised to the power of 2 the difference is considered. This cluster radius of EMI-Tf swollen IPT is estimated via the micromechanics approach proposed by Li and Nemat-Nasser [26], which was introduced in Section 2.4 and was previously implemented in the Chapter 3 assessment of Selemion®. The total number of channels is lastly accommodated via equation (4.2.15) above. The total numbers of channels are different due to different diluent content and channel size. All the relevant parameters are shown in Table 13.

The predicted currents in water swollen Nafion is about 60 times that of EMI-Tf swollen Nafion as shown in Figure 4.12. Corresponding experiments have been conducted as shown in Figure 4.13 [12], which shows that the sensitivity of water swollen Nafion is several times higher than that of the ionic liquid swollen Nafion. The difference between these two diluents is less than the predictions. However, the fact that the sensitivity of water swollen IPT is higher is consistent with the predicted trends.

Table 13. Relevant parameters for water and EMI-Tf form IPT samples

Electrolyte	Water (Li^+)	EMI-Tf
Viscosity (cP)	1	45
Volume fraction (%)	38.2	48.2
Surface energy* (dyn/cm)	72.9	52
Cluster radius (Å)	$22.5^{[26]}$	17.8
Charge density (C/m^3)	$2.09x10^7$	$6.55x10^7$

Number of channels	2.90×10^{12}	7.26×10^{12}

*(Required for micromechanics estimate of radius)

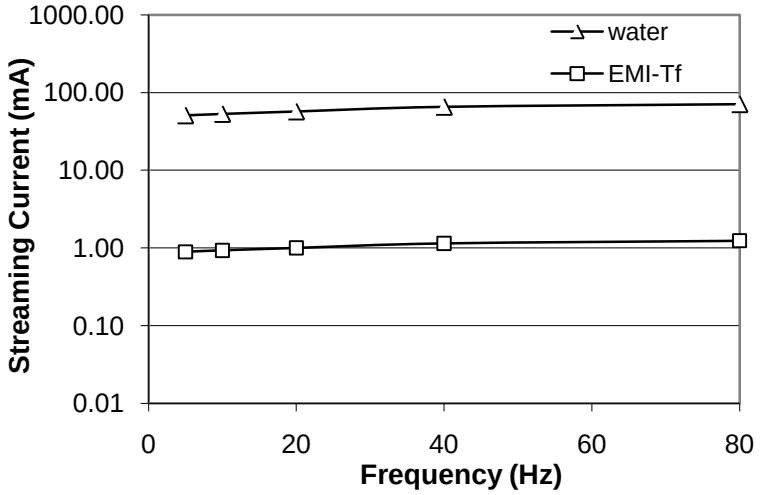

Figure 4.12: Predictions of streaming current trends in IPTs in water and ionic liquid form

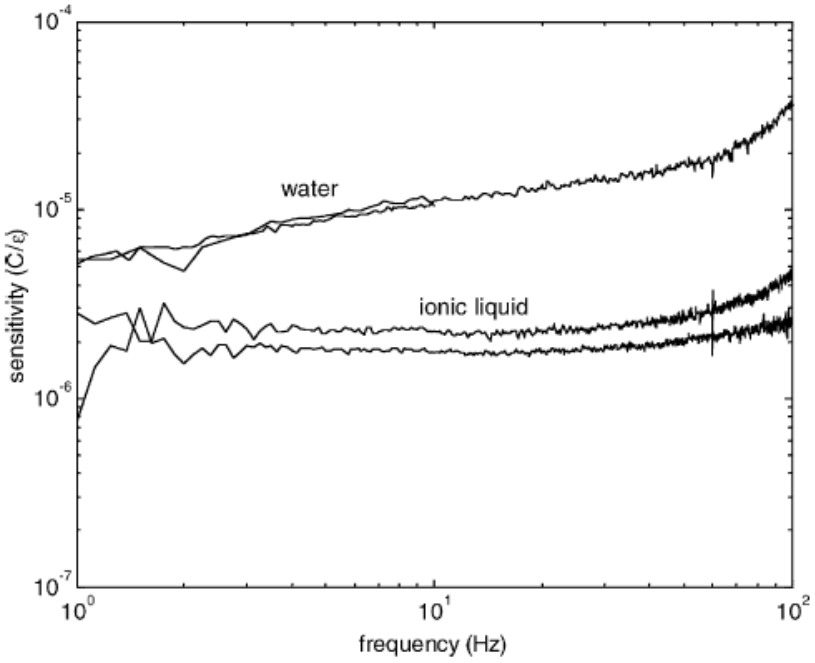

Figure 4.13: Charge-to-strain sensing response of samples in water and ionic liquid (EMI-Tf) form [12]

The predictions are not normalized because several parameters vary for different diluents, including the diluent volume fraction, the channel size, and the viscosity of the diluent, and the Young's modulus of the material varies as well when the frequency varies. The magnitude of the predictions is not comparable with the experimental data because the experiments measured the charge sensing sensitivity in C/ε while the predictions are currents in mA. However, the predicted trends that the water swollen Nafion has higher sensitivity than the EMI-Tf swollen Nafion and the sensitivity increases when the frequency increases are consistent with the experiments. This result is encouraging, however, careful inspection of the governing equation illustrates that this prediction is dominated by the variation in viscosity between the two cases. Consider for instance restating the comparison as a ratio of the two predicted responses, by equation (4.4.1), the ratio is:

$$\frac{I_w}{I_{IL}} = \frac{v_{f,w} a_w^{\,2} \eta_{IL}}{v_{f,IL} a_{IL}^{\,2} \eta_w} \qquad (4.4.2)$$

because the IPT dimensions (W and L_f) and electrode architectures ($v_{f,p}$ and ϕ) are the same, and there is no significant change in Young's modulus and charge density. It is observed that the impact of the channel radius has a factor of 2. This would be significant for a significant variation in radius. However, as compared to the 45:1 ratio of viscosity, this effect becomes small in the current case. It is prudent to next consider a case in which significant variation has been experimentally observed but for the same diluent, to isolate this effect.

4.4.2 **Sodium versus Lithium Cases for Water as IPT Diluent**

It has previously been observed that a fully hydrated (water as diluent), Lithium exchanged IPT displays 5 to 10 times the sensitivity of the fully hydrated Sodium exchanged case. Employing the same normalization approach of the previous section, where Table 13 provides pertinent experimentally determined parameters for assessment results in the simplified expression

$$\frac{I_{Li}}{I_{Na}} = \frac{v_{f,Li} a_{Li}^{\,2} \eta_{Na}}{v_{f,Na} a_{Na}^{\,2} \eta_{Li}} = \frac{v_{f,Li} a_{Li}^{\,2}}{v_{f,Na} a_{Na}^{\,2}} \qquad (4.4.3)$$

because there is no significant variation in viscosity. Imposing the parameters of Li form and Na form fully hydrated Nafion 1200 EW in [26] (Table 14) results in a prediction of approximate 1.5x sensitivity in the Lithium case. While it is encouraging the ratio predicts higher sensitivity in the Lithium case, even in a normalized form the prediction is substantially lower than experiment. Further consideration of this prediction requires assessment of the same scenarios per a different morphology; that proposed by Hsu and Gierke is imposed.

Table 14. Parameters for Nafion 1200 EW in Li and Na forms

Cation	Li^+	Na^+
Volume fraction of water (%)	38.2	30.7
Cluster radius (nm)	2.25	2.10

Table 15. Predictions per Schmidt-Rohr and Chen morphology comparing with reported experimental data

	Predicted	Experiment
$I_w : I_{IL}$	x60	~x10
$I_{Li} : I_{Na}$	x1.5	x5 to 10

4.5 EFFECT OF IONOMER MORPHOLOGY

The development of the streaming potential model to this point has put emphasis on the morphology proposed by Schmidt-Rohr and Chen [29]. This has been largely a matter of convenience: it is relatively straight forward to mathematically impose the streaming potential phenomenon in this proposed morphology. But as emphasized in Chapter 2, the actual morphology of Nafion, and ionomers in general, remains an open topic. However, the morphology of Hsu and Gierke [23] has been effectively employed and developed for over 30 years. Thus, despite the fact that it too is almost necessarily removed from reality, the history of developmental adaptation may bode well for its application.

Recall that the proposed morphology distributes spherical hydrophilic clusters of electrolyte amid a matrix of hydrophobic backbone. While application of the proposed morphology puts emphasis on the expected cluster size, it is understood that selective ionic conduction occurs in the channels between the clusters (Figure 2.1 copied below for convenience).

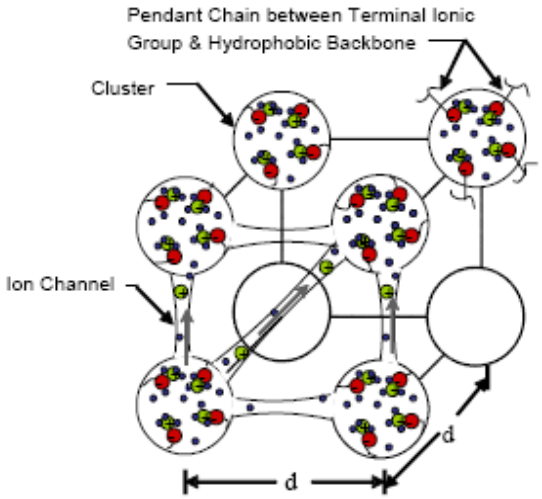

Figure 2.1: Selective Ionic Conduction per Hsu and Gierke [23].

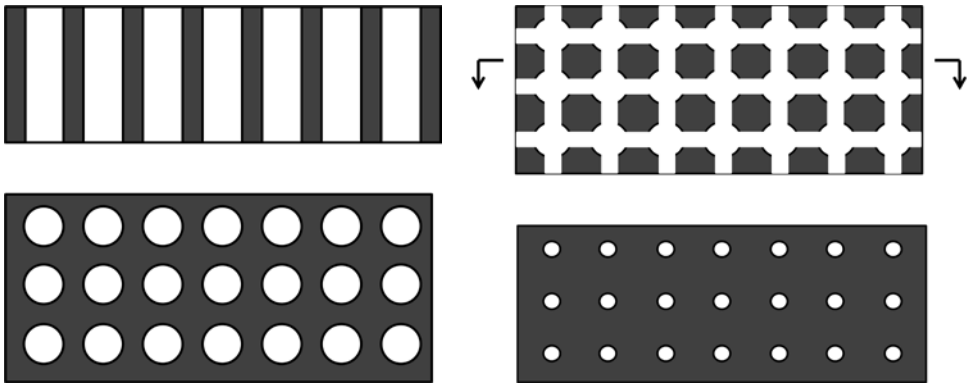

Figure 4.14: Sectional view of the channels in the models of (a) Schimdt-Rohr and Chen parallel channel morphology and (b) Hsu and Gierke cluster morphology

In order to assess the streaming current hypothesis for this cluster morphology, these conduction channels must take on some meaningful dimension. Here, it will be assumed that the volume of these channels can be approximated as right circular cylinders that typically retain some fixed proportion with respect to the volume of the clusters.

$$\pi \cdot a_{ch}{}^{2} \cdot l_{ch} = c \cdot \frac{4}{3} \pi \cdot a_{cl}{}^{3} \qquad (4.5.1)$$

Thus an IPT with especially high uptake and cluster volume, would also be expected to display relative ease in communication among these clusters, while the inverse is expected for a relatively dehydrated sample. The total current in an IPT can be predicted by the streaming current in a single conduction channel multiplied by the number of the channels. Although there are conduction channels between every two adjacent clusters, only those parallel to the thickness dimension of the IPT function as conduction channels in bending mode. Moreover, the streaming currents in the conduction channels aligned in series are not additive. In other words, only the streaming currents in parallel channels are additive. The number of effective conduction channels can be estimated by

$$N = \frac{WL_f}{d^2} \qquad (4.5.2)$$

where d is the cluter center-to-center distance (Figure 4.15).

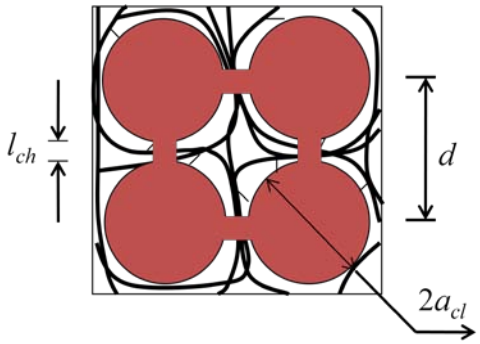

Figure 4.15: Demensions of clusters and conduction channels

If the size of these channels is further assumed to dominate the observed streaming potential (this is a conservative assumption), then per equation (4.2.14) for the maximum streaming current in a single channel can be predicted by

$$I_t = \frac{N}{2} I_{s\max} = \frac{N}{2} \frac{3\pi\rho_e {a_{ch}}^4 E}{8\eta {L_f}^2} \delta \tag{4.5.3}$$

Per equation (4.5.3) the ratio of performance between two Hsu and Gierke cluster morphology cases becomes

$$\frac{I_1}{I_2} = \frac{{N_1}^2 {a_{ch,1}}^4 \rho_{e,1} \eta_2}{{N_2}^2 {a_{ch,2}}^4 \rho_{e,2} \eta_1} \tag{4.5.4}$$

where

$${a_{ch}}^2 = \frac{4c}{3l_{ch}} {a_{cl}}^3 \tag{4.5.5}$$

$$l_{ch} = d - 2a_{cl} \tag{4.5.6}$$

$$d = \sqrt[3]{\frac{\frac{4}{3}\pi \cdot {a_{cl}}^3}{v_{f,l}}} = \sqrt[3]{\frac{4\pi}{3v_{f,l}}} a_{cl} \tag{4.5.7}$$

Substitution and simplication of equations (4.5.1)-(4.5.7) result in

$$\frac{I_1}{I_2} = \frac{a_{cl,1}{}^6 d_2{}^2 l_{ch,2}{}^2 \rho_{e,1} \eta_2}{a_{cl,2}{}^6 d_1{}^2 l_{ch,1}{}^2 \rho_{e,2} \eta_1} \quad (4.5.8)$$

Because the cluster center-to-center distance d and the channel length l_{ch} both have an linear relationship with the cluster size a_{cl}, $a_{cl}{}^4$ drops out by being divided by $d^2 l_{ch}{}^2$. Therefore, the impact of cluster size a_{cl} on streaming current also has a factor of 2 as that of channel size a does in Schimdt-Rohr and Chen morphology model. The impact of diluent volume fraction is included in the cluster center-to-center distance.

The expression may be similarly employed for the comparison between the water and ionic liquid cases where the charge density is assumed to be similar. In this case a ratio of 6.9 is predicted as compared to the experimentally observed ratio of about 5. For the comparison between the Lithium and Sodium exchanged cases, where charge density and viscosity continue to be similar, the predicted ratio is 4.7 as compared to the experimentally observed ratio of 5 to 10. Comparing with the parallel channel model with predicted ratio of about 60 and 1.5, these results are much closer to the experimental observation. The predictions and experimental data are summarized in Table 16.

Table 16. Predictions per Schmidt-Rohr and Chen parallel channel morphology and Hsu and Gierke cluster morphology comparing with reported experimental data

	Predicted by Schimdt-Rohr and Chen model	Predicted by Hsu and Gierke model	Experiment
$I_w : I_{IL}$	x60	x6.9	~x10
$I_{Li} : I_{Na}$	x1.5	x4.7	x5 to 10

In the cluster morphology model, the predicted ratio between different diluents or cations is much closer to the experiments. As presented before, the impact of cluster radius has a factor of 2 in both models, which means the cluster radius does not contribute to the ratio difference between the cases. From equations (4.4.2), (4.5.7), and (4.5.8) it can be observed that the contribution of the diluent volume fraction has changed from $v_{f,l}$ to $\left(\sqrt[3]{\frac{1}{v_{f,l}}}\right)^2$, which determines the cluster center-to-center distance as well as the total number of channels. The most significant observations here are (1) in the absence of critical assessment of each parameter assumption (for instance the assumption of similar charge densities among the cases) it is difficult to assert that either of these cases is fundamentally superior, and (2) while accuracy varies, and in the case of the Hsu and Gierke morphology accuracy is quite good, both the 'bounding' morphologies considered capture the appropriate trends.

4.6 TRANSIENT RESPONSE UNDER STEP BENDING

In this section the transient sensing response of an IPT cantilever due to a step displacement at the tip is considered from the perspective of the streaming potential model. From the preliminary study on the streaming potential mechanism in IPT sensing, it is observed that the streaming current is induced by the transport of the charged fluid at a certain velocity. The pressure difference between the two ends of the nanochannel is the key of the generation of the fluid velocity in bending.

When suddenly bending an IPT cantilever, the stress in the compressed layer generates a pressure difference along the thickness of the IPT in a very short period of time; hence a

streaming current in the IPT is generated. However, it is also understood that the fluid motion serves to dissipate the pressure, and thus the streaming current response is expected to be transient. To analyze the transient response of IPT current due to a sudden bending, the process is decomposed into a number of time increments. As time increases, the IPT tip displacement increases. It is assumed that after every time increment, when the charged fluid is transported from one side of the channel to the other side, the redistribution of the charged fluid neutralizes the stress difference in the material and acquires an equilibrium stress state in the material. Therefore, the magnitude of the current is determined by the IPT tip displacement change $\Delta\delta$ within a time increment, *i.e.*, the tip velocity. For identical IPTs subject to this analysis the streaming current as present by equation (4.3.7) may be normalized as,

$$I_t \Big/ \frac{3C}{2}\frac{v_{f,l}v_{f,p}Wa^2\rho_e E}{\phi\eta} = \frac{\delta}{L_f} \tag{4.6.1}$$

Farinholt and Leo [11] have performed experiments on the sensing response of IPTs under step tip displacement. Imposing the displacement input of their experiments (shown in Figure 4.16) on equation (4.6.1), and setting the normalized IPT current at maximum tip displacement to 1, the prediction of IPT current due to step tip displacement is plotted in Figure 4.17. The prediction is largely consistent with the experimental observation that the streaming current is proportional to the tip velocity, as should be expected from inspection of equation (4.6.1). One significant variation from experiment is the absence of a delay in predicted response; however the experimental report notes that it is not clear whether the apparent 7.5 ms delay is a manifestation of a physical mechanism in the IPT or associated with delays inherent in the measurement device.

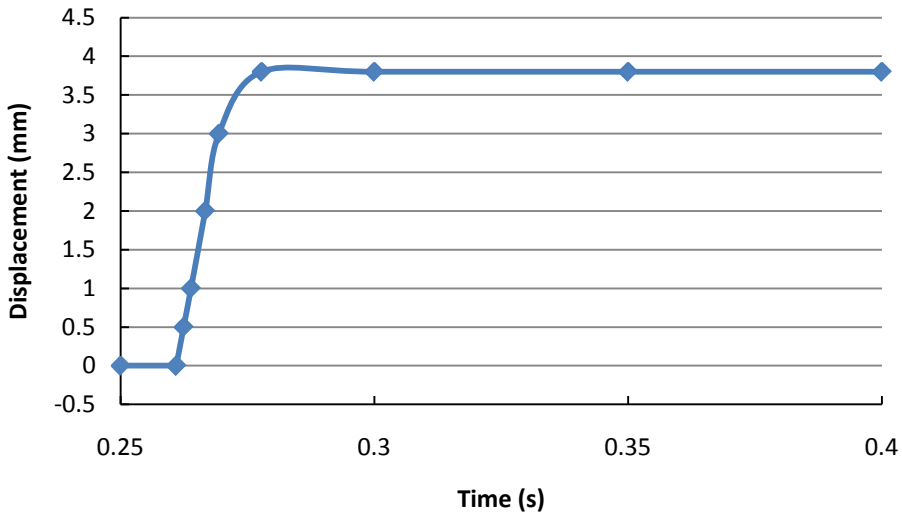

Figure 4.16: Step displacement input by Farinholt et al [11]

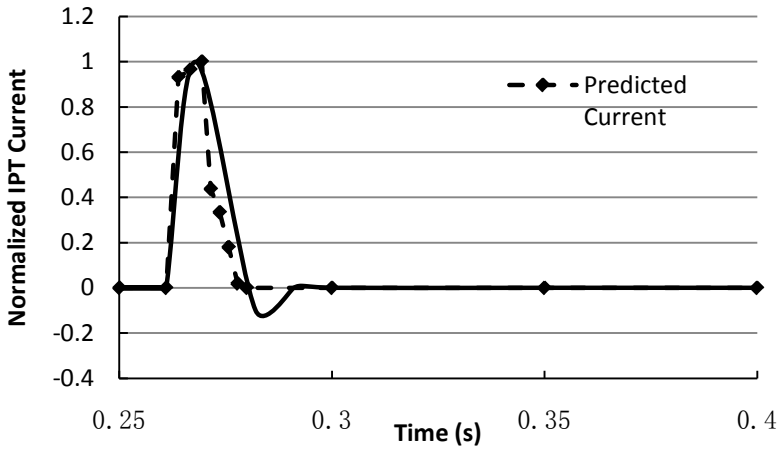

Figure 4.17: Normalized predictions of IPT current under step tip displacement plotted with measured current with normalization. Solid line is from experiment, dashed line is the predicted response. Discrete points correspond to points at which data is visually extracted from experimental stimulus plot of Figure 4.16.

Another notable difference is the absence of a current reversal of the predicted response as compared to the experimentally observed response. There are a number of possible explanations for the discrepancy. For instance the onset of oscillatory fluid motion in the presence of a viscously damped material system may display a transient current reversal.

Alternatively, as discussed in the previous chapter, the local stiffness (on the length scale of the channels) is among the parameters that will evolve with hydration [92], which will in turn have a proportional effect on local streaming current. In other words, hydration is increased/depleted on opposite sides of the transducer in bending; local stiffness evolution may transiently favor the streaming current on the depleting side.

This reasoning may inadvertently open questions regarding the evolution of the global stiffness. However, it can be easily shown that the stress relaxation observed in Nafion at a global length scale is small for the time scale of the step displacement. For instance, Liu et al. studied the tensile behavior of Nafion by measuring the Young's modulus of Nafion 117-H films at 3% strain with different initial strain rates [93]. The Young's modulus of Nafion 117-H at 3% strain with 0.7 min^{-1} initial strain rate are plotted in Figure 4.18, with a zoomed in perspective for a shorter time frame presented in Figure 4.19. Based on their results the global stiffness is expected to change from ~229 MPa to ~224 MPa over the 0.02 sec displacement. Thus evolution of global stiffness in the context of a step displacement is expected to be negligible; this however is not the case for dynamic loading.

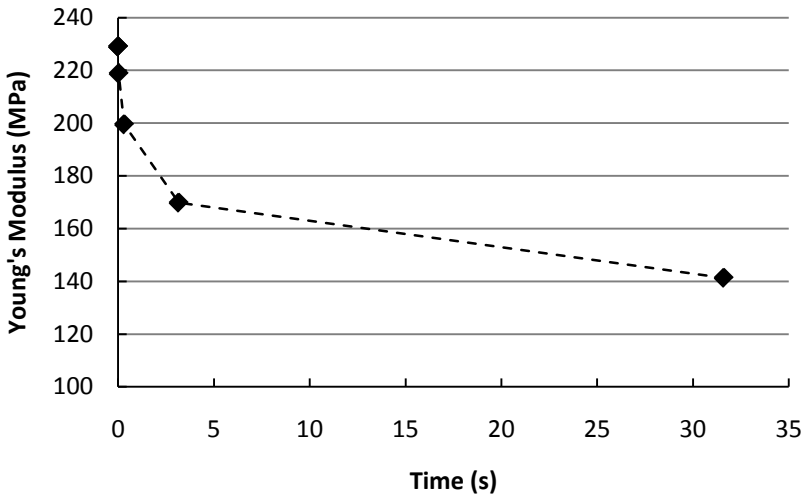

Figure 4.18: Young's modulus of N117-H at 3% strain with 0.7 min^{-1} initial strain rate [93].

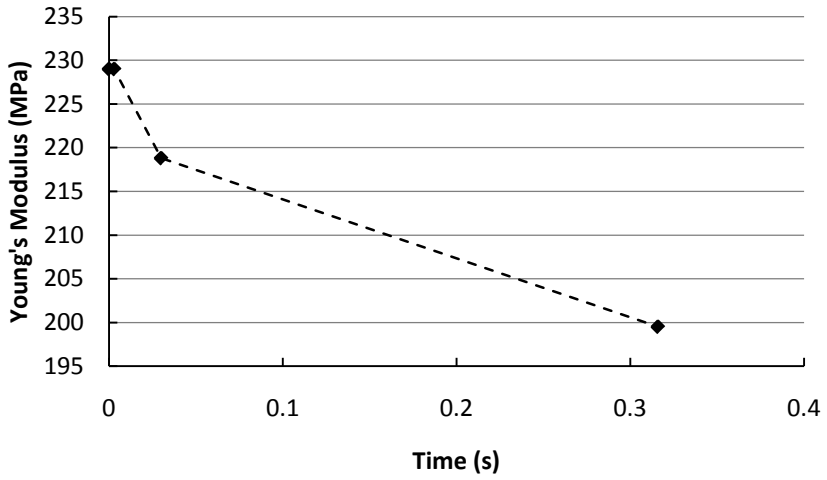

Figure 4.19: Relaxation effect during the process of step displacement

4.7 EFFECT OF STRAIN RATE

Besides its dependency on temperature and hydration due to phase inversion and cluster formation, Nafion as a polymer, exhibits strong time and strain rate effects. At different

frequencies, an IPT undergoes different strain rates. For viscoelastic materials with small strain, the Young's modulus is a function of strain rate. Therefore, Young's modulus becomes a function of frequency such that the IPT current is expected to have a linear relationship with the frequency. If global stiffness is no longer assumed as constant then the normalization proposed in equation (4.6.1) must now include evolution of Young's modulus on the right hand side of the expression,

$$I_t \Big/ \frac{3C}{2} \frac{v_{f,l} v_{f,p} W a^2 \rho_e}{\phi \eta} = \frac{\delta}{L_f} E_f , \tag{4.7.1}$$

where the subscript *f* has been introduced to denote the Young's modulus rate dependence. To retain normalization both sides of the equation can be divided by a reference value; Young's modulus at 100 Hz is imposed for this purpose.

$$I_t \Big/ \frac{3C}{2} \frac{v_{f,l} W v_{f,p} \beta^2 a^2 \rho_e E_{100Hz}}{\eta \phi} = \frac{\delta}{L_f} \frac{E_f}{E_{100Hz}}, \tag{4.7.2}$$

For an IPT vibrating with a steady maximum displacement, the expression becomes

$$I_t \propto \frac{E_f}{E_{100Hz}} \tag{4.7.3}$$

Franklin [94] has measured the evolution of effective Young's modulus from 5 Hz to 100 Hz as shown in Table 17. These data have been applied in equations (4.7.2) to generate the profile illustrated in Figure 4.20 where the normalized IPT current at 100 Hz is set to 1. It is understood that the load is increased to assure the same tip deflection as modulus increases. The current increases in the low frequency area but tends to be constant when the frequency goes up to 60 Hz.

Farinholt and Leo [11] have reported sensitivity as charge per strain (C/ε) as a function of frequency. As is typical in dynamic tests, the experimental results are noisy at low frequency, but rapidly tend toward a constant ($0.264\ \mu C/\varepsilon$) as frequency increases. While the presented predictions instead move toward a constant asymptotically, the tendency toward a constant sensitivity is captured. Moreover, while not a direct validation of the hypothesis that time varying Young's modulus contributes to the observed transient response to a step impulse, it is supportive of it.

Table 17. Young's modulus of Nafion at different strain rate

Frequency (Hz)	Young's Modulus (MPa)	Frequency (Hz)	Young's Modulus (MPa)
5	115	60	154
10	120	70	159
20	129	80	160
30	140	90	162
40	148	100	165
50	152		

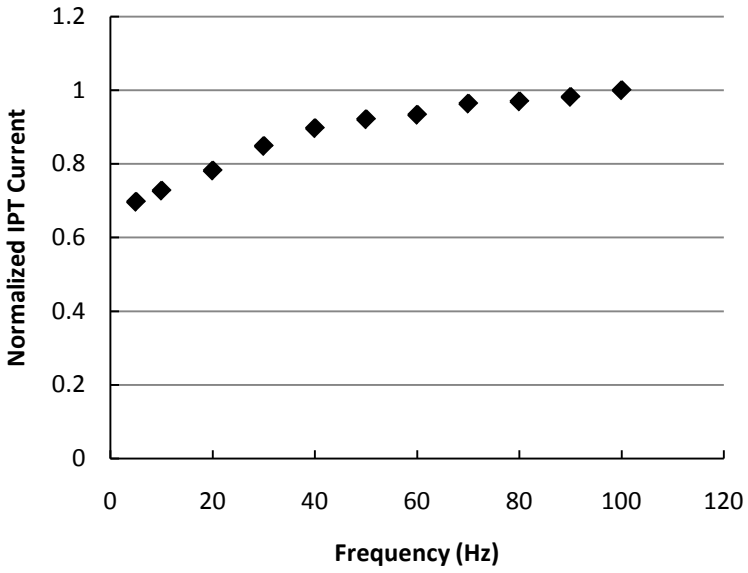

Figure 4.20: Normalized IPT current at different frequencies

4.8 DISCUSSION

The sensing responses of IPT benders are modeled from various perspectives based on the streaming potential mechanism. Even over the broad range of scenarios considered (manipulation of IPT state and loading), comparison of the normalized prediction trends with experimental data display good agreement. Achieving these validations indicates validity of the streaming potential method in bending mode. By the streaming potential method the sensing trends can be predicted for different IPT dimensions, electrode arthitectures, and ionomer states. These parameters, which have been experimentally demonstrated have different degrees of effects on the electromechanical properties of IPTs, can be vaired and compared arbitrarily to identify the desired IPT electromechanical performance. Therefore, this model can be used as an effective tool to assist IPT optimization.

To complete validation the hypothesis that the streaming potential is capable of modeling IPT sensing in all deformation modes must be considered (Figure 4.21). While not considered in detail, the legitimacy of this may be effectively addressed with qualitative arguments. The cases of tension and compression are relatively straight forward. For these consider first that the pressure gradient developed in bending corresponds to the hydrostatic component of loading. In both tension and compression the hydrostatic term exists, and therefore a motive force for fluid flow necessarily exists.

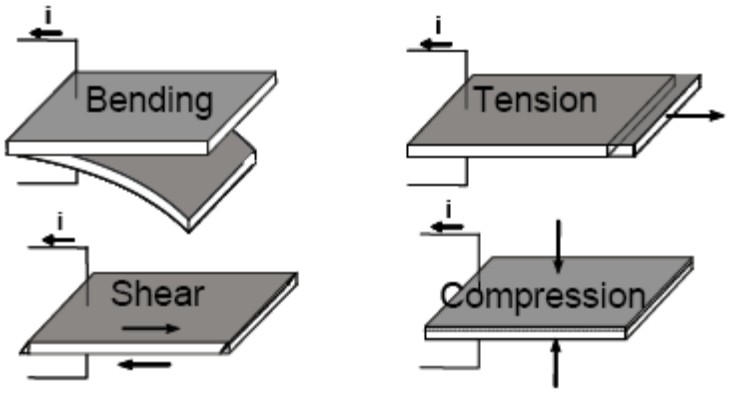

Figure 4.21: IPT macroscopic sensing modes [50]

For the case of pure shear loading however, no hydrostatic term exists, thus the motive force for fluid flow must be fundamentally different in this case. For this scenario, consider an IPT in shear mode, while one side of the IPT is fixed and the other side is driven by a shaker. The relative motion between the two sides of the IPT results in a shear deformation and a potential through the material thickness (Figure 4.22).

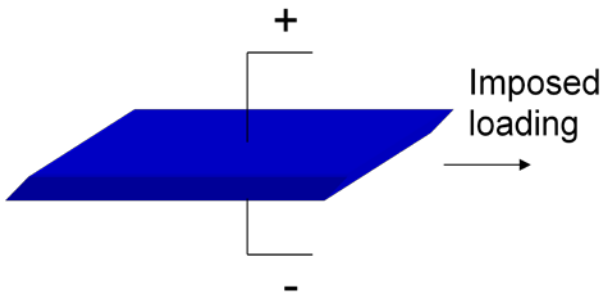

Figure 4.22: An IPT sensor under imposed shear loading

Consider each of the electrodes of an IPT as two parallel plates, the porous property of the electrode makes the flow in the IPT electrode viable. Therefore, a first order estimate of shear mode velocity of the electrolyte in the IPT electrodes can be modeled by the classic parallel-plate flow. The most fundamental premise of the streaming current hypothesis argues that whenever there is a net relative motion of the electrolyte with respect to the electrode, the streaming potential is developed. Therefore, the parallel-plate flow developed inside the electrodes is expected to be able to develop a streaming potential in the IPT.

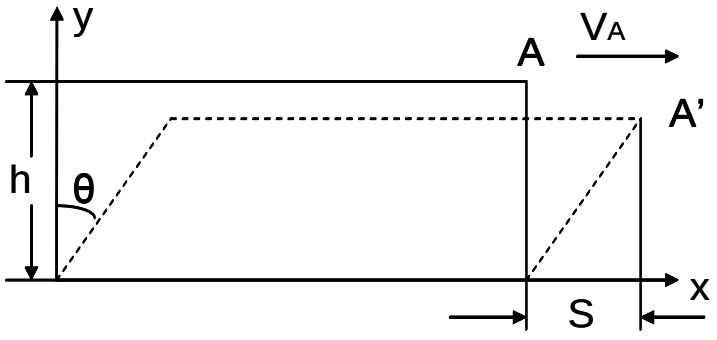

Figure 4.23: Shear deformation and the velocity of the moving surface

5.0 CONCLUSIONS AND FUTURE WORK

Major conclusions are drawn in this chapter. A brief summary of the contributions and recommendations for future work are presented.

5.1 CONCLUSIONS

The work in this dissertation focuses on computational studies of the electromechanical responses of ionic polymer transducers (IPTs). The mechanical properties of ionic polymers, the ionomer morphology, and the fundamental mechanism responsible for the electromechanical sensing responses of IPTs are studied.

A multiscale modeling approach has been developed. The approach is able to predict ionic polymer local stiffness, which is inaccessible via experimentation. The approach applies a Monte Carlo methodology in the creation of polymer chain using rotational isomeric state (RIS) theory. The lengths of the crosslinks in the polymer chains are then fitted with Johnson distributions to simulate their probability density function, which is related to the entropy change of the material under stress. In this dissertation the RIS theory is adapted so that early chain termination is eliminated and longer molecule chains are achieved. This enables more stable and realistic predictions by an order of magnitude over the previous approach, and greatly lowers the computation burden as compared to some common computational dynamics studies. The cluster

morphology proposed by Hsu and Gierke [23] is imposed in the approach. Ionic polymers with differenct hydration levels and cations are modeled. The predicted trends that ionic polymer with lower hydration level is stiffer and sodium form Nafion is stiffer than lithium form Nafion are correct. Having estatblished that the modeling approach is robust, as an illustration it is then employed to forecast properties of lesser known system Selemion. Other multiscale properties that could be studied with this method include evolution of local stiffness and pendant chain stiffness.

The sensing responses of IPT benders are studied by a physics-based modeling approach. The study begins with the streaming current hypothesis, which is assumed to be the fundamental mechanism underlying IPT sensing. The streaming potential hypothesis argues that whenever there is a net relative motion of the electrolyte with respect to the electrode a streaming potential is devoloped, which makes this method viable for all deformation modes. To preliminarily illustrate the streaming potential hypothesis, the parallel water channel morphology in Nafion membrane proposed by Schimdt-Rohr and Chen [29] is imposed. The proof of concept modeling of IPT bending shows good agreement with experimental observations in both the trends and the magnitude of the strain induced current. The model is then normalized to capture the prediction trends more easily. The effect of electrode architecture is studied by comparing the predictions of the sensing responses in IPTs with various electrode particulate volume fractions or metal contents. The predicted trend that the sensitivity first increases and then decreases when the electrode particulate volume fraction increases is consistent with the reported experiments. The predition shows that electrodes containing more large surface area particulates are more sensitive, which is also consistant with experimental data. The effect of IPT diluents are studied by comparing water swollen IPTs with ionic liquid swollen IPTs. The predictions successfully

capture the trends that water swollen IPTs are more sensitive and that lithium form IPTs are more sensitive than sodium form IPTs. The model evolves from parallel rectangular channel model to parallel circular cylindrical channel model, which is more akin to the morphology model in Nafion proposed by Schimdt-Rohr and Chen [29]. Although the adaption of channel geometry does not affect the prediction trends, it is important for model adaption to the cluster morphology proposed by Hsu and Gierke [23]. With this morphology adaption, streaming currents are considered to be developed in the clusters and the conduction channels. The effect of IPT diluent is studied again. Comparing with the parallel channel model, the model with cluster morphology is able to achieve predictions much closer to the reported experiments.

It is widely accepted that strong correlations exists among the ionic polymer morphology and stiffness, electrode architecture, and active response. Although there is a lack of consensus on both ionomer morphology and underlying electromechanical mechanisms responsible for IPT sensing, it is understood that both are functions of ionomer stiffness. In the case of IPT transduction models this stiffness dependence is displayed at two length scales. At the device length scale, classic characterization parameters such as free displacement and blocked force are a function of the active material's stiffness. At the nanoscopic length scale, the local backbone elastic energy is an important parameter in morphology evolution. Multiscale modeling represents one viable approach to exploring this multi-length scale dependence. On the other side, manipulation of diluent, counterion, and even base ionomer in IPTs are also known to affect ionomer morphology. From the multiscale modeling of ionic polymer stiffness and the modeling of streaming current in IPT sensing ,the interdependence between the ionomer material state and the IPT active response have been studied providing valuable insights into the actual mechanism in IPT sensing and enabling in-depth study of IPT electromechanical responses. Correlations

appear repeatedly in the presented studies, for instance evolution of morphology was required in predicting that an optimum particulate volume fraction exists. While not employed in the current study, other important opportunities for overlap between the two studies include assessing local streaming current as a function of local stiffness, as well as reconsidering charge density (which is known to be a function of pendant chain stiffness).

It is argued that this dissertation provides validation of the streaming potential hypothesis in IPT sensing. The modeling of IPT sensing responses afterwards follows the streaming potential method, which should be able to predict IPT sensing not only in bending, but in shear, tension, and compression as well. From a preliminary demonstration of IPT sensing in shear mode, it is argued that the streaming potential method has the potential of being used as a robust modeling approach to predict the sensing response of IPT in all deformation modes.

5.2 CONTRIBUTIONS

The main contributions of this dissertation include:

1. A new understanding of the relationship between polymer synthesis and polymer morphology for a wide class of materials based on ion-conducting and electron-conducting polymers;

2. A new understanding of the fundamental physics underlying the electromechanical sensing responses in ionic polymer transducers;

3. Creation of a computationally efficient tool for optimizing electrode architecture in ionic polymer transducers;

4. New insights into the relationship between polymer morphology and the sensing responses.

5.3 FUTURE WORK

Based on the work presented in this dissertation, the recommendation for future work are:

1. Integrate local stiffness predictions and streaming current predictions, *i.e.*, assess IPT current as a function of local stiffness.
2. Use the modeling method to design the electrode architecture for optimization of IPT sensor array.
3. Design and perform experiments as the experimental conditions are highly consistent with the predicting models.
4. Modeling the IPT sensing response in all other three deformation modes to further prove the streaming potential mechanism in IPT sensing.
5. Study other phenomenon of IPT transduction (for instance, the back relaxation phenomena) that are not discussed in this dissertation.

APPENDIX A

STIFFNESS PREDICTION FOR LITHIUM EXCHANGED NAFION 1200 EW

A.1 M = 50~80, JOHNSON UNBOUNDED DISTRIBUTION, OLS FITTING

Data set #	K-S	γ	δ	λ	ξ	r_o	Mean	SD	Stiffness
1	0.0221	-10.08	3.775	2.02	3.557	19.0376	18.5927	4.091665	13.6393
2	0.018	-4.906	3.297	5.509	6.573	19.1487	18.6937	4.149493	13.6748
3	0.0182	-3.855	3.215	6.884	7.752	19.0993	18.6459	4.136868	14.0921
4	0.018	-4.261	3.043	5.418	7.692	19.0389	18.5852	4.131592	13.6292
5	0.0193	-6.104	3.256	3.874	5.72	19.124	18.6453	4.252078	12.6808
6	0.0166	-8.154	3.151	1.812	6.036	19.092	18.6363	4.146418	12.9683
7	0.0158	-1.156	1.945	6.232	14.11	19.1106	18.5907	4.427291	15.6163
8	0.0193	-6.327	3.746	5.179	4.49	18.9654	18.5227	4.073817	13.9246
9	0.0134	-1.235	1.942	6.128	13.94	19.223	18.6956	4.471942	15.0969
10	0.0169	-5.224	3.355	5.153	6.25	18.9029	18.463	4.054289	13.9059
Mean	0.01776	-5.1302	3.0725	4.8209	7.612	19.07424	18.60711	4.193545	13.92282
SD	0.002329	2.77753	0.640105	1.72626	3.612963	0.092021	0.073025	0.145635	0.879212

A.2 M = 50~80, JOHNSON UNBOUNDED DISTRIBUTION, DWLS FITTING

Data set #	K-S	γ	δ	λ	ξ	r_o	Mean	SD	Stiffness
1	0.0234	-3.066	2.724	6.275	9.402	19.1445	18.6565	4.294984	13.1846
2	0.0164	-1.352	1.86	5.543	13.72	19.3383	18.7965	4.545485	14.0693
3	0.014	-1.23	1.835	5.632	14.03	19.2853	18.7449	4.533378	14.6451
4	0.0156	-1.173	1.685	5.006	14.2	19.2626	18.6999	4.62185	13.9709
5	0.0168	-1.487	1.874	5.462	13.21	19.3145	18.7483	4.642322	12.8929
6	0.0167	-2.767	2.595	6.129	10.18	19.1058	18.6307	4.234219	13.6429
7	0.018	-1.254	1.844	5.641	13.86	19.1985	18.6543	4.538667	14.3703
8	0.0189	-3.035	2.774	6.526	9.351	19.1985	18.6543	4.538667	13.2742
9	0.0165	-1.267	1.808	5.493	13.9	19.3183	18.7618	4.603431	13.988
10	0.0171	-2.793	2.628	6.213	10	18.9867	18.5128	4.215568	13.6129
Mean	0.01734	-1.9424	2.1627	5.792	12.1853	19.2153	18.686	4.476857	13.76511
SD	0.002497	0.84625	0.450934	0.470148	2.139285	0.111824	0.082621	0.163364	0.547929

A.3 M = 50~80, JOHNSON BOUNDED DISTRIBUTION, OLS FITTING

Data set #	K-S	γ	δ	λ	ξ	r_o	Mean	SD	Stiffness
1	0.028	3.312	2.629	59.6	4.936	18.9187	18.5069	3.925794	13.5504
2	0.0193	6.017	2.95	113.3	5.105	19.0889	18.6527	4.057448	13.2842
3	0.023	3.311	2.479	58.93	5.879	19.0108	18.5935	3.961348	13.1974
4	0.0248	4.641	2.789	80.41	5.233	18.9161	18.4982	3.954167	13.5496
5	0.0272	4.385	3.285	79.18	1.628	18.8997	18.4708	4.003524	13.7026
6	0.0266	3.1	2.644	56.4	4.752	18.8526	18.454	3.856217	13.9654
7	0.0281	2.965	2.72	56.67	3.822	18.8352	18.4241	3.913732	13.6547
8	0.0292	2.58	2.473	50.17	4.986	18.8211	18.4156	3.885805	13.4528
9	0.0213	5.155	2.892	92.53	4.8	19.0388	18.6021	4.054353	13.1834
10	0.028	2.796	2.584	52.48	4.697	18.7262	18.331	3.826879	13.9033
Mean	0.02555	3.8262	2.7445	69.967	4.5838	18.91081	18.49489	3.943927	13.54438
SD	0.003331	1.152517	0.24768	20.73283	1.157651	0.110324	0.098142	0.078211	0.272872

A.4 M = 50~80, JOHNSON BOUNDED DISTRIBUTION, DWLS FITTING

Data set #	K-S	γ	δ	λ	ξ	r_o	Mean	SD	Stiffness
1	0.0271	4.691	2.777	84.4	4.936	19.0257	18.5781	4.102616	12.7406
2	0.0212	6.683	2.943	138	5.236	19.154	18.6971	4.158626	12.7304
3	0.022	3.967	2.521	70.85	5.979	19.0943	18.6504	4.093272	12.5356
4	0.0214	5.019	2.79	90.24	5.234	18.9838	18.5443	4.061231	12.947
5	0.0285	4.069	3.217	75.22	1.628	18.9614	18.5275	4.033167	13.542
6	0.0228	3.598	2.705	63.83	4.752	18.9216	18.5072	3.938337	13.5722
7	0.0253	3.219	2.741	60.5	3.823	18.899	18.4738	3.986341	13.2821
8	0.0218	5.572	2.82	104.8	5.257	18.9982	18.5451	4.124424	12.6107
9	0.0201	4.993	2.835	90.93	4.801	19.0789	18.6272	4.126966	12.7287
10	0.0207	6.984	3.24	135.2	3.933	18.8741	18.4417	4.016883	13.5195
Mean	0.02309	4.8795	2.8589	91.397	4.5579	18.9991	18.55924	4.064186	13.02088
SD	0.002872	1.252466	0.222573	27.32345	1.210134	0.090333	0.079961	0.069855	0.414981

A.5 M = 80~100, JOHNSON UNBOUNDED DISTRIBUTION, OLS FITTING

Data set #	K-S	γ	δ	λ	ξ	r_o	Mean	SD	Stiffness
1	0.0194	-5.277	3.229	4.736	6.432	19.143	18.681	4.180274	13.2923
2	0.0198	-6.719	3.518	3.954	5.015	19.0592	18.6099	4.113967	13.5717
3	0.0182	-4.777	3.114	4.98	6.969	19.0242	18.5603	4.175578	13.1956
4	0.0174	-3.8	3.115	6.485	8.001	19.0057	18.5556	4.111732	14.057
5	0.014	-1.1	1.758	5.487	14.32	19.1745	18.6248	4.558319	14.9371
6	0.0182	-5.566	3.34	4.683	6.039	18.987	18.5391	4.099749	13.6219
7	0.019	-8.103	3.41	2.426	5.09	19.0535	18.6033	4.117413	13.3286
8	0.0219	-7.106	3.734	4.181	4.324	18.9686	18.5324	4.044495	14.0078
9	0.0182	-7.738	3.396	2.636	5.251	18.9914	18.5473	4.083006	13.4735
10	0.0187	-6.057	3.407	4.323	5.606	19.0262	18.5769	4.110362	13.5634
Mean	0.01848	-5.6243	3.2021	4.3891	6.7047	19.04333	18.58306	4.159489	13.70489
SD	0.002002	2.077178	0.540167	1.216469	2.881185	0.067515	0.04661	0.145654	0.516771

A.6 M = 80~100, JOHNSON UNBOUNDED DISTRIBUTION, DWLS FITTING

Data set #	K-S	γ	δ	λ	ξ	r_o	Mean	SD	Stiffness
1	0.0171	-1.143	1.655	5.011	14.32	19.3981	18.812	4.732329	13.6018
2	0.0183	-3.698	2.861	5.741	8.383	19.142	18.6583	4.27598	12.9713
3	0.02	-5.823	3.039	3.47	6.432	19.0946	18.6064	4.290178	12.2557
4	0.0194	-3.888	2.906	5.561	8.141	19.0852	18.6101	4.231907	13.0964
5	0.0157	-1.188	1.7	5.099	14.09	19.2512	18.6797	4.655911	13.7055
6	0.0178	-8.986	3.232	1.562	5.436	19.0644	18.5956	4.201786	12.6436
7	0.023	-0.9388	1.39	4.073	14.97	19.4652	18.8105	5.005907	12.4103
8	0.0177	-1.137	1.718	5.217	14.28	19.2287	18.6752	4.580372	14.5359
9	0.0204	-4.415	2.923	4.783	7.671	19.0677	18.5942	4.222903	12.8767
10	0.0151	-1.288	1.791	5.305	13.84	19.2412	18.693	4.560211	13.9749
Mean	0.01845	-3.25048	2.3215	4.5822	10.7563	19.20383	18.6735	4.475748	13.20721
SD	0.002343	2.663209	0.721275	1.262072	3.836825	0.140678	0.081297	0.272892	0.729842

A.7 M = 80~100, JOHNSON BOUNDED DISTRIBUTION, OLS FITTING

Data set #	K-S	γ	δ	λ	ξ	r_o	Mean	SD	Stiffness
1	0.0309	3.017	2.558	55.86	5.015	18.9529	18.5401	3.934096	13.4387
2	0.029	3.213	2.692	58.8	4.433	18.8928	18.484	3.908917	13.7256
3	0.0283	4.528	2.941	78.91	4.081	18.8578	18.4356	3.968031	13.5621
4	0.029	2.606	2.429	49.66	5.408	18.8369	18.436	3.86558	13.5307
5	0.0268	3.856	2.832	68.33	4.11	18.8655	18.4458	3.957215	13.5319
6	0.0275	2.741	2.36	50.4	5.999	18.8269	18.4228	3.879769	13.2796
7	0.0343	2.941	2.901	57.56	2.783	18.8078	18.4081	3.856837	14.2399
8	0.0329	3.078	2.74	57.07	4.07	18.8176	18.4187	3.854032	14.0715
9	0.0283	2.579	2.377	48.58	5.775	18.8214	18.425	3.842457	13.5633
10	0.0225	3.917	2.586	68.12	5.771	18.9373	18.5166	3.969491	13.2042
Mean	0.02895	3.2476	2.6416	59.329	4.7445	18.86169	18.45327	3.903642	13.61475
SD	0.003286	0.645509	0.213436	9.724077	1.024429	0.050914	0.044875	0.050246	0.323683

A.8 M = 80~100, JOHNSON BOUNDED DISTRIBUTION, DWLS FITTING

Data set #	K-S	γ	δ	λ	ξ	r_o	Mean	SD	Stiffness
1	0.0245	7.367	3.038	163.1	4.867	19.1456	18.6791	4.200622	12.5629
2	0.024	4.875	3.059	86.12	3.581	18.9752	18.5439	4.022684	13.4813
3	0.0291	3.163	2.685	59.42	4.081	18.8729	18.4462	3.990496	13.1511
4	0.0232	4.8	2.723	86.38	5.395	18.9954	18.5508	4.085712	12.7308
5	0.0257	3.999	2.822	71.54	4.109	18.9207	18.4862	4.031538	13.1089
6	0.0192	5.471	2.715	102.7	5.912	18.9863	18.54	4.092431	12.6525
7	0.0296	4.383	3.15	76.96	2.781	18.8879	18.4736	3.934319	14.0437
8	0.0265	6.083	3.115	112.6	4.07	18.9689	18.5307	4.05368	13.3112
9	0.0291	2.366	2.494	48.55	4.541	18.8255	18.4222	3.875822	13.5679
10	0.0204	4.621	2.652	82.59	5.737	18.9969	18.5556	4.070862	12.7299
Mean	0.02513	4.7128	2.8453	88.996	4.5074	18.95753	18.52283	4.035817	13.13402
SD	0.0036	1.416846	0.227872	32.06365	0.987343	0.088458	0.072143	0.089782	0.477566

A.9 M = 100~120, JOHNSON UNBOUNDED DISTRIBUTION, OLS FITTING

Data set #	K-S	γ	δ	λ	ξ	r_o	Mean	SD	Stiffness
1	0.0169	-4.242	3.05	5.572	7.501	19.0513	18.5821	4.202094	13.2209
2	0.0145	-0.9796	1.824	5.863	14.72	19.0716	18.5579	4.396621	16.7721
3	0.0151	-1.071	1.751	5.447	14.52	19.2278	18.6909	4.512045	15.5201
4	0.0172	-3.422	3.106	7.117	8.5	18.9818	18.5332	4.102344	14.3392
5	0.0221	-7.831	3.831	3.761	3.807	19.0169	18.5801	4.052452	14.0146
6	0.0203	-10.12	3.581	1.638	4.233	19.0044	18.5555	4.106171	13.3783
7	0.016	-5.297	3.272	4.886	6.176	19.0553	18.5894	4.187919	13.1641
8	0.0208	-15.7	3.712	0.4151	3.8	19.0168	18.5792	4.056108	13.7592
9	0.014	-0.9054	1.719	5.439	15.01	19.0772	18.5619	4.404024	17.2889
10	0.0201	-7.923	3.809	3.642	3.739	19.0363	18.5919	4.089251	13.7755
Mean	0.0177	-5.7491	2.9655	4.37801	8.2006	19.05394	18.58221	4.210903	14.52329
SD	0.002905	4.751265	0.872372	2.04923	4.805091	0.068158	0.042284	0.166567	1.490327

A.10 M = 100~120, JOHNSON UNBOUNDED DISTRIBUTION, DWS FITTING

Data set #	K-S	γ	δ	λ	ξ	r_o	Mean	SD	Stiffness
1	0.0149	-1.314	1.791	5.314	13.71	19.2472	18.6863	4.612689	13.5255
2	0.017	-1.19	1.81	5.493	14.11	19.1552	18.6266	4.468944	15.0445
3	0.0156	-1.127	1.676	5.049	14.38	19.3114	18.7493	4.625356	14.3108
4	0.0164	-2.845	2.724	6.602	9.787	19.0544	18.5789	4.230205	13.6971
5	0.0219	-3.412	2.851	6.213	8.718	19.1371	18.6527	4.278479	13.143
6	0.018	-4.58	2.978	4.796	7.324	19.0686	18.5891	4.249337	12.7249
7	0.0164	-2.429	2.462	6.31	10.72	19.1355	18.6321	4.360299	13.1714
8	0.0225	-15.58	3.361	0.2552	4.86	19.0717	18.6072	4.183521	12.8135
9	0.0189	-2.303	2.511	6.534	11.13	19.0306	18.5659	4.179844	14.4576
10	0.0214	-4.14	3.012	5.644	7.621	19.1338	18.6544	4.25625	13.0113
Mean	0.0183	-3.892	2.5176	5.22102	10.236	19.13455	18.63425	4.344492	13.58996
SD	0.002757	4.278216	0.583243	1.853886	3.197361	0.088147	0.055036	0.16794	0.779228

A.11 M = 100~120, JOHNSON BOUNDED DISTRIBUTION, OLS FITTING

Data set #	K-S	γ	δ	λ	ξ	r_o	Mean	SD	Stiffness
1	0.0219	3.763	2.498	66.13	6.019	18.9357	18.5056	4.012917	12.7855
2	0.0231	4.777	2.804	82.66	5.29	18.9464	18.5142	4.023738	13.6233
3	0.032	3.457	2.991	63.39	2.962	18.8647	18.465	3.86273	14.374
4	0.0257	2.677	2.316	49.6	6.161	18.8596	18.452	3.89977	13.0994
5	0.0276	5.121	3.117	88.74	3.72	18.9289	18.5142	3.940514	14.0182
6	0.0252	6.382	3.217	117.6	3.791	18.8933	18.4647	4.001455	13.6339
7	0.02	3.001	2.264	54.21	6.661	18.9816	18.5397	4.071936	12.3653
8	0.0264	3.71	2.56	64.23	5.851	18.9815	18.5393	4.073291	13.4259
9	0.0261	3.053	2.534	54.18	5.552	18.822	18.4333	3.805409	14.1033
10	0.0216	4.924	2.838	86.96	5.047	18.9884	18.5599	4.011165	13.3338
Mean	0.02496	4.0865	2.7139	72.77	5.1054	18.92021	18.49879	3.970293	13.47626
SD	0.003484	1.17348	0.329865	21.07092	1.22033	0.058024	0.042626	0.089982	0.616038

A.12 M = 100~120, JOHNSON BOUNDED DISTRIBUTION, DWLS FITTING

Data set #	K-S	γ	δ	λ	ξ	r_o	Mean	SD	Stiffness
1	0.0185	6.477	2.792	136.9	5.753	19.0614	18.5919	4.204548	12.1772
2	0.0238	4.23	2.679	74.43	5.319	18.9464	18.5142	4.023738	12.9996
3	0.0272	4.6	3.148	80.71	2.961	18.9563	18.5367	3.966366	13.9189
4	0.0189	6.638	3.003	132.7	4.911	18.9959	18.5481	4.100269	12.9408
5	0.0308	2.461	2.48	49.7	4.708	18.9072	18.4962	3.920816	13.3533
6	0.023	6.494	3.187	122.9	3.862	18.9452	18.5051	4.059788	13.2978
7	0.0197	2.881	2.218	53.12	6.66	18.9816	18.5397	4.071936	11.9765
8	0.024	7.329	3.107	154.7	4.698	19.029	18.5819	4.100711	13.0757
9	0.0227	7.119	3.098	144.4	4.833	18.822	18.4332	3.805893	13.4766
10	0.0234	5.879	2.832	113.8	5.393	19.0753	18.6194	4.145481	12.5941
Mean	0.0232	5.4108	2.8544	106.336	4.9098	18.97203	18.53664	4.039955	12.98105
SD	0.00377	1.75707	0.320138	38.67457	1.008976	0.0752	0.053671	0.116251	0.594417

BIBLIOGRAPHY

1. Sadeghipour, K., Salomon, R., and Neogi, S., 1992, “Development of a novel electrochemically active membrane and 'smart' material based vibration sensor/damper,” *Smart Mater. Struct*. **1**(2), 172.

2. Shahinpoor, M., Bar-Cohen, Y., Simpson, J.O., and Smith, J., 1998, “Ionic polymer-metal composites (IPMCs) as biomimetic sensors, actuators and artificial muscles - a review,” *Smart Mater. Struct.* **7**(6), R15.

3. Farinholt, K., Newbury, K., Bennet, M.D., and Leo, D.J., 2002, “An investigation into the relationship between charge and strain in ionic polymer sensors,” *First World Congress on Biominetics and Artificial Muscles*, Albuquerque, NM, 9-11 December.

4. Associated Press: Update 1: Audi, VW, and Porsche to make hybrid engine. *Forbes*, September 12, 2005.

5. Landler, M. and Bradsher, K., “VW to build hybrid minivan with Chinese,” *New York Times*, September **9,** 2005.

6. Schneider, G., “Priming the public for hydrogen fuel,” *The Washington Post*, November **10**, 2004.

7. Hickner, M.A., Ghassemi, H., Kim, Y.S., Einsla, B.R., and McGrath J.E., 2001, “Alternative polymer systems for proton exchange membranes (PEMs),” *Chem. Rev.* **104**(10), pp. 4587-4612.

8. Oguro, K., Kawami, Y., and Takenaka, H., 1992, “An actuator element of polyelectrolyte gel membrane-electrode composite,” *Osaka Kogyo Gijutsu Shikensho Kiho*. **43**(1), pp. 21-24.

9. Osada, Y. and Hasebe, M., 1985, “Electrically activated mechanochemical devices using polyelectrolyte gels,” *Chem. Lett.* **14(**9), pp. 1285-1288.

10. Newbury, K., and Leo, D.J, 2002, “Electromechanical Modeling and Characterization of Ionic Polymer Benders,” *Journal of Intelligent Material Systems and Structures* **13**(1), pp. 51-60.

11. Farinholt, K., and Leo, D.J., 2004, “Modeling of electromechanical charge sensing in ionic polymer transducers,” *Mechanics of Materials* **36**(5), pp. 421-433.

12. Bennett, M.D., and Leo, D.J., 2004, “Ionic liquids as stable solvents for ionic polymer transducers,” *Sensors and Actuators A* **115**, pp. 79-90.

13. Akle, B.J., Bennett, M.D., and Leo, D.J., 2006, “High-strain ionomeric-ionic liquid electroactive actuators,” *Sensors and Actuators A Physics* **126**(1), pp. 173-181.

14. Bar-Cohen, Y., 2001, “Electroactive polymer (EAP) actuators as artificial muscles—reality, potential, and challenges (SPIE, The International Society for Optical Engineering, Bellingham, WA).

15. Shahinpoor, M., 1992, “Conceptual design, kinematics and dynamics of swimming robotic structures using ionic polymeric gel muscles,” *Smart Mater. Struct.* 1(1), 91-94.

16. Shahinpoor, M., and Kim, K.J., 2000, “The effect of surface-electrode resistance on the performance of ionic polymer–metal composite (IPMC) artificial muscles,” *Smart Mater. Struct.* **9**, pp. 543–551.

17. Yeager, H.L., and Kipling, B., 1979, “Ionic diffusion and ion clustering in a perfluorosulfonate ion-exchange membrane,” *J. Phys. Chem.* **83**(14), pp. 1836-1839.

18. Starkweather, H.W., Jr., 1982, “Crystallinity in Perfluorosulfonic Acid Ionomers and Related Polymers,” *Macromolecules* **15** (2), 320-323.

19. Litt, M. H., 1997, **“**A reevaluation of Nafion morphology,” Polymer Preprint 38, 80**–**81.

20. Rebrov, A.V., Ozerin, A.N., Svergun, D.I., Bobrova, L.P., and Bakeyev, N.F., 1990, “Small Angle X-ray Scatter Study of the Aggregation of Macromolecules of the Perfluorosulphonated Ionomer in Solution.” *Polymer Science U.S.S.R.*, **32**(8), pp. 1515-1521.

21. Termonia, Y., 2007, “Nanoscale modeling of the structure of perfluorosulfonated ionomer membranes at varying degrees of swelling,” *Polymer* **48**, pp. 1435-1440.

22. Paddison, S.J., 2003, “Proton Conduction Mechanisms at Low Degrees of Hydration in Sulfonic Acid-Based Polymer Electrolyte Membranes,” *Annu. Rev. Mater. Res.* 33 pp. 289-319.

23. Hsu, W.Y., and Gierke, T.D., 1982, “Elastic theory for ionic clustering in perfluorinated ionomers,” *Macromolecules* **15**, pp. 101-105.

24. Datye, V.K., Taylor, P.L., and Hopfinger, A.J., 1984, “Simple model for clustering and ionic transport in ionomer membranes,” *Macromolecules* 17, pp. 1704-1708.

25. Datye, V.K., and Taylor, P.L., 1985, “Electrostatic contributions to the free energy of clustering of and ionomer,” *Macromolecules* 18, pp. 1479-1482.

26. Li, J.Y., and Nemat-Nasser, S., 2000, “Micromechanical analysis of ionic clustering in Nafion perfluorinated membrane,” *Mechanics of Materials* **32**, 303-314.

27. Bennett, M.D., 2005, “Electromechanical Transduction in Ionic Liquid-Swollen Nafion Membranes,” PhD dissertation.

28. Nemat-Nasser, S., 2002, “Micromechanics of actuation of ionic polymer-metal composites,” *J. Appl. Phys.* **92**(5), pp. 2899-2915.

29. Schmidt-Rohr, K., and Chen, Q., 2008, "Parallel Cylindrical Water Nanochannels in Nafion Fuel-Cell Membranes," *Nature Materials* **7**, pp. 75-83.

30. Nemat-Nasser, S., and Li, J.Y., 2000, “Electromechanical response of ionic polymer-metal composites,” *J. Appl. Phys.* **87**(7), pp. 3321-3331.

31. Weiland, L.M., and Leo, D.J., 2005a, “Computational Analysis of Ionic Polymer Cluster Energetics”, *J. Appl. Phys.* **97**, 013541; also selected for publication in the Virtual Journal of Nanoscale Science and Technology, December 27, 2004.

32. Weiland, L.M., and Leo, D.J., 2005b, “Ionic Polymer Cluster Energetics: Computational Analysis of Pendant Chain Stiffness and Charge Imbalance,” *J. Appl. Phys.* **97**, 123530.

33. Grot, W.G.F., Munn, C.E., and Walmsley, P.N., 1972, *141st Meeting of the Electrochemical Society*, Houston, TX.

34. Kanno, R., Tadokoro, S., Takamori, T., and Hattori, M., 1996, “Linear approximate dynamic model of ICPF actuator,” *Proc. IEEE Int. Conf. on Robotics and Automation* (Piscataway, NJ:IEEE) pp 219–25.

35. Parrott, O., Nicolaisen, A., and Leo, D.J., 2002, “Extensional Transduction Properties of Ionic Polymer Materials,” *Proc. SPIE* 4695, pp. 228.

36. Flory, P.J., 1988, “Statistical mechanics of chain molecules,” Hanser Publisher, New York, NY.

37. Mark, J.E., and Curro, J.G., 1983, “A non-Gaussian theory of rubberlike elasticity based on rotational isomeric state simulations of network chain configurations. I. Polyethylene and polydimehylsiloxane short-chain unimodal networks,” *J. Chem. Phys.* **79**(11), pp. 5705-5709.

38. Yuan, Q.W., Kloczkowski, A., Mark, J.E., and Sharaf, M.A., 1996, “Simulations on the reinforcement of poly(dimethylsiloxane) elastomers by randomly distributed filler particles,” *J. Polym. Sci., Part B: Polym. Phys.* **34**, 1647.

39. Sharaf, M.A., and Mark, J.E., 2004, “Monte Carlo simulations on the effects of nanoparticles on chain deformations and reinforcement in amorphous polyethylene networks,” *Polymer* **45**, 3943.

40. Jones, R.M., 1975, “Mechanics of Composite Materials,” McGraw-Hill Book Company, New York, New York.

41. Weiland, L.M., Lada, E.K., Smith, R.C., and Leo, D.J., 2005, “Application of rotational isomeric state theory to ionic polymer stiffness predictions,” *J. Mater. Res.* **20**(9), pp. 2443-2455.

42. Matthews, J.L., Lada, E.K., Weiland, L.M., Smith, R.C., and Leo, D.J., 2006, “Monte Carlo simulation of a solvated ionic polymer with cluster morphology,” *Smart Mater. Struct.* **15**(1), pp. 187-199.

43. Nemat-Nasser, S., and Wu, Y., 2003, “Comparative experimental study of ionic polymer–metal composites with different backbone ionomers and in various cation forms,” J. Appl. Phys. 93(9), pp. 5255-5267.

44. Bonomo, C., Fortuna, L., Giannone, P., Graziani, S., and Strazzeri, S., 2006, “A model for ionic polymer metal composites as sensors,” *Smart Mater. Struct.* 15, 749–758.

45. Chen, Z., Tan, X., Will, A., and Ziel, C., 2007, “A dynamic model for ionic polymer-metal composite sensors,” *Smart Mater. Struct.* **16**, 1477-1488.

46. Shahinpoor, M., and Kim, K.J., 2001, “Ionic polymer–metal composites: I. Fundamentals,” *Smart Mater. Struct.* **10**, pp. 819–833.

47. Kim, S.J., Kim, S.M., Kim, K.J., and Kim, Y.H., 2007, “An electrode model for ionic polymer-metal composites,” *Smart Mater. Struct.* **16**, pp. 2286-2295.

48. Akle, B.J., 2005, “Characterization and modeling of the Ionomer-conductor interface in ionic polymer transducers,” Ph.D. Dissertation.

49. Akle, B.J., Bennett, M.D., Leo, D.J., Wiles, K.B., and McGrath, J.E., 2007, “Direct assembly process: a novel fabrication technique for large strain ionic polymer transducers,” *J. Mater. Sci.* **42**(16), pp. 7031-7041.

50. Weiland, L.M., and Akle, B.J., “Ionic polymer transducers in sensing: the streaming potential hypothesis,” *Smart Structures and Systems*, in press.

51. Akle, B.J., and Nakad, Z., 2009, “Improved signal conditioning circuit design for ionic polymer transducers as sensors,” *Proc. SPIE 16th Annual Symposium on Smart Structures and Materials*, San Diego, California, Vol. 7292-54.

52. Akle, B.J., Hickner, M, Leo, D.J., and McGrath, J.E., 2005, “Correlation of capacitance and actuation in ionomeric polymer transducers,” *J. Mater. Sci.* **40**(14), pp. 3715-3724.

53. Akle, B., Nawshin, S., and Leo, D., 2007, “Reliability of high strain ionomeric polymer transducers fabricated using the direct assembly process,” *Smart Mater. Struct.* **16**(2), pp. S256-S261.

54. Newbury, K.M., and Leo, D.J., 2003, “Linear electromechanical model of ionic polymer transducers part I: Model development,” *Journal of Intelligent Material Systems and Structures*, 14, pp. 333-342.

55. de Gennes, P.G., Okumura, K., Shahinpoor, M., and Kim, K.J., 2000, “Mechanoelectric Effects in Ionic Gels,” *Europhysics Letters* 50(4), 513.

56. Asaka, K., and Oguro, K., 2000, “Bending of polyelectrolyte membrane platinum composites by electric stimuli,” *J. Elec. Chem.* 480, 186.

57. Tadokoro, S., Takamori, T., and Oguru, K., 2001, “Modeling of IPMC for design of actuation mechanisms,” in *Electroactive Polymer Actuators as Artificial Muscles*, ed. Y. Bar- Cohen, SPIE Publishing, Bellingham, WA, USA.

58. Porfiri, M., 2009, “An electromechanical model for sensing and actuation of ionic polymer metal composites,” *Smart Mater. Struct.* **18**, 015016.

59. He, X., 2008, “Monte Carlo simulation of ion transport of high strain ionomeric polymer transducers,” Ph.D., Dissertation.

60. Helmholtz. II., H., 1853, “Some laws concerning the distribution of electrical currents in conductors with applications to experiments on animal electricity,” *Annalen der Physik und Chemie*, 89(6):211–233.

61. Gouy, G., 1910, “Constitution of the Electric Charge at the Surface of an Electrolyte,” *J. Phys.Radium*, 9:457–468.

62. Chapman, D., 1913, “A contribution to the theory of electrocapillarity,” *Philos Mag.*, 25:475–481.

63. Stern, O., 1924, “On the theory of the electrical double layer,” *Z. Elektrochem*, 30:508, Bibliography entry.

64. Grahame, D.C., 1947, “The electrical double layer and the theory of electrocapillarity,” *Chem. Rev.* **41**(3), pp. 441–501.

65. Bockris, J.O.M., Devanathan, M., and Müller, K., 1963, “On structure of charged interfaces,” *Proc. R. Soc. London* A **274**, pp. 55-79.

66. Werner,C., Köber, H., Zimmermann,R., Dukhin, S., and Jacobasch, H.J., 1998, "Extended electrokinetic characterization of flat solid surfaces," *Journal of Colloid and Interface Science* **208**, pp. 329–346.

67. Ghoniem, N.M., and Cho, K., 2000, “The emerging role of multiscale modeling in nano- and micro-mechanics of materials,” *J. Comput. Aided Mater.*, Des. 3, 164.

68. McFadden, N., AFRL document OSR-02-02.

69. Fermeglia, M., Pricl, S., and Longo, G., 2003, "Molecular modeling and process simulation: Real possibilities and challenges," *Chem. Biochem. Eng.* **17**(1), 69.

70. Kremer, K., and Müller-Plathe, F., 2001, "Multiscale problems in polymer science: Simulation approaches," *MRS Bull.* 205.

71. de la Rubia, T.D., and Bulatov, V., 2001, "Materials research by means of multiscale computer simulation," *MRS Bull.* 169.

72. Phillips, R., 2004, "Modeling the stuff of the material world: Do we need all of the atoms?" *The Bridge (National Academy of Engineering),* Winter, 22.

73. Theodorou, D.N., and Suter, U.W., 1985, "Detailed Molecular Structure of a Vinyl Polymer Glass," *Macromolecules* **18**, pp. 1467-1478.

74. Smith, G.D., Yoon, D.Y., and Jaffe, R.L., 1993, "A Third-Order Rotational Isomeric State Model for Poly(oxyethylene) Based upon ab Initio Electronic Structure Analysis of Model Molecules," *Macromolecules* **26**, pp. 5213-5218.

75. Bahar, I., Zuniga, I., Dodge, R., and Mattice, W.L., 1991, "Configurational Statistics of Poly(dimethylsiloxane) 2: A New Rotational Isomeric State Approach," *Macromolecules* **24**, pp. 2993-2998.

76. Jang, S.S., Molinero, V., Çağin, T., and Goddard III, W.A., 2004, "Nanophase-segregation and transport in Nafion 117 from molecular dynamics simulations: Effect of monomeric sequence," *J. Phys. Chem. B* **108**, 3148.

77. Gao, F., and Weiland, L.M., 2007, "Improving rotational isomeric state theory for application to mechanical properties prediction," *Proc. SPIE on Behavior and Mechanics of Multifunctional and Composite Materials*, San Diego, CA, 6526, pp. 65250Z-1-9.

78. Gao, F., and Weiland, L.M., 2008a, "A multiscale model applied to ionic polymer stiffness prediction," *J. Mater. Res.* **23**(3), pp. 833-841.

79. Gao, F., Weiland, L.M., and Kitchin, J., 2008b, "Rotational isomeric state theory applied to the stiffness predictions of an ionic polymer electrolyte membrane," *Proc. SPIE on Behavior and Mechanics of Multifunctional and Composite Materials*, San Diego, CA, 6929-22.

80. Mauritz, K.A., and Moore, R.B., 2004, “State of understanding of Nafion,” *Chem. Rev.* **104**(10), pp. 4535-4586.

81. Bates, T.W., and Stockmayer, W.H., 1968, “Conformational energies of perfluoroalkanes, part II. Dipole moments of H(CF2)nH,” *Macromolecules* **1**(1), 12.

82. Gruger, A., Régis, A., Schmatko, T., and Colomban, P., 2001, “Nanostructure of Nafion membranes at different states of hydration: An IR and Raman study,” *Vib. Spectrosc.* **26**(2), 215.

83. Treloar, L.R.G., 1975, “The Physics of Rubber Elasticity,” 3rd ed. (Clarendon Press, Oxford, UK,).

84. Swain, J.J., Venkatraman, S., and Wilson, J.R., 1988, “Least-squares estimation of distribution functions in Johnson’s translation system,” *J. Statist. Comput. Simul.* **29**, 271.

85. Krüger, J.K., and Fischer, C., 2000, “The mono-crystalline state of polyvinylidene fluoride/trifluoroethylene on nano-structured Teflon,” *A. le Coutre. Appl. Phys. A* **70**, pp. 297.

86. Kawano, Y., Wang, Y., Palmer, R.A., and Aubuchon, S.R., 2002, “Stress–strain curves of Nafion membranes in acid and salt forms,” *Polimeros.* **12**(2), 96.

87. Han, T-H., Kim, D-O., Lee, Y., Suh, S-J., Jung, H-C., Oh, Y-S., and Nam, J-D., 2006, “Gold nanostructures formed in ionic clusters of perfluorinated ionomer,” *Macromol. Rapid Commun.* **27**(17), pp. 1483.

88. Yoon, D.Y., Sundararajan, P.R. and Flory, P.J., 1975, “Conformational characteristics of polystyrene,” *Macromolecules* **8**, pp. 776-783.

89. van der Heyden, F.H. J. Stein, D. and Dekker, C., 2005, “Streaming currents in a single nanofluidic channel,” *Phys. Rev. Lett.* **95**, pp. 116104.

90. Daiguji, H., Yang, P., Szeri, A.J., and Majumdar, A., 2004, “Electrochemomechanical Energy Conversion in Nanofluidic Channels,” *Nano Lett.*, **4**(12), pp. 2315-2321.

91. Gao, F. and Weiland, L.M., 2008, "Modeling of the electromechanical response of ionic polymer transducers by means of streaming potential mechanism," *Proceeding of ASME*

Conference on Smart Materials, Adaptive Structures and Intelligent Systems: Active Materials, Mechanics and Behaviors, Ellicott City, MD.

92. Zangrilli, U., Gao, F., and Weiland, L.M., "Implications of multiscale modeling on sensing predictions in Nafion," submitted to *Smart Mater. Struct.*, January 2010.

93. Liu, D., Kyriakides, S., Case, S.W., Lesko, J.J., Li, Y., and McGrath, J.E., 2006, "Tensile behavior of Nafion and sulfonated poly(arylene ether sulfone) copolymer membranes and its morphological correlations", *J. Polym. Sci., Part B: Polym. Phys.* **44**, pp. 1453-1465.

94. Franklin, J.W., 2003, "Electromechanical modeling of encapsulated ionic polymer transducers," Master thesis.